Investigating Intergranular Fracture in Nickel via Atomistic Simulations

by

Guoqiang Xu

B.S., Fudan University (2010)

Submitted to the Department of Materials Science and Engineering
in partial fulfillment of the requirements for the degree of

Doctor of Philosophy in Materials Science and Engineering

at the

MASSACHUSETTS INSTITUTE OF TECHNOLOGY

February 2016

Author .....
Department of Materials Science and Engineering
October 30, 2015

Certified by .....
Michael J. Demkowicz
Associate Professor of Materials Science and Engineering
Thesis Supervisor

Accepted by .....
Donald R. Sadoway
Chairman, Department Committee on Graduate Theses

Investigating Intergranular Fracture in Nickel via Atomistic Simulations

by

Guoqiang Xu

Submitted to the Department of Materials Science and Engineering
on October 30, 2015, in partial fulfillment of the
requirements for the degree of
Doctor of Philosophy in Materials Science and Engineering

Abstract

Alloys based on face-centered cubic (FCC) elements such as nickel (Ni) are among the most resistant to fracture. However, when embrittled by impurities, they lose their toughness and crack along grain boundaries. Though long known, this phenomenon remains poorly understood. In this thesis, we use large-scale molecular dynamics (MD) simulations to study the effects of grain boundaries (GBs) on various aspects of fracture properties in Ni, including intergranular fracture mechanisms, fracture toughness as well as crack healing.

By performing statistical analysis on crack tip processes for fracture along different GBs, we revealed three distinct crack propagation mechanisms. For fracture along coherent twin boundary with the crack front along the $[11\bar{2}]$ direction, no bond breaking is observed and crack advance is solely attributed to the slip of atoms at its tip due to the emission of dislocations. The dislocation process leads to the blunting of the crack tip. For fracture along $\Sigma 65(100)$ symmetrical tilt GB, we discovered a new crack propagation mechanism, decohesion restrained by emission of dislocations (DRED). In it, bursts of brittle fracture initiate emission of dislocations, which prevent cracks from propagating more than a few nanometers in a single burst. For fracture along coherent twin boundary with the crack front along the $[1\bar{1}0]$ direction, crack propagates by brittle decohesion, which initiates dislocation emission in a similar way as DRED. However, the dislocation process does not arrest the crack due to the local hardening mechnism, which constraints the motion of dislocations. Using the method developed to calculate the critical energy release rate G_c from atomistic simulations, we also compared the toughness of fractures by these three mechanisms.

In the course of investigating intergranular fracture, we discovered a new mechanism for crack healing in a 2D model. This mechanism relies on the generation of disclination dipoles due to GB migration, which can interact with the crack, causing it to advance or heal. We also demonstrate the healing of nanocracks in realistic 3D microstructures.

Thesis Supervisor: Michael J. Demkowicz

Title: Associate Professor of Materials Science and Engineering

Acknowledgments

First of all, I wish to express my sincere thanks to my research advisor, Prof. Michael J. Demkowicz for his knowledge, his encouragement and his generosity. The things I learned from him are even more than what I learned from my parents. Under his selfless guidance, I grew up from a nervous student who repeat every sentence twice in his first literature review presentation, to a computational scientist who can work independently and confidently. I will never forget, in my hard times, he uses his own story to encourage me and help me move on. His influence on my character will last for my whole life.

I would like to take this opportunity to thank my parents, Jingkuan Xu and Shurong Wang as well as my sister Xianghui Xu for their unconditional love and support all my life.

I am grateful to the member of my thesis committee, Prof. Krystyn Van Vliet and Prof. Christopher A Schuh for many discussions they held with me during different stages of this work. Their incisive comments and insightful guidance have helped me a lot throughout my Ph.D. studies.

I would like to thank my friends for their encouragements and love. My life would lose its color without them. Special thanks to Pengkun Lu, Chongzhao Wu, Han Liu, Wen Ma, Ruize Xu, Yifan Wang and CuiCui Chen. Thank you all for the company.

I would like to thank Prof. David M. Parks for useful discussions on the fracture and crack healing mechanisms. His exceptional knowledge in this field plays an important role in shaping my work. I would like to thank Prof. Silvija Gradecak for the helpful discussions during each sponsor meeting.

I'm also indebted to all members of the Demkowicz group who have helped me during the course of my PhD by listening to my talks and providing me with constructive criticism at every stage. Special thanks to Dr. Richard Baumer for the help during my first year of Ph.D. studies, Wenshan Yu for the useful discussions with my work.

I acknowledge the financial support from MIT-BP corrosion center for this work

under the project of predicting hydrogen-induced intergranular fracture.

Contents

List of Figures

Chapter 1

Introduction

The goal of the research presented here is to investigate the effects of GBs on the mechanisms of intergranular crack propagation, fracture toughness as well as other fracture properties (such as crack healing) in FCC crystalline materials. Both the static (individual GB characteristics) and dynamical (stress-driven GB migration) aspects of GBs will be considered for understanding these effects. This chapter motivates the needs to study the GB's influence on crack propagation behaviors in light of failures of engineering materials due to intergranular fracture as well as designing challenges for fracture-resistant materials. It concludes a brief overview of the remaining chapters.

1.1 Failures due to intergranular brittleness

Intergranular fracture, which takes place in various engineering materials, is a specific fracture mode where the crack propagates along the GB of materials [8]. Intergranular brittleness can cause serious problems in the processing or service of engineering materials and lead to failures of machine components and structures that occur in power generating equipment, oil and gas pipelines, aircraft and aerospace technologies, chemical equipment, and marine structures [9, 10, 11].

Nickel-based alloys exhibit excellent mechanical strength, creep resistance at high temperatures and good corrosion resistance. Therefore they are widely used as struc-

ture materials in extreme environments, such as deleterious elements like hydrogen (H) in elevated temperatures. Under such conditions, brittle intergranular fracture in nickel-based alloys induced by the extreme environment is a major cause for the mechanical failures of structure materials. In the process of environment-assisted cracking (EAC), the mechanical work of external forces (for example, applied tensile stress) and the physicochemical environment are combined in a specific manner to produce macroscopically brittle fracture along GBs at stresses that may be far below those required for general yielding.

Despite decades of researches and studies, the mechanism of intergranular fracture in nickel-based alloys caused by EAC is still not fully understood. Hydrogen embrittlement (HE), for example, has been known to lead to premature failure of nickel-based alloys by brittle intergranular fracture. However, the fracture is not truly brittle. Considerable ductility occurs during fracture as evidenced by deformation markings on the fracture surfaces and shear bands in the adjacent grains. Martin et. al. found that the intergranular fracture surfaces of Ni 201 containing 2000 at. ppm. of hydrogen appear flat and featureless at low spatial resolution in SEM but steps are evident at higher spatial resolution, which indicates there is plasticity associated with brittle-like crack propagations [1]. Further TEM analysis of the microstructure immediately beneath the fracture surface shows dense dislocations inside the cells (see Figure 1-1). Questions regarding fracture behaviors caused by HE remain unclear, such as how the dislocations influence the intergranular crack propagations and what is the role of the surrounding plasticity in contributing to fracture toughness.

At present, intergranular fracture in nickel-based alloys caused by EAC remains to be a major cause of the premature failures of various components and equipment in industry. Understanding the mechanism of intergranular fracture can not only help to prevent or reduce economic losses, but is also directly related to the safety and reliability of potentially dangerous engineering systems. In this thesis, we will investigate the mechanism of crack propagation along GB in pure Ni.

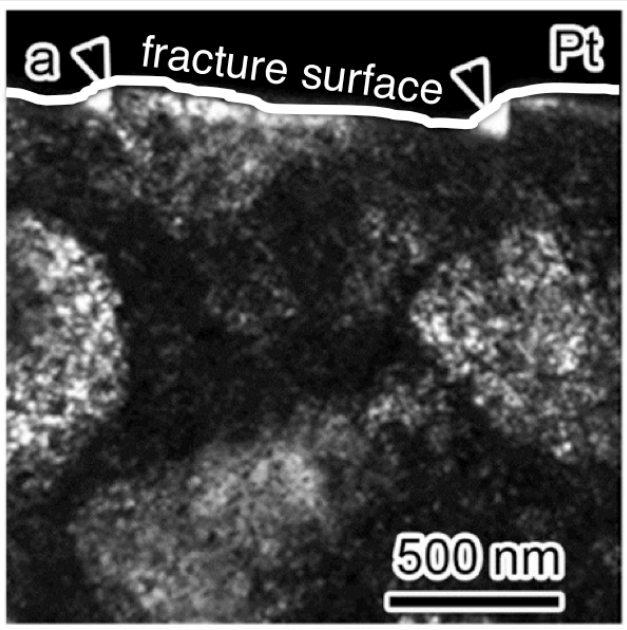

Figure 1-1: Bright-field electron micrographs showing the microstructure following immediately below an intergranular facet in material containing hydrogen [1].

1.2 Interface control for resistance to intergranular fracture

The conditions at which intergranular fracture occurs and the associated fracture toughness are functions of composition, loading configuration, and detailed microstructure, including the number and type of grain boundaries present in the material. The concept of GB design and control is to improve the resistance of conventional polycrystalline alloys to intergranular degradation phenomena by increasing the number of 'strong' GBs in the GB character distribution [12, 13]. This idea is based on the fact that GBs, rather than being simply regarded as two-dimensional planes, have detailed structures, depending on their crystallography and atomic-level state and therefore are expected to exhibit different properties [14].

GB engineering is a technique in materials science and engineering, first proposed by Prof. T. Watanabe in the early 1980s [15]. It employs thermomechanical processing to promote the nucleation of GBs with special type and reduce the incidence

of other types in the microstructure. It has been claimed that this technique can yield improvements in strength, ductility, chemical corrosion, SCC, high-temperature creep and high-cycle fatigue resistance [16, 17, 18, 2]. Bechtle et. al. demonstrates the feasibility of using GB engineering to reduce the susceptibility of intergranular brittleness in hydrogen environment in commercially pure Ni samples [2]. Using this technique, the fraction of special GBs, such as annealing twins and its variants, is increased from 46% to 75%. It is found that the high special fracture microstructure showed almost double the tensile ductility and significantly lowered proportion of intergranular fracture. Figure 1-2 shows the SEM images of fracture surfaces with low and high special GB fractions. The low special fraction microstructure shows 100% intergranular fracture, while the high special fraction microstructure displays a more ductile fracture mode.

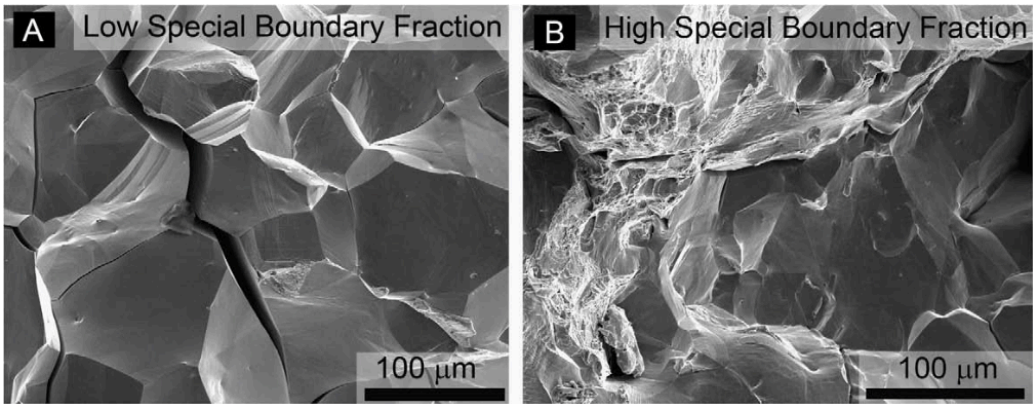

Figure 1-2: Secondary electron micrographs of fracture surfaces. (A) The low special fraction microstructure shows 100% intergranular fracture, while (B) the high special fraction microstructure displays a more ductile fracture mode [2].

The use of GB engineering to enhance the intergranular fracture resistance of materials requires the knowledge of the toughness of individual GBs. However, the relationship between GB structures and fracture properties is still unknown. It is challenging to determine the fracture toughness of individual GBs experimentally, as it requires the preparation of notched flat and defect-free GBs with defined misorientation. Therefore, only a few types of simple GBs (such as pure tilt or twist GBs) are investigated experimentally [19, 20, 21, 3, 22, 23, 24]. Figure 1-3 shows the

misorientation dependence of the intergranular fracture stress observed on purified and non-purified molybdenum bicrystals with <110> tilt boundary having a wide range of misorientation angles up to 180° [3]. It is found that higher values of the fracture stress were observed for the low-angle boundaries with the misorientation angle smaller than about 10° and also for those high-angle boundaries whose misorientation angle is larger than 60° in purified material. The result clearly shows that intergranular fracture stress strongly depends on the misorientation angle, however, the complete dependence of fracture toughness on the five parameters of GBs is still unknown.

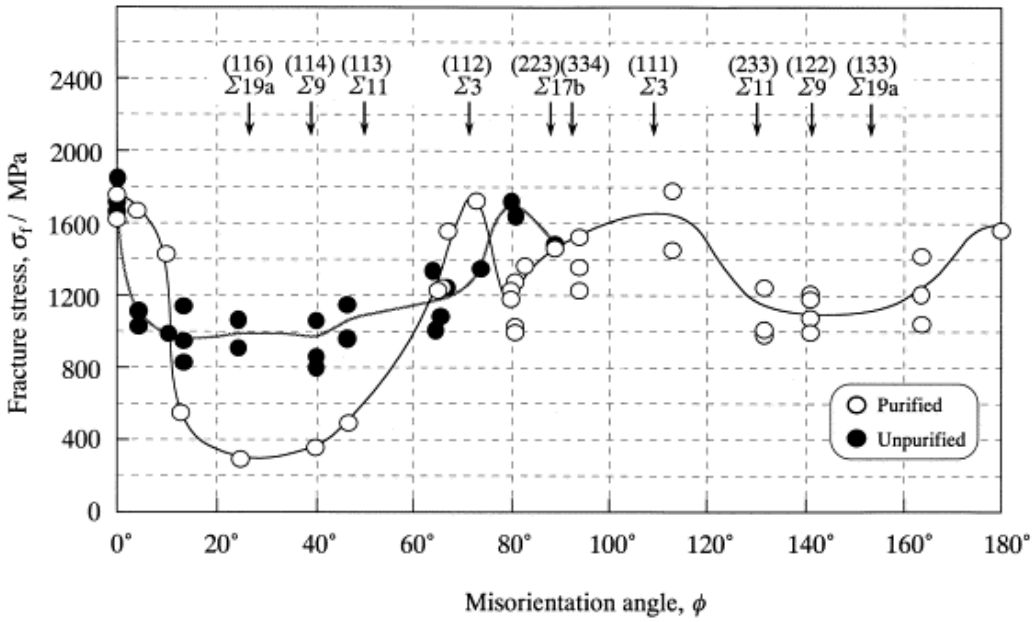

Figure 1-3: Misorientation dependence of fracture stress in molybdenum bicrystals with <110> tilt boundaries [3].

Therefore, understanding of GB's effect on intergranular fracture toughness is of great importance. It may provide insights for designing materials resistant to fracture by promoting a high proportion of 'strong' GBs in polycrystal.

1.3 Organization of the thesis

Chapter 2 provides a review of previous work undertaken to understand the mechanism of intergranular fracture as well as GB's effect on intergranular fracture toughness. Gaps in knowledge about intergranular fracture are identified.

Chapter 3 describes in detail the simulation techniques that are used in this study: molecular dynamics, construction of GBs and the finite element method.

Chapter 4 describes the post-processing techniques that are used in this study to characterize atomistic fracture simulations, including the approaches to estimate crack extension (crack surface area calculation, crack tip position estimation and bond breaking analysis), the method to quantify plastic deformations during fracture (slip vector analysis, dislocation extraction and plastic work density) and the method to estimate critical energy release rate.

Chapter 5 describes in details the atomistic simulations of intergranular fracture in FCC Ni. Fracture simulations along coherent twin boundaries and $\Sigma 65(100)$ symmetrical tilt GB are performed. The fracture mechanisms for crack propagations along these GBs are revealed by statistical analysis of fracture processes at the crack tip. Their critical energy release rates are also calculated and compared.

Chapter 6 describes the crack healing phenomenon discovered in a 2D model in the course of investigating intergranular fracture. The mechanism of healing of nanocracks is analyzed and discussed. The healing of nanocracks in 3D microstructures is also demonstrated.

Chapter 7 is devoted to a discussion of implications of this work as well as open questions.

Chapter 2

Literature review

This chapter presents a literature survey of work done in the field of understanding intergranular crack propagation mechanisms as well as GB's effects on fracture toughness, which serves as background for current research.

2.1 Fracture modes in crystals

A fracture can be described as the separation of an object or material into pieces by an imposed stress [25]. Upon loading, the failure may occur through different fracture modes depending on the manner in which the crack propagates through a material. For FCC materials, there are two possible modes of fracture, ductile and brittle. In general, the main different between brittle and ductile fracture can be attributed to the amount of plastic deformation that the materials undergoes during crack propagations. In ductile materials, crack propagation is accompanied by a large amount of plastic deformation [26], while in brittle materials cracks moves with little or no plastic deformation [27].

Ductile materials usually have high fracture toughness owing to the work of plastic deformation expended during crack advance. Fracture of most ductile materials proceeds by the nucleation, growth and coalescence of voids [28]. Void nucleation usually takes place in regions of high local plastic deformation ahead of the crack tip, resulting in a fracture surface typically covered with hemispherical or hemi-ellipsoidal

dimples [29]. Depending on the loading configuration and material properties, void coalescence may occur after a significant amount of void growth, which leads to a fracture surface covered with large and deep dimples, or start soon after the nucleation of voids, giving rise to shallow and small dimples [30].

Some materials like sapphire can undergo pure brittle fracture with no discernable plasticity associated with this process [31]. Because no plastic work is expensed, the fracture toughness of such materials is therefore low. In brittle fracture, the crack runs fast, leaving a relatively flat surface at the break.

Both ductile and brittle fracture can occur either by transgranular or intergranular fracture. In transgranular fracture, the crack propagates through the grains of the materials. The change of crack propagation direction may occur due to the different crystal orientation of each grain. Intergranular fracture is the crack traveling along the GBs, and not through the grains. Intergranular fracture usually occurs along GBs that are intrinsically brittle, or are weakened by the environment (such as hydrogen) or GB precipitations.

2.2 Classical model for predicting ductile vs. brittle modes of fracture

Knowing the fracture mode not only give the information on the crack propagation mechanism, but also provide a qualitative estimation of the fracture resistance. Therefore, it is of great importance to understand the factors that control whether ductile or brittle occurs in certain crystalline materials under a given set of conditions. Extensive theoretical work on predicting ductile vs. brittle response of materials has been done and is summarized below. Most of the work is concerned with the problem of pure ductile and pure brittle response of crystals and does not consider the intermediate case where cleavage cracking occurs with surrounding plasticity.

One criterion for predicting ductile vs. brittle fracture modes is proposed by Kelly. He compare the ratio of the largest tensile stress to the largest shear stress close to a

crack tip with the ratio of the ideal cleavage stress to the ideal shear stress [32, 33]. If the ideal cleavage stress is first reached, the crack will propagate by decohesion of planes ahead of the crack tip, leading to brittle fracture. On the other hand, if the ideal shear stress is first reached, plastic shear will occur at the crack tip, indicating ductile failure. This criterion may not reflect what happens in reality exactly because it models ductile fracture as a continuum shearing process while in reality ductile fracture occurs with void growth and covalence.

At lower temperatures and/or high loads, void growth is often attributed to dislocation activity. Therefore, Rice and Thomson proposed another criterion [4]: whether a particular microstructural feature undergoes brittle or ductile fracture is determined by a competition between two processes: decohesion of planes and dislocation nucleation at the crack tip (see Figure 2-1). By introducing a dislocation core cut-off parameter, the critical energy release rate G_{dis} for the emission of a half-loop glide dislocation at the crack tip can be calculated. Ductile vs. brittle behavior is therefore predicted by comparing G_{dis} with the critical energy release rate for decohesion G_{dec}: brittle fracture occurs when $G_{dec} < G_{dis}$ while ductile fracture ensues when $G_{dis} < G_{dec}$. However, the core cut-off parameter used in the model is hard to estimate.

Later, Rice proposed a modified criterion based on the Peierls concept to circumvent the need for a core cut-off parameter [34, 35]. In this new criterion, the energy release rate for dislocation nucleation and emission can be calculated by balancing the stress field of the loaded crack and the self-stress of the incipient straight-line dislocation in the glide plane ahead of the crack tip with the interatomic forces across the emission plane. Even though this model is not free of approximations (for example, the formation energy of ledges formed upon dislocation emission is ignored and a single, constrained emission path is used), this criterion is very successful in predicting the fracture mode of some crystals [7, 36]. This model was further modified by other authors to make it more accurate [37, 38, 39, 40].

Schoeck proposed a similar criterion, which is also based on Peierls concept [41], considering the total Gibbs free energy GT of the system and obtained the equilibrium

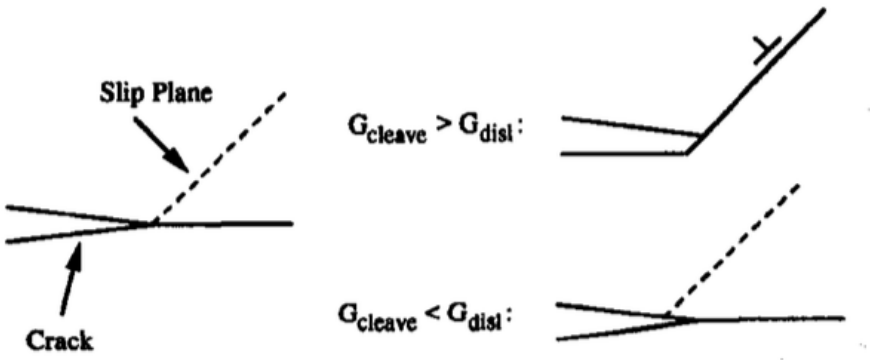

Figure 2-1: Atomistically sharp crack on the left, showing the competition between dislocation emission (upper right) and cleavage decohesion (lower right). [4]

configuration of the incipient dislocation by minimizing GT with respect to a set geometrical shape parameters. The physical basis of this model is the same with that of Rice's, but the treatment is based on vibrational principles and in most cases it need numerical evaluations [42, 43].

Rice's model was a marked improvement over Kelly's, but it nevertheless has limited predictive capability [44]. The most important weakness of this model is that it assumes that cracks in crystals will propagate either by pure brittle fracture without any plasticity or by ductile fracture induced by dislocation nucleation. However, from Figure 1-1, there exist an intermediate case where brittle fracture can occur with surrounding plasticity. The model doesn't consider this. Moreover, Rice's model can only provide analytical results for simple dislocation configurations with straight-line cracks while in real crystals the nucleation phenomena are much more complex. Finally, Rice's model can only be applied to 2D cases, where the emitted dislocation lines are parallel to the crack front.

2.3 GB's effects on ductile vs. brittle behaviors of fracture

The intergranular fracture behaviors of polycrystals are governed by both crack propagation pathways along connected boundaries and the fracture toughness of individual GBs. Thus, the overall toughness of a polycrystal undergoing intergranular fracture depends not only the properties of isolated boundaries, but also on the topological characteristics of the entire GB network [45].

Even the dependence of fracture toughness on individual GBs is a complicated problem. GB is not just a two-dimensional defect in polycrystals but also has its own, often complex, structures at atomic scales [14]. A lot of work has been done to study the GB structures based on symmetry (point groups) [46], local atom arrangement (structure units method) [47, 48] and misfit dislocation models [49, 50]. The effects of GB structure on fracture modes can be understood in terms of Rice's criterion [4], i.e., how the bond breaking as well as dislocation emission processes are influence by the GB structures.

The critical energy release rate for cleavage cracking along GB is related to GB separation energy $2\gamma_s - \gamma_{GB}$, where γ_s is the surface energy and γ_{GB} is the GB energy. Many efforts have been devoted to understand how GB structure influences its GB energies. For example, purely geometrical criteria for low interfacial energy GBs have been developed including small Σ value and high planar CSL site density [51]. These criteria are useful in some cases but are violated in many other cases [52, 5]. For example, in the work of Olmsted et. al., they computed 388 GB energies in Ni using atomistic simulations and found that the dependence of GB energy on geometry parameters are rather complex [5]. Figure 2-2 shows the GB energies vs. inverse density of coincident sites Σ, which violates the criterion proposed above. This limited capability of prediction implies a more sophisticated approach is needed, perhaps incorporating factors other than geometry. All in all, we do not yet understand what exactly determines GB separation energies.

GB structure may also influence dislocation nucleation and emission mechanisms

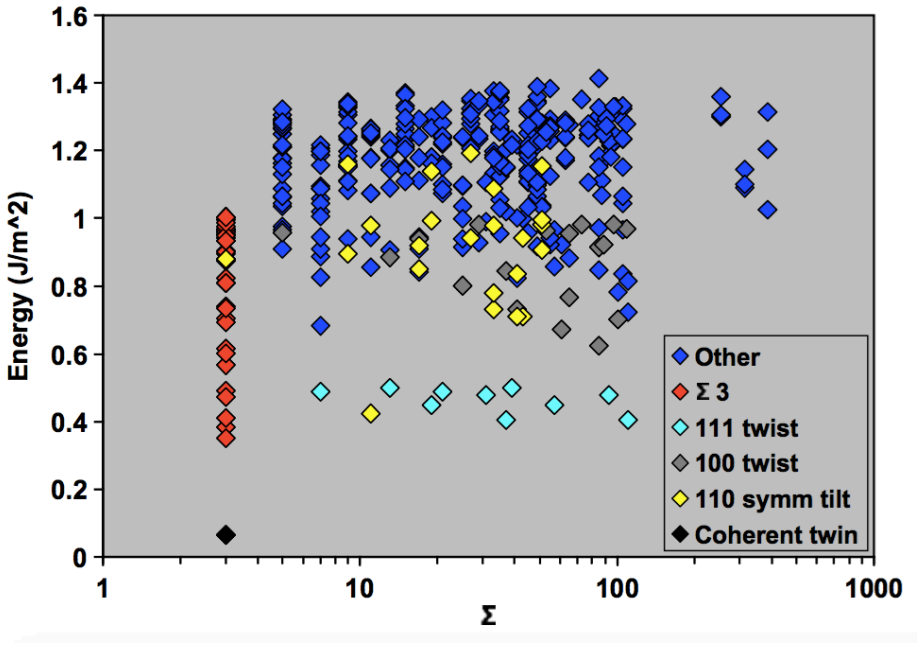

Figure 2-2: The computed GB energies for Ni plotted against Σ, the inverse density of coincident sites [5].

through its local stress field as well as by providing favorable nucleation sites or even ready-made sources or sinks for dislocations [53, 54]. For example, the misfit dislocations on the GB can either shield or antishield the intergranular crack, making the nucleation and emission of dislocations harder or easier [55, 56]. In addition, GB dislocations can also contribute to local variations in loading mode at the crack tip, for example mode II and III loading even when the remote load is of type I. GB stress field may also have an influence on the preferred nucleation sites of dislocations [57]. Moreover, GB dislocations can sometimes act as dislocation sources. The ways that GBs influence dislocation activity are complex and the effects of GBs listed above are not exhaustive.

For more general types of GBs and even for low-angle tilt boundaries in the presence of extrinsic dislocations, the influence of GB structure on process of dislocation nucleation and emission may be markedly different than described above. Furthermore, local stress field is hard to obtain and therefore the exact effects are intractable for theoretical analysis.

2.4 Experimental measurements of the fracture toughness of GBs

Efforts from the experimental side are also devoted to understand the relationship of GB structures and their fracture toughness. The toughness of intergranular fracture is measured by experiments on well-characterized bicrystals for various GBs, e.g. pure twist [19, 23, 24], pure tilt [21, 3], high angle [20], and low-Σ GBs [22]. It is found that not only the fracture modes and toughness can be influenced by the types of GBs. Kaneko prepared and tested copper bicrystals with different GBs, which are slightly deviated from $\Sigma 3$ (111) coherent twin and showed that as the absolute value of the deviation angle from coherent twin increases, the fracture toughness decreases [6]. Moreover, the fracture mode of cracks in this bicrystals is also influenced by GBs. Specimens having deviation angles less than 3 degrees involved no intergranular fracture, while when deviation angles ranged from 3 degrees to 5 degrees, the fraction of surface formed by intergranular fracture increased (see Figure 2-3). In specimens having deviation angles greater than 9 degrees, transgranular cracking became dominant again.

The relationships between GBs and fracture toughness discovered by experimental work is summarized below:

- <100> tilt GBs: fracture toughness decreases from 0° to 20° misorientation angles and appears to be small for high angle GBs [21].
- <110> tilt GBs: GBs with misorientation angles between 0° to 10°, 65° to 73° and 89° have high fracture toughness [3].
- <111> twist GBs: the misorientation dependence of fracture toughness is weak [23].
- High angle GBs: the twist misorientation across a high angle boundary has a more profound effect on fracture toughness than the tilt misorientation. [20]

Besides measurements of toughness of individual GBs, tests on polycrystals are

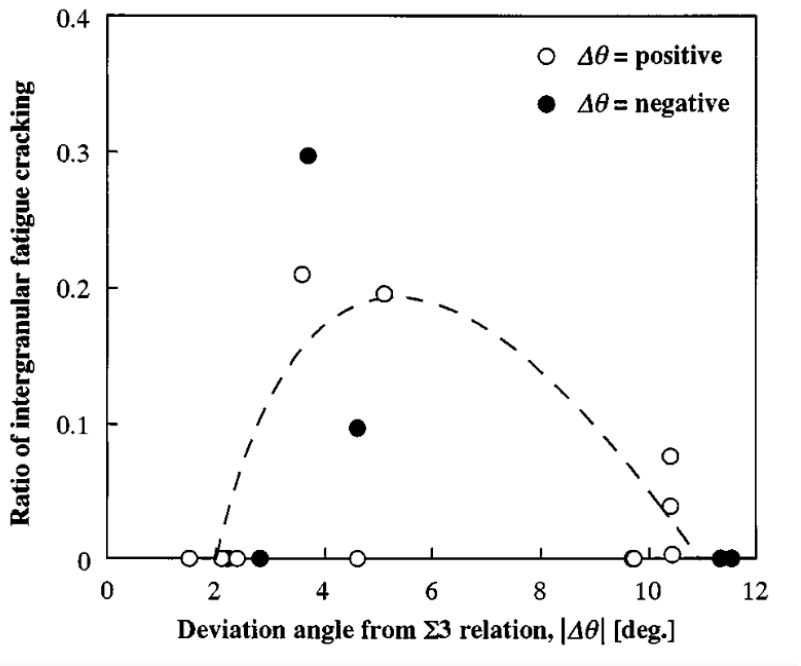

Figure 2-3: The ratio of the intergranular cracking to the primary crack length, plotted against the $|\theta|$ value. The projected lengths to the x-axis were used as the primary crack length in the calculation of the ratio [6].

also performed to infer the dependence of fracture toughness on GBs [58, 59]. It has been shown that the toughness usually increases monotonically with increasing overall fraction of low-Σ boundaries [59]. Moreover, the ratio of intergranular fracture segments to the total crack area was lower for specimens with higher fractions of low-Σ boundaries. However, this does not indicate all low-Σ GBs are stronger than random GBs. Random GBs have distinctive structures, which may be very different from each other and therefore they may exhibit totally different fracture behaviors.

Even though the structures of GBs are well understood, there is still a lack of general knowledge on the relationship of GB structure and their fracture properties. The GBs investigated in the experiments are only a small subset of all GBs and in most experiments the GBs are characterized by its Σ value, which is not able to fully determine GB structures. Moreover, most experiments use polycrystals containing different fractions of 'special' GBs rather than using bicrystals to study GB's effect on fracture toughness, the conclusion drawn from which may be difficult to interpret.

2.5 Atomistic simulations of fracture

2.5.1 Investigation of fracture mechanisms

Atomistic simulation is the ideal tool to investigate crack tip processes during fracture at the atomic scale, which is difficult to access experimentally. Insight into the influence of GB structures on the deformation processes (and hence the fracture mode) has been obtained by simulations of intergranular fracture in bicrystals [7, 60, 61, 62, 63, 36, 64]. Yamakov analyzed intergranular fracture along a $\Sigma 99[110]$ symmetric tilt GB in aluminum [7] and showed that in one direction, the crack propagates in a brittle manner by cleavage with very little or no dislocation emission, and in the other direction, the propagation is ductile through emission of dislocations (see Figure 2-4). This behavior is consistent with the prediction of brittle vs. ductile modes of fracture using Rice's criterion [34].

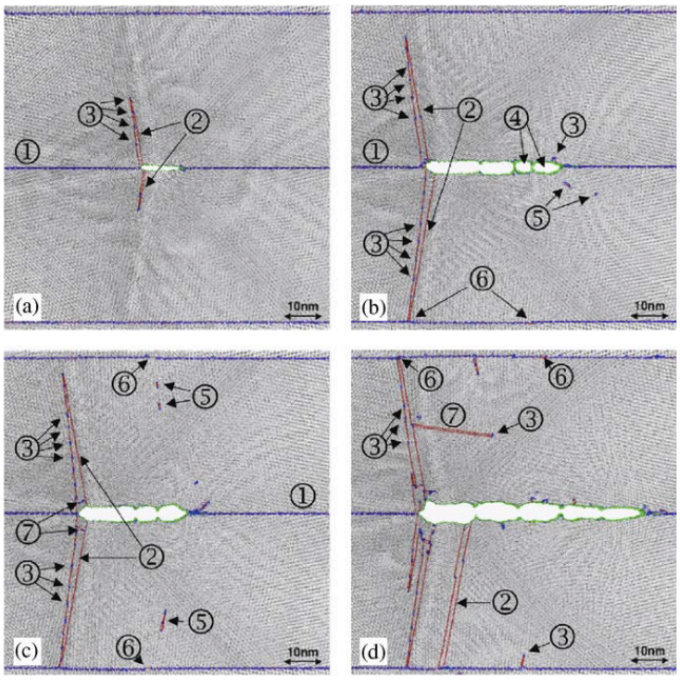

Figure 2-4: MD snapshots of cracks, which have propagated in the MD system. The right crack propagates in a brittle like manner with sharp tips while the right crack gets blunted and does not propagate [7].

However, Rice's criterion sometimes fails to predict the ductile vs. brittle response

of fracture, even for a 2D crack. Adlakha et. al. performed fracture simulation along seven <110> symmetric tilt GBs [60]. It is found that certain GBs (Σ9(221), Σ11(332) and Σ33(441)) show an absence of directional asymmetry in the observed crack growth behavior, in conflict with the Rice's criterion. This conflict is attributed to the complicated local structure of GBs, which change the stress state near the crack tip, causing dislocation emissions at a distance ahead of the crack tip.

To date, however, ductile vs. brittle behavior has only been studied in a small number of simple GBs. Most of them were performed in 2D or quasi-2D (thin) system. GB fracture even in some of these simple cases remains unexplained, e.g. the lack of fracture anisotropy mentioned above. In conclusion, there remains a lack of general understanding on how to relate ductile or brittle behavior to GB structure.

2.5.2 Calculation of fracture toughness

The fundamental thermodynamic criterion for crack extension is that the energy released from the specimen and loading system is sufficient to supply the energy needed to increase the area of the crack [65, 66]. Griffith found that, in the absence of plasticity, the energy required for crack extension is equal to the surface energy, γ_s, of the newly created crack faces [27]. Thus, the Griffith fracture criterion may be written as $G_c = 2\gamma_s$, where G_c is the critical energy release rate: the energy dissipated per unit of newly created crack area. Irwin subsequently showed that$-$in isotropic solids under plain strain [67]$-G_c$ and the mode I fracture toughness K_Ic are related by

$$K_{Ic} = \sqrt{\frac{EG_c}{1-\nu^2}}, \tag{2.1}$$

where E is Young's modulus and ν is Poisson's ratio.

Griffith's original fracture criterion does not apply to materials where crack extension is accompanied by plastic deformation [68, 69, 70]. Nevertheless, the notion of critical energy release rate is still valid and leads to the fracture criterion

$$G_c = w_p + 2\gamma_s \tag{2.2}$$

where the plastic work term, w_p, is generally much greater than $2\gamma_s$. For example, w_p is approximately 25 times $2\gamma_s$ for cleavage along a general grain boundary (GB) of copper embrittled by bismuth [71]. For low temperature transgranular cleavage of polycrystalline mild steel, w_p is approximately 500 to 1000 times $2\gamma_s$ [72]. In this manuscript, we describe a new method for determining G_c directly from atomistic simulations of fracture in the presence of plasticity.

Knowledge about the fracture toughness of GBs is of particular importance for GB engineering of structural materials [2] as well as investigations of polycrystalline materials at the macroscale [73, 74, 75]. However, it is challenging to determine the fracture toughness of individual GBs experimentally, as it requires the preparation of notched flat and defect-free GBs with defined misorientation. Atomistic simulations have an advantage in this context as well, as it is easy to construct atomic models containing specific GBs. Such models may be used to compute intergranular fracture toughness [76, 77, 78, 79, 80].

One way to estimate fracture toughness (and hence G_c) from atomistic simulations is to calculate the critical stress at which a crack in the material begins to grow [76, 77]. Then, using linear elastic fracture mechanics (LEFM) [25], K_{Ic} may be estimated based on the geometry of the specimen as well as the loading conditions. This approach is widely used to investigate the initial crack response [36, 7], but it cannot be used to calculate the post-yielding fracture toughness after the emission of dislocations from the crack tip.

Another method for the estimating fracture toughness in the presence of crack tip plasticity is the J-integral approach [78, 79, 80]. The J-integral is a path-independent surface integral that evaluates the driving force for crack propagation, commonly used in continuum-level simulations of deformation [81]. A key challenge in this approach is to create meaningful definitions of the required thermo-mechanical quantities in terms of atomic-level information [82, 83]. The J-integral has been applied to atomistic simulations of both brittle and ductile materials [79, 80].

Chapter 3

Methods

This chapter describes the methods used to study the intergranular fracture in Ni. The first section provides background on classical MD and describes the detailed fracture simulation techniques used in the subsequent chapters. The second section describes the methods for construction and finding equilibrium state of GBs. The last section provides a description of finite element method.

3.1 Atomistic simulation method

Fracture involves the processes at the atomic scale such as the rupture of atomic bonds and the rearrangement of atomic configurations near the crack tip. Atomistic simulation models materials at the level of atoms [85] and therefore are frequently used to study fractures processes in metals using classical MD simulations with empirical interatomic potentials.

3.1.1 Molecular dynamics

In MD, the atoms are allowed to interact with each other and their physical movements are simulated in the context of N-body simulation. The trajectories of atoms are determined by numerically solving the Newton's equations of motion for a system of interacting atoms, where the forces between the atoms are defined by

interatomic potentials. For each atom i, the equation of motion is,

$$\begin{aligned} \dot{r}_i &= \frac{p_i}{m_i}, \\ \dot{p}_i &= -\nabla_{r_i} U. \end{aligned} \tag{3.1}$$

where r_i, p_i and m_i represent the position momentum and mass for atom i. U denotes the potential energy.

The challenge of simulating intergranular fracture using MD is the computational cost. The fracture simulations are typically large on two folds: the number of atoms and the number of timesteps. A fracture system usually consists of cracks, GBs and free surfaces. In order to eliminate the effect of the artificial free surfaces on fracture behaviors, the system needs to be large, at least on the nano scales, in the direction perpendicular to the GBs as well as the crack propagation direction. For a fully 3D fracture simulation, the size in the third direction, which is along the crack front, also needs to be large, so that the non-uniform processes at different positions of the crack tip can be captured. To satisfy these size requirements, tens of millions of atoms must be simulated for a fully 3D intergranular fracture.

The number of timesteps for intergranular fracture is also large. In fracture simulations, the time between two successive loading increments need to be large enough so that the system can reach equilibrium before the next strain increment. The time to reach equilibrium depends on the deformation processes occurring in the system. When there are plastic deformations, it usually takes at least picoseconds to reach equilibrium. However, in metals, the size of timestep is constrained by the the vibrational motion of the atoms, which is on the scale of femtosecond. Therefore, tens of thousands of timesteps are necessary to simulate even one loading step and millions of timesteps are required for the whole fracture simulation.

Because of these computational demands, all MD fracture simulations in this thesis are performed using fast parallel code in LAMMPS [86]. Visualizations of atomic configurations during the fracture are performed using OVITO [87].

3.1.2 Interatomic potentials

A MD simulation requires a potential function by which the atoms in the simulation will interact. One simple choice is the pairwise potential, in which the total potential energy can be calculated from the sum of energy contributions from pairs of atoms. The pairwise potential requires the use of a volume-dependent energy to describe the elastic properties of a metal, which is sometimes hard to estimate. For example, the volume-dependent energy is ill-defined for calculations involving surfaces because the exact termination of the volume on an atomic scale at the surface is ambiguous. Therefore, other forms of approximation for describing the energy between atoms are required to accurate simulate fracture processes, where crack surfaces are involved,

The embedded-atom method (EAM), originally proposed by Daw and Baskes [88], is a many-body interatomic potential which can treat metallic systems in which fractures, surfaces and impurities can be included. The EAM potential energy is a sum of functions of the separation between atoms and neighbors,

$$E_i \;=\; F_\alpha\left(\sum_{i\neq j}\rho_\beta(r_{ij})\right) \;+\; \frac{1}{2}\sum_{i\neq j}\phi_{\alpha\beta}(r_{ij}). \tag{3.2}$$

where r_{ij} is the distance between atoms i and j, $\phi_{\alpha\beta}$ is a pairwise potential function, ρ_β is the contribution to the electron charge density from atom j of type β at the location of atom i, and F is an embedding function that represents the energy required to place atom i of type α into the electron cloud. EAM potential are particularly appropriate for metallic systems and are widely used in MD simulations.

To accurate simulation the fracture process, which usually involves creation of new surfaces as well as dislocation emissions from the crack tip, the potential needs to yield the correct physical properties of the metals. Among them, the surface and stacking fault energy are of particular importance for fracture simulations. In this thesis, we use the EAM potential developed by Angelo et.al [89]. for simulating fracture in Ni. Figure 3-1a shows the calculation of γ surface on the (111) plane in Ni using this potential. The stacking fault energy is then be calculated from the energy barrier in

the <112> slip direction along Cut 1 on γ surface (see Figure 3-1b). The estimated stacking fault energy $\gamma_s = 125.4 J/m^2$, which is very close to the experimental value $126 J/m^2$. Other mechanical properties of Ni, including elastic constants, surface energies and elastic modulus, calculated using this potential are list in Table 3.1.

Table 3.1: Mechanical properties of Ni predicted by EAM potential [89]

Parameter	Calculation
C_{11}	246 GPa
C_{12}	147 GPa
C_{44}	125 GPa
γ_{100}	2.06 J/m^2
γ_{110}	2.35 J/m^2
γ_{111}	1.93 J/m^2
Bulk modulus	180 GPa
Shear modulus	76 GPa

In Chapter 6, we performed simulations on the interactions between cracks with 3D microstructure of Pd. We use the EAM potential for Pd developed by Zhou et.al [90]. for this simulation. The predicted stacking fault energy by the EAM potential is $\gamma_s = 173.3 J/m^2$, which is very close to the experimental value $180 J/m^2$. Other mechanical properties of Pd predicted by this potential are listed in Table 3.2.

Table 3.2: Mechanical properties of Pd predicted by EAM potential [90]

Parameter	Calculation
C_{11}	247 GPa
C_{12}	200 GPa
C_{44}	57 GPa
γ_{100}	1.64 J/m^2
γ_{110}	1.75 J/m^2
γ_{111}	1.53 J/m^2
Bulk modulus	188 GPa
Shear modulus	46 GPa

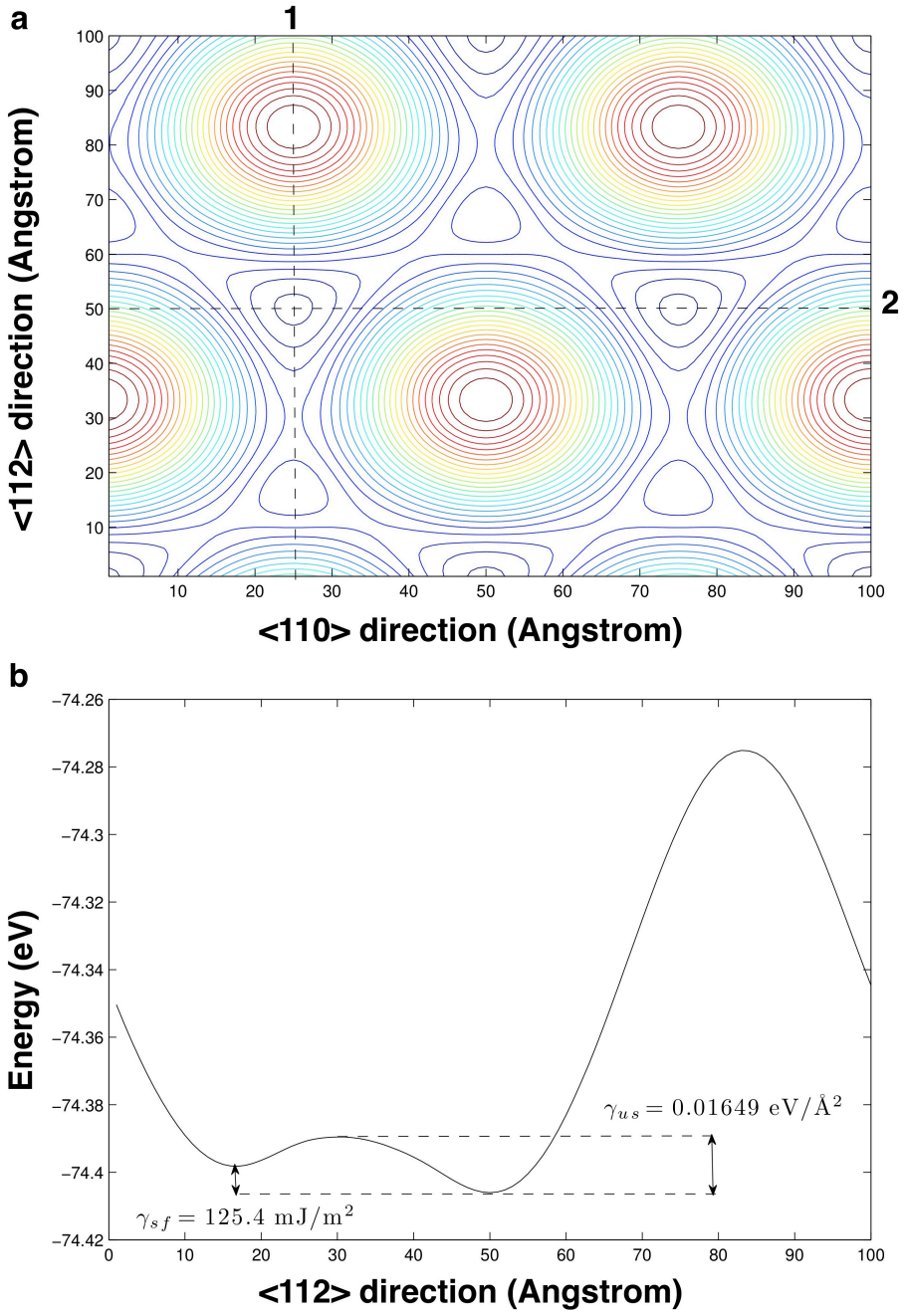

Figure 3-1: (a) Calculation of γ surfaces of the EAM Ni potential. (b) the stacking faulting energy are calculated from the energy barrier along the Cut 1 in the <112> directions on the γ surface.

3.1.3 Fracture simulation setup

Figure 3-2 shows a typical model for fracture simulations. We apply periodic boundary conditions along the crack front. The remaining model surfaces are free surfaces. All simulations are performed at a fixed temperature 10K using a Nosé-Hoover thermostat [91, 92].

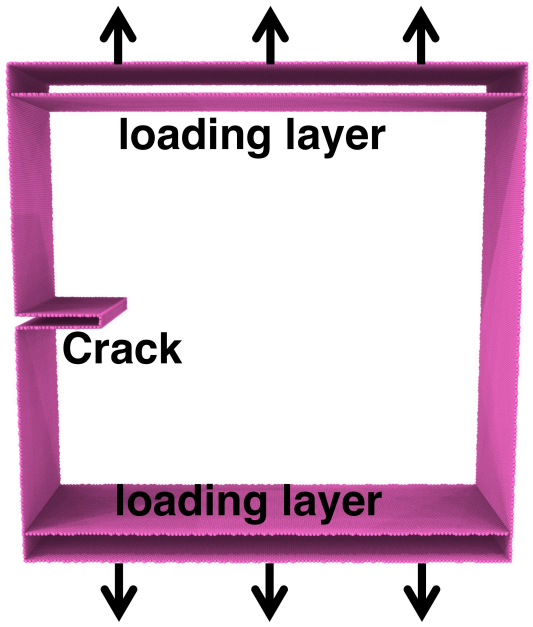

Figure 3-2: A typical model for fracture simulations.

During the simulation, uniaxial tension or shear loading is applied by displacement-control. We use a specially developed algorithm to apply the loading to our model without impeding the motion of emitted dislocations. The algorithm gradually applies vertical/horizontal displacements to thin loading layers on the top and bottom of the model, shown in Figure 3-2. To minimize stress fluctuations due to these incremental displacements, atoms in the interior of the model are also displaced such that the displacement field varies linearly with distance between the loading layers. Each loading increment corresponds to 0.1% tensile/shear strain and is followed by 5ps of MD relaxation, yielding an average strain rate of $2 \times 10^8/s$. The time of relaxation (5ps) is determined by the minimum time required for the system to reach

equilibrium. The center of mass position of each loading layer is constrained, but the relative positions between atoms within each layer may change, allowing dislocations to pass through the layers. Thus, dislocations emitted from the crack tip are not trapped in the model, as they would have been if the loading layers were rigid, and do not exert any back-stresses on the crack.

In fracture simulations, a crack can be introduced via two schemes. One approach is to turning off the interactions between atoms above and below the two dimensional crack surface, thus creating an artificial crack. The cracks introduced this way are extremely sharp with infinite curvature and may therefore promote brittle fracture, suppressing the emission of dislocations from the crack tip. Figure 3-3a shows the introduction of a <100> crack into single crystal Ni by turning off the interactions. Figure 3-3b shows the brittle propagation of this crack under uniaxial tension. However, the crack in the <100> direction in Ni usually extends in a ductile manner by emitting dislocations [93].

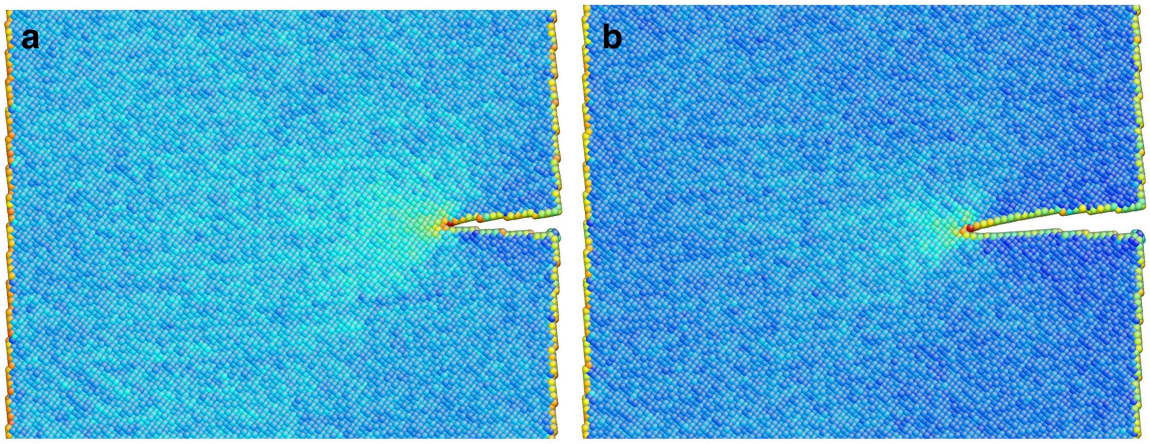

Figure 3-3: (a) Introduction of an atomically sharp crack by turning off the interactions between atoms above and below the crack surface. (b) Crack propagates by brittle fracture under uniaxial tension.

One way to solve this discrepency is to introduce the crack by removing atom layers and hence a crack with finite curvatures. The thickness of atoms removed needs to be greater than twice the cutoff distance of the potential so that there are no chemical interactions between the crack faces. Figure 3-4a shows the introduction of

a <100> crack by removing 1nm-thick of atoms into the same single crystal shown in Figure 3-3. The crack created this way is stable at zero stress when no external load is applied. Besides, it also yields the correct response of crack under uniaxial tension. Figure 3-4b shows dislocations are emitted from the crack tip during its propagation, which is in agreement with experiment observations [93].

In this thesis, the second scheme is adopted for creating the crack. The cutoff radius is $r_{cutoff} = 0.484nm$ for the Ni EAM [89] potential and $r_{cutoff} = 0.495nm$ for the Pd EAM potential [90]. Therefore, the thickness of atoms removed is 1nm for all the Ni and Pd simulations.

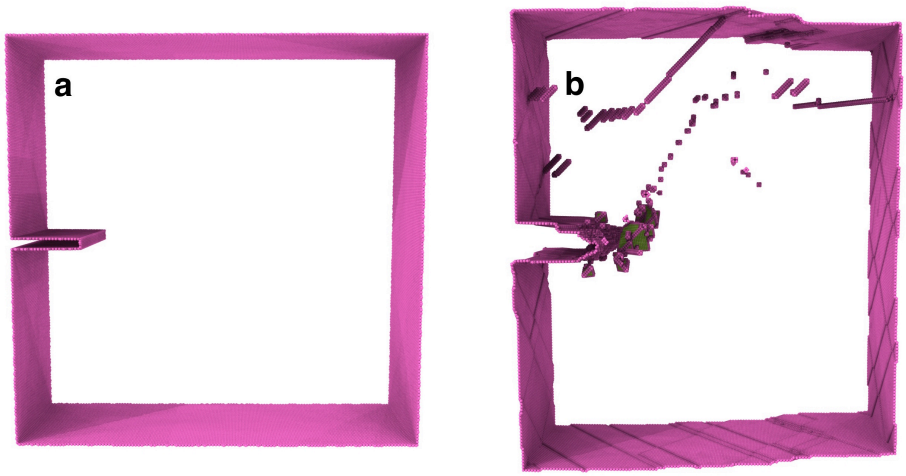

Figure 3-4: (a) Introduction of a crack by removing 1nm-thick of atoms. (b) Crack propagates by emitting dislocations under uniaxial tension.

3.2 Constructions of GBs

GBs that are studied in this thesis are coincidence site lattice (CSL) GBs. A CSL is a lattice formed from points where the two misoriented lattices happen to coincide [14]. The advantage of using CSL GBs (rather than general GBs) is that periodic boundary conditions can be applied in the two directions on the GB plane. This usually makes finding the equilibrium state of GB easier. The ratio of the volume of a CSL primitive cell to a crystal lattice primitive cell is denoted by Σ.

Given a CSL GB, the basis vector of CSL can be calculated using the method provided by Grimmer et.al. [94]. Let $R_A = (e_1^1, e_2^1, e_3^1)$ and $R_B = (e_1^2, e_2^2, e_3^2)$ denote the rotation matrices of the two grains, Grain 1 and Grain 2, separated by the GBs (see Figure 3-5). The transformation matrix from Grain 1 to Grain 2 is,

$$T = R_B R_A^{-1} \tag{3.3}$$

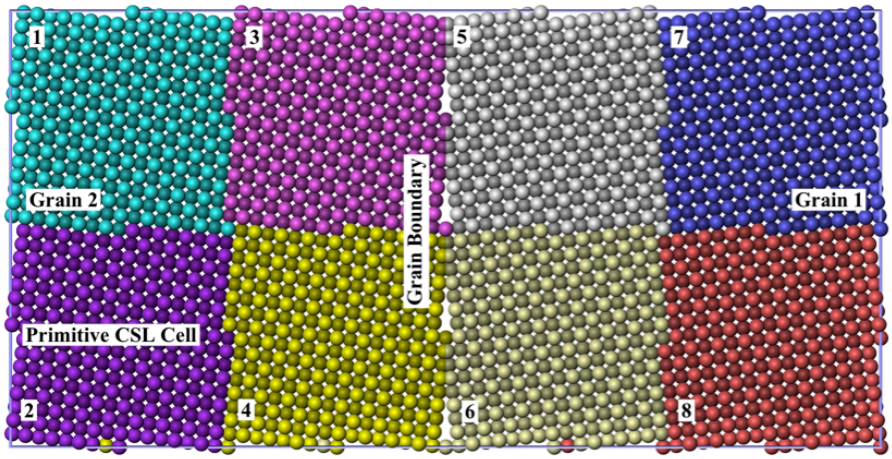

Figure 3-5: The initial structure of a CSL GB. Grain 1 and Grain 2 are separated by a vertical GB plane. Each color represent a CSL primitive cell.

T can be expressed in different reference lattices. Without loss of generality, let us chose the reference lattice such that $e_1^A = e_1^B$ parallel to the rotation axis. Then T will be of the form,

$$T = \begin{bmatrix} 1 & t_{12} & t_{13} \\ 0 & t_{22} & t_{23} \\ 0 & t_{32} & t_{33} \end{bmatrix}. \tag{3.4}$$

With this, the basis vectors for the CSL are,

$$\begin{aligned} e_1^{CSL} &= e_1^2, \\ e_2^{CSL} &= te_2^2, \\ e_3^{CSL} &= ne_2^2 + \frac{\Sigma}{t} e_3^2. \end{aligned} \tag{3.5}$$

Here t is the least common multiple of the denominators of t_{12}, t_{22} and t_{32}. n is the unique integer satisfying the condition,

$$n_i = n_t i2 + \frac{\Sigma}{t} t_{i3},$$
$$0 \leq n_i \leq t. \tag{3.6}$$

for i = 1, 2 and 3.

With the basis vectors of CSL cell for GBs obtained, the construction of GBs can be done by first repeating the primitive CSL cells in all three periodic directions, followed by removing atoms of lattice 1 on the right side of GB plane and removing atoms of lattice 2 on the left side of GBs. The as-constructed initial structure of a CSL GB is shown in Figure 3-5. Each color represents a CSL primitive cell.

To find the equilibrium structure of the GBs, Grain 1 is displaced with respect to Grain 2 along some vector on the γ surface of the GB to reach the minimum energy point. Figure 3-6 shows a typical γ surface calculated using MD for a $\Sigma 65 < 100 > (01\bar{8})$ GB. The atoms in Grain 1 is displaced on the γ surface to Point A (marked on Figure 3-6), which is the lowest energy point. Starting from this γ surface minimum, the GB is then annealed using MD for 5ps at 500K, and quenched to T=10K.

3.3 Finite element method

Finite element method (FEM) [95] is a numerical technique for solving partial differential equations (PDEs). In this thesis, we used the FEM implemented in the commercial software package COMSOL [96] to calculated the stress and displacement fields due to the defects in the model microstructure, such as cracks, free surfaces and disclination dipoles. For example, if we want to know the stress fields of a dislocation in a *finite* solids, the stress fields of the dislocation in a *infinite* solids as well as the image stresses due to the free surfaces are needed. The former usually has a closed-form expressions whereas the latter usually not, which requires numerical estimations. To compute this, linear elastic FE calculations are used with plain strain

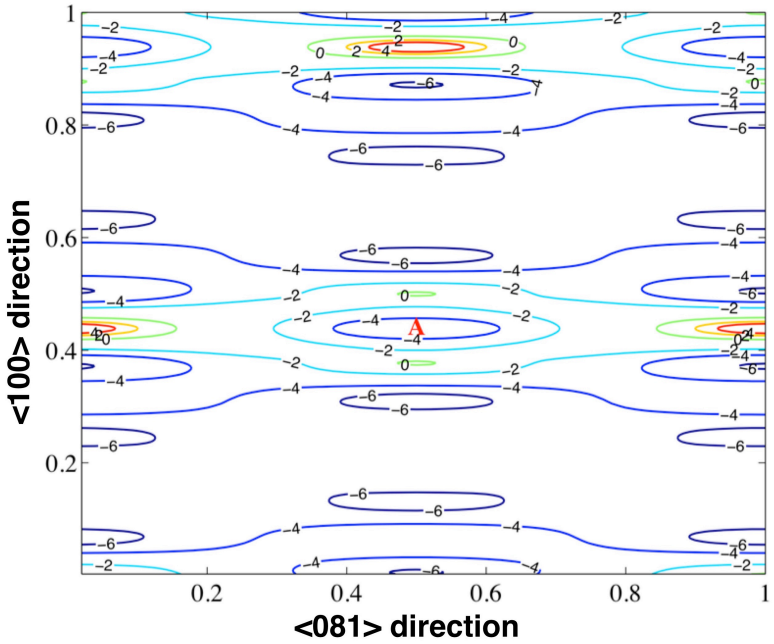

Figure 3-6: The γ surface of a $\Sigma 65 < 100 > (01\bar{8})$ GB

.

conditions. Using the elastic constants calculated from the atomistic simulations, the Zener anisotropy parameter for Ni is

$$A = \frac{2C_{44}}{C_{11} - C_12} = 0.799 \tag{3.7}$$

which is sufficiently close to unity for the material to be considered approximately isotropic for the purpose of this study.

A typical FEM model for calculating the stress fields in the atomistic model in Figure 3-2 is shown in Figure 3-7. Because of the mirror symmetry of the atomistic model, only half of it is used for the calculation.

The PDEs to be solved in the model are,

$$-\nabla \cdot (c \bigotimes \nabla u) = k, \tag{3.8}$$

where $k = [k_x, k_y]^T$ are body forces, $u = [u_x, u_y]^T$ are the displacements and $\bigotimes$ is the tensor product [97]. c is a rank four tensor, which can be written as four 2-by-2

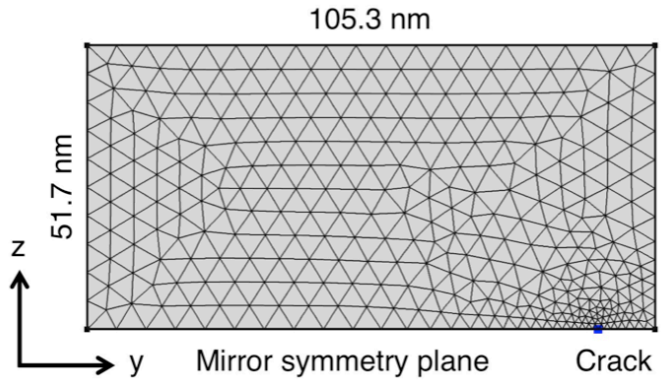

Figure 3-7: A typical FEM model

.

matrices:

$$
\begin{aligned}
c_{11} &= \begin{pmatrix} 2G+\mu & 0 \\ 0 & G \end{pmatrix} \\
c_{12} &= \begin{pmatrix} 0 & \mu \\ G & 0 \end{pmatrix} \\
c_{21} &= \begin{pmatrix} 0 & G \\ \mu & 0 \end{pmatrix} \\
c_{22} &= \begin{pmatrix} G & 0 \\ 0 & 2G+\mu \end{pmatrix}
\end{aligned} \tag{3.9}
$$

where G is the shear modulus and μ is defined by G and Poisson's ratio ν as,

$$\mu = 2G\frac{\nu}{1-\nu} \tag{3.10}$$

When there are no crystal defects in the model, free-traction boundary conditions are used for solving the PDEs. However, when the crystal defects (such as dislocations and disclinations) are present, the tractions t on the boundary are changed according to,

$$t = -\sigma_{defect} \cdot \hat{n} \tag{3.11}$$

where σ_{defect} is the stress tensor of the defect in an infinite solid and $\hat{n}$ is the unit outward normal to the surface.

Chapter 4

Characterizing atomistic fracture simulations

This chapter describes various methods for post-processing of atomistic fracture simulations, including estimation of crack extension, quantifying plastic deformations during the crack propagation and calculation of the critical energy release rate. We are going to use these methods to investigate the mechanisms and toughness of fracture along different GBs in Chapter 5.

4.1 Estimation of crack extension

One of the tasks for post-processing of fracture simulations is to measure the crack propagation distance. For pure brittle fracture, calculation of the crack propagation distance is trivial—simply by measuring the crack tip positions. However, in situations when crack propagates with plasticity, the tip of the crack gets blunted by the dislocations emitted from it and there are no well-defined crack tip positions. In this section, several methods that can be used to calculate the crack propagation distance in such situations are described.

4.1.1 Crack surface area

One approach is to estimate the crack extension with crack surface areas. To identify the crack surface from atomistic fracture simulations, we adopt an algorithm developed by Dupuy et. al. [98], which determines unambiguously the atoms that constitute the surface and meshes the surface with triangles. Their approach rolls a probe with radius R_s over the surface. Every atom touched by the probe is identified as a surface atom, as shown in Figure 4-1a. Following Dupuy et. al., we set $R_s = 0.35R_a$ where $R_a = 0.3nm$. Using this technique, we construct a crack surface mesh such as that in Figure 4-1b for all atomic configurations of interest. Both crack extension and crack tip blunting contribute to the total crack surface area A_{total}.

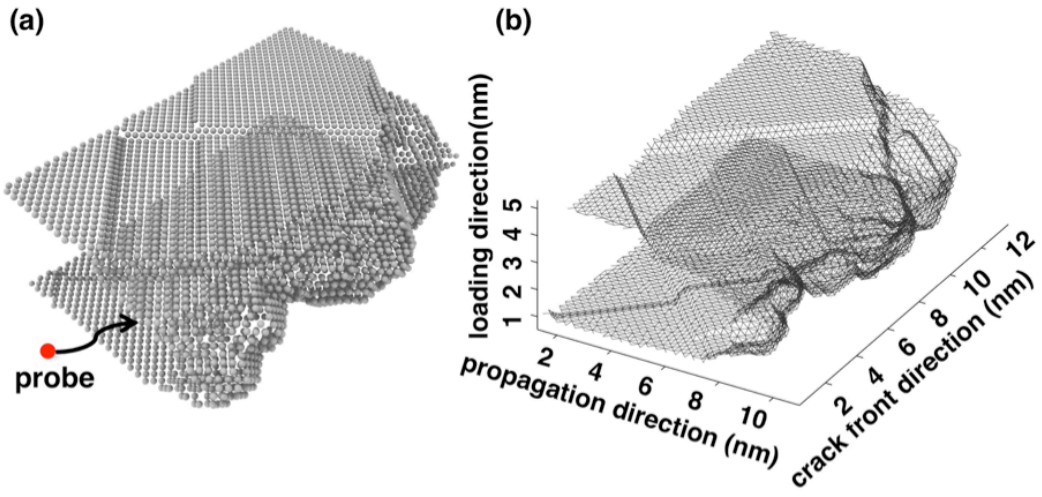

Figure 4-1: (a) Identifying surface atoms with a spherical probe. (b) Surface mesh constructed from the atomistic model in (a) using the method developed by Dupuy et al.

To estimate crack extension, the projected crack surface area A_{proj}, rather than A_{total}, is needed. To calculate just the part A_{proj} associated with crack extension, we project the crack surface onto the crack propagation plane, as illustrated in Figure 4-2a. This plane is identified by least squares fitting of the initial and final locations of the crack front. We calculate both the total and projected crack surface areas after every strain increment. Figure 4-2b plots these quantities as a function of strain for a

fracture simulation in the single crystal in Ni. During the initial elastic loading, there is no crack extension. At 4% strain, there is a sudden burst of crack advance with a velocity of about 100m/s. This crack speed is small compared to the Rayleigh wave speed in Ni: $c_R = 2887.6$m/s, for the potential we used. After the initial burst, the crack propagates through a series of intermittent advances with an average velocity of 5m/s. The first burst of crack propagation differs from subsequent ones because the crack starts out with a straight and defect-free front while, in later stages, the crack front becomes curved due to non-uniform propagation and damaged due to the emission and accumulation of dislocations. We view the state of the crack after the first burst as a more realistic representation of cracks in Ni.

4.1.2 Estimating crack tip positions

One straightforward method is to locate the position of a blunted crack tip and then estimate the crack extension by the difference between the initial and final positions of the crack tip. With the crack surface atoms identified, it is possible to determine the crack tip location with the apex of an elliptical curve fitted to atoms within a distance of ∼1.5nm to the tip (see Figure 4-3). With this method, we can also quantify the degree of bluntness with the radius of curvature at the crack tip. The crack tip radius of curvature ρ can be determined by

$$\rho = \frac{b^2}{a} \tag{4.1}$$

where a and b are the major and minor axes of the fitted elliptical curve.

4.1.3 Bond breaking analysis

Another way to measure the crack extension is to count the number of bond breaking events at the crack tip. The bond breaking events that we are interested in are those contributing to the creation of new crack surfaces. Not all of the debonding falls into this category, for example, when a dislocation moves in the bulk, the bonds between atoms on two sides of slip plane are broken but this does not leads to crack

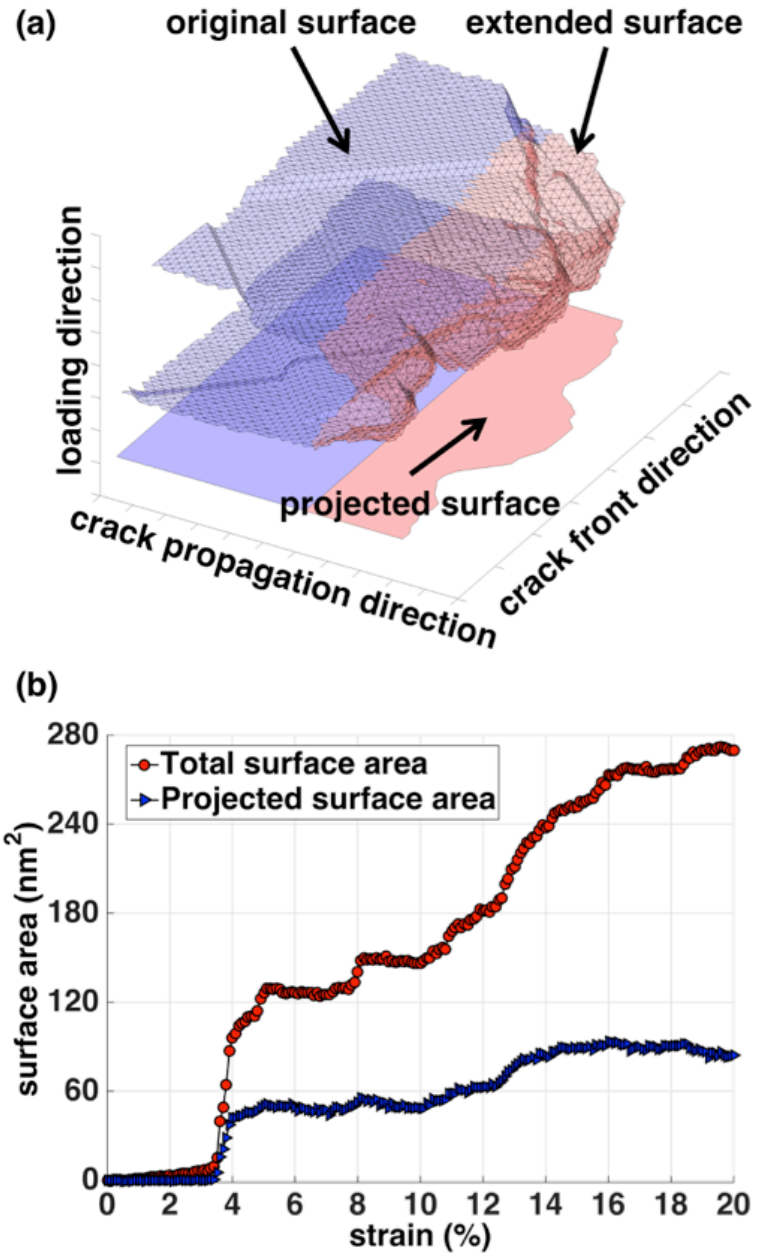

Figure 4-2: (a) The total surface area is calculated from the surface mesh, illustrated in Figure 4-1. The projected surface area is obtained by projecting the crack surface onto the crack propagation plane. (b) The total and projected crack surface area for a fracture simulation in the single crystal.

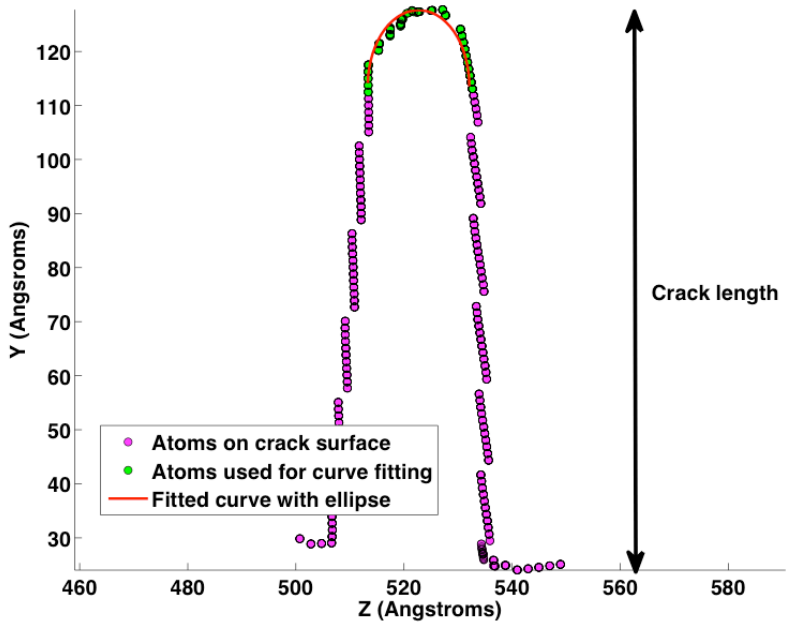

Figure 4-3: Crack surface extracted from simulations (atoms in purple). The crack tip (colored green) is fitted with an ellipse.

extension. In order to extract the right information from the bond breaking data, we require that the pair of atoms between which the bond breaks must be on the crack surface at the time of debonding.

The outcome of the debonding analysis is a list of position and time for each bond breaking event. Figure 4-4 shows a typical distribution of bond breaking events over time during a burst of crack propagation. It can been seen that the debonding process at the crack tip starts at ∼100 time step, with a peak at ∼280 time step.

4.2 Quantifying plasticity accompanying fracture

Crack propagation in FCC metals is usually accompanied by plastic deformations. Dislocation nucleation, glide and multiplication are the primary plastic deformation processes. In this section, several approaches for characterizing the dislocation processes are described.

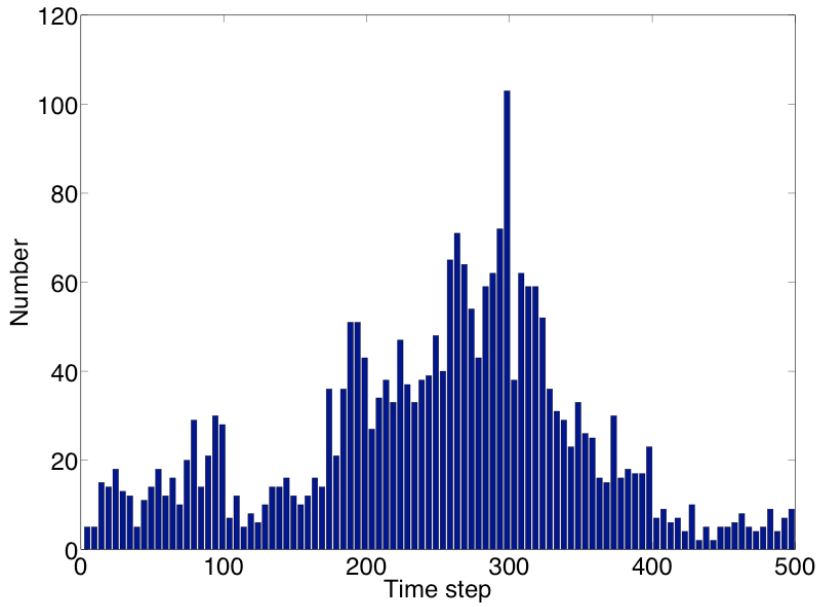

Figure 4-4: Histogram of bond breaking events over time during a burst of crack propagation.

4.2.1 Slip vector analysis

To detect nucleation and glide of dislocations, slip vector analysis proposed by Zimmerman et. al. can be used [99]. The slip vector of atom k is

$$s^k = -\frac{1}{n}\sum_{l\neq k}^{n}(x^{kl} - X^{kl}) \tag{4.2}$$

where n is the number of neighbors to atom k while x^{kl} and X^{kl} are the positions of atom l relative to atom k in the current and reference states, respectively. The slip vector of an atom represents how much the plastic slip of each atom is with respect to its neighbors. For example, when a dislocation loop is nucleated from the tip, atoms within the loop on two sides of slip plane will have slip vectors equal to the B'urgers vector of the dislocation.

The outcome of the slip vector analysis is a list of position and time for each slipping event. Figure 4-5 shows a typical distribution of slipping events over time in the vincinity of crack tip during a burst of crack propagation.

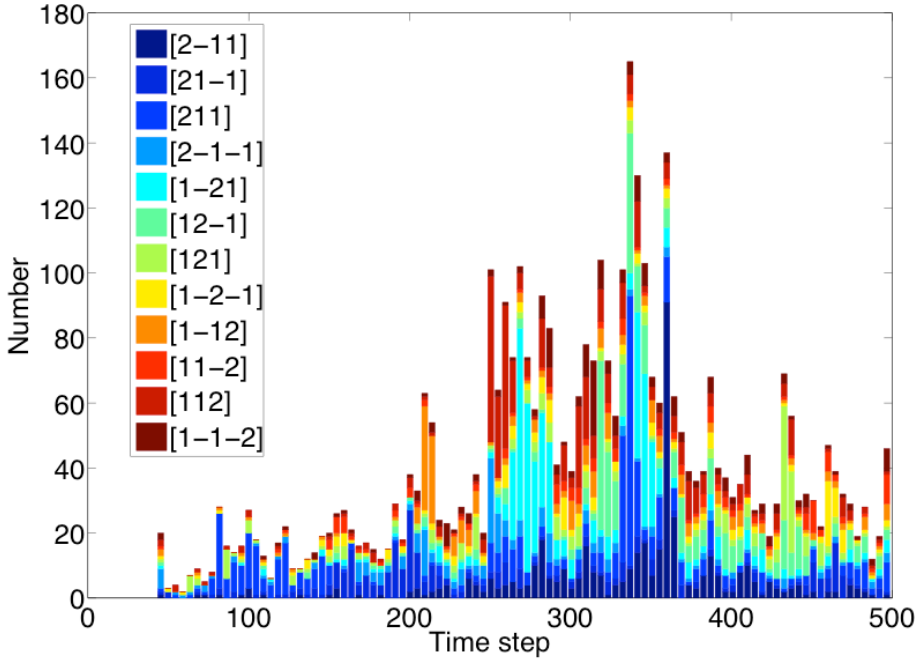

Figure 4-5: Histogram of slipping events over time during a burst of crack propagation.

4.2.2 Dislocation extraction

Slip vector analysis estimates the degree of slipping for each atoms, however, it cannot provide information such as the lines of the dislocations. Dislocation extraction algorithm (DXA) developed by Stukowski [100] can identify dislocation defects in atom-position datasets generated by atomistic simulations. The algorithm converts all identified dislocations into continuous lines and computes their Burgers vectors in a fully automated fashion. Figure 4-6 shows an example of identifying the configuration of nucleated dislocation at the crack tip during fracture using DXA.

4.2.3 Plastic work density

We estimate the plastic work density ρ_{pw} based on the spatial distribution of dislocation slip. ρ_{pw} contains information concerning the shape of the region where plasticity contributes most to the toughness of fracture. The amount of plastic work

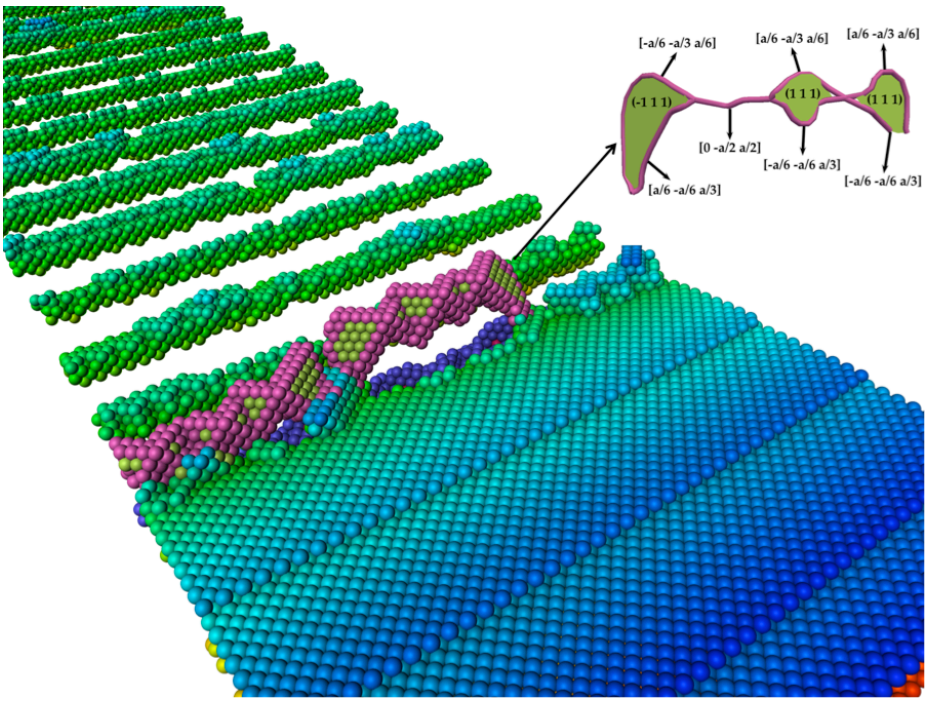

Figure 4-6: Dislocation configurations identified from atomistic fracture simulations using DXA.

dW_p done by the motion of a dislocation in a stressed solid is [101],

$$dW_p = b \cdot \sigma dS \tag{4.3}$$

where b is the Burgers vector of the dislocation, dS is the area swept by the gliding dislocation, and σ is the stress acting on the dislocation.

To estimate dS, the area swept by dislocations on {111} planes in FCC Ni, we find the number of slipped atoms using slip vector analysis [99]. Every such atom contributes a slip area of $\sqrt{3}a_L^2/4$, where a_L is the equilibrium cubic lattice parameter of Ni. Therefore, dS is

$$dS = \frac{\sqrt{3}}{4}a^2\frac{N}{2}, \tag{4.4}$$

where N is the total number of slipped atoms. An atom is considered a slipped atom if its slip vector s satisfies, $||s - b|/||b|| < 0.05$, i.e. if its slip vector is within 5% of Burgers vector, b. When identifying slipped atoms, we consider all the 12 slip

systems in FCC Ni.

To validate this method of calculating swept area, we apply it to three test cases: glide of a straight edge dislocation dissociated into Shockley partials (see Figure 4-7a), expansion of a circular dislocation loop (see Figure 4-7b), and expansion of two nested dislocation loops (see Figure 4-7c). In all three cases, the computed slip area was within 4% of the true slip area, which is known a priori.

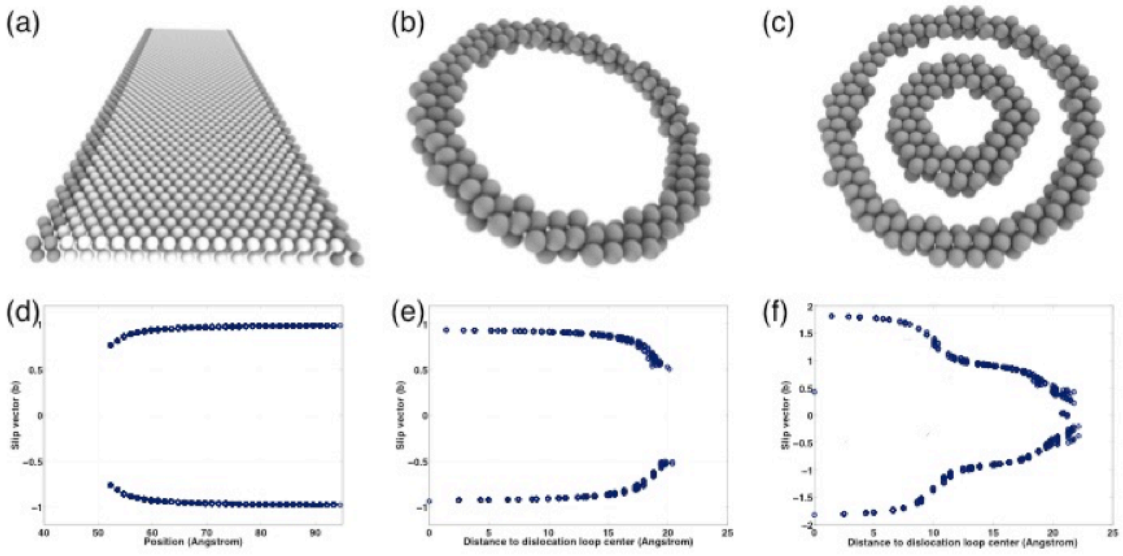

Figure 4-7: Verification of methods for slip area estimation with (a) straight-line dislocation with 5nm width, (b) dislocation loop with 2nm radius and (c) concentric dislocation loops with 1nm and 2nm radius. Slip vectors of atoms displaced by the (d) straight-line dislocations, (e) dislocation loop and (f) concentric dislocation loops.

With the slip area calculated, we estimate the plastic work using Equation 4.3. Unfortunately, there is no clear way to obtain the external stress σ acting on each dislocation. Our atomic models only allow us to compute total stresses, $\sigma_t = \sigma_e + \sigma_d$, which are a superposition of σ as well as the stresses of the dislocation itself, σ_d. Therefore, as a simplifying assumption, we assume that σ is uniform and equal to the applied tensile stress. This assumption ignores any stresses exerted by the crack or other lattice defects.

The estimated plastic work density for intergranular fracture is visualized in Fig. Figure 4-8. Bright regions correspond to intense dislocation activity and hence high

plastic work density. The initial crack length at zero stress is marked by white lines in Figure 4-8. A striking feature of these plastic work density distributions is that most of the plastic work is localized in distinct slip bands that originate at the crack tip and end at a free surface.

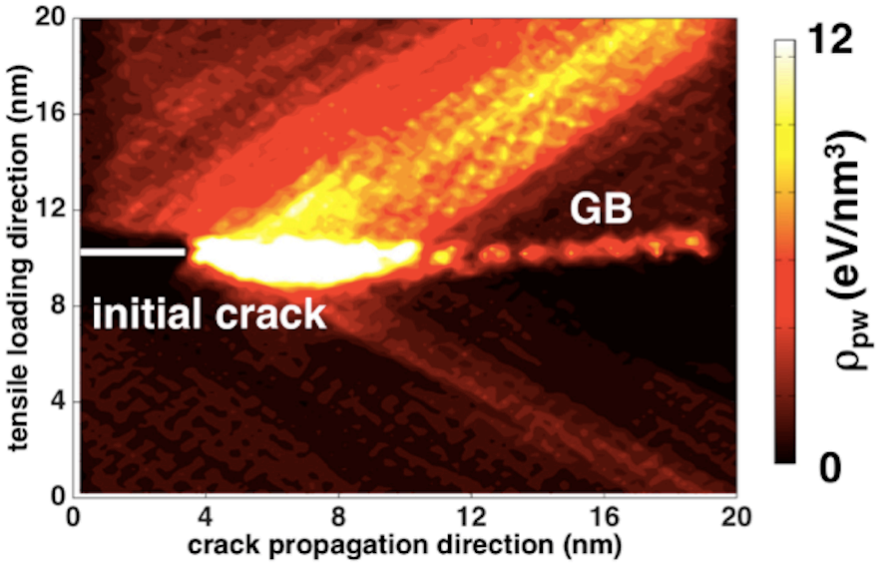

Figure 4-8: Plastic work density distribution for intergranular fracture.

4.3 Critical energy release rate

The critical energy release rate, G_c, is the energy dissipated during fracture per unit area of crack extension [66],

$$G_c = -\frac{\partial(U - W)}{\partial A_{proj}} \tag{4.5}$$

where U is the internal energy, W is the work done by external loads, and A_{proj} is projected crack surface area calculated by projecting the total surface area A_{total} onto the plane of crack extension. This quantity, G_c, is the energy that must be supplied to the crack tip for the crack to extend. In the transgranular fracture simulations described above, the average crack path is approximately along (010) surfaces with

surface separation energy of $2\gamma_{100} = 4.12 J/m^2$ (see Table 3.1). However, in view of the prominent dislocation activity in the fracture simulations, we expect that G_c will far exceed $2\gamma_{100}$.

Two quantities are needed to estimate G_c in our simulations: the projected crack surface area A_{proj}, which is discussed in the previous section, and the energy dissipated during crack advance, which will be discussed in the following section.

4.3.1 Estimating energy dissipated during fracture

To determine the energy dissipated during crack advance, we compute the work, W, done by external loads:

$$W = \int_{L_y}^{L'_y} f(y)\mathrm{d}y \approx \sum_i f(y_i)\Delta y \tag{4.6}$$

Here, $f(y_i)$ is the tensile force acting on the centers of mass of the loading layers at the i^{th} strain increment and Δy is the subsequent relative displacement of the layers. During crack propagation, part of this external work is stored as internal energy, U, while the remainder is dissipated either by creation of new crack surfaces or through plasticity. U is the sum of the potential energy of the model (determined from the EAM potential for Ni [89]) and the total kinetic energy of all the atoms in the model. The energy dissipated during fracture is simply the difference between W and U.

Figure 4-9 illustrates one example of the calculation of external work and internal energy during crack propagation. For reference, it also shows the tensile stress-strain curve for this simulation. Initially, both W and U rise parabolically with strain at the same rate, signifying that no energy is being dissipated. This behavior is to be expected, as the model deforms elastically during the first $\sim$4% of strain and all the external work is stored as elastic strain energy. After the onset of plastic deformation, a large fraction of the external work done is dissipated.

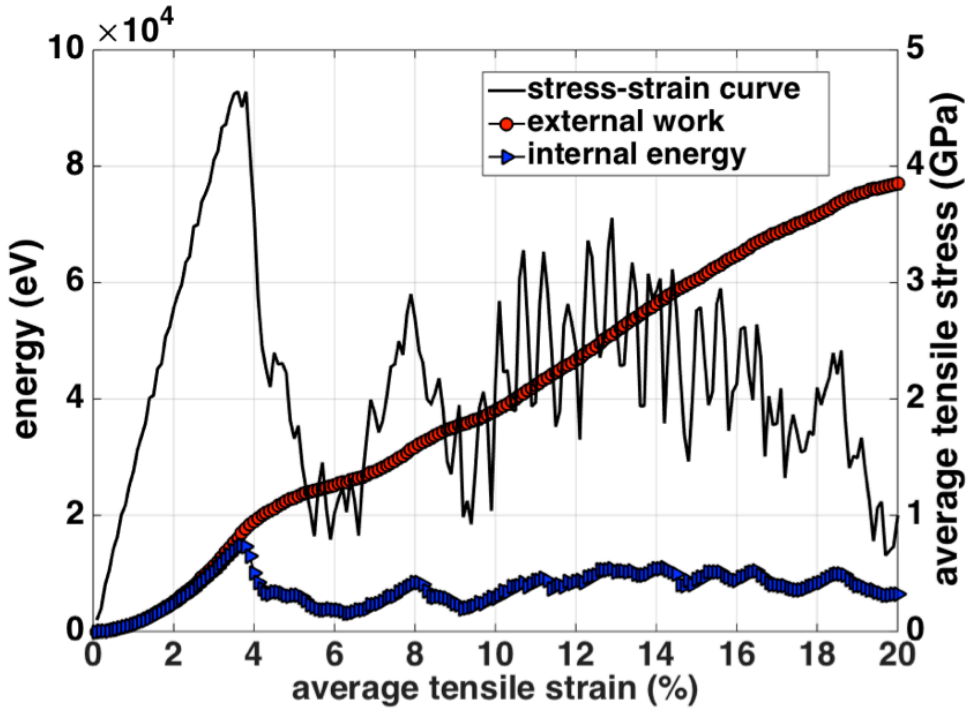

Figure 4-9: One example of external work, internal energy, and average tensile stress during fracture.

4.3.2 Calculation of critical energy release rate

Having calculated the projected crack surface area and dissipated energy, we estimate G_c using Equation 4.5. Figure 4-10 plots the energy dissipated, W-U, against the projected crack surface area for the fracture simulation. G_c is the slope of this plot. It varies considerably during loading. Its value is positive on average, but there are regions on the plot with negative G_c. They indicate partial crack closure due to rapid elastic unloading of the vicinity of the crack tip after a burst of crack advance. For comparison, Figure 4-10 also plots a straight line with slope $2\gamma_s = 4.12 J/m^2$, corresponding to pure brittle fracture according to the Griffith criterion. The area between this line and the (W-U) vs. A_{proj} plot is w_p. It is the origin of the plastic work contribution to G_c given in Equation 2.2. As expected, w_p is much larger than $2\gamma_s$.

Figure 4-10 shows two distinct stages of crack propagation. In the first stage, from a projected crack area of 0 to $29nm^2$ (marked by the shaded region in Figure 4-10,

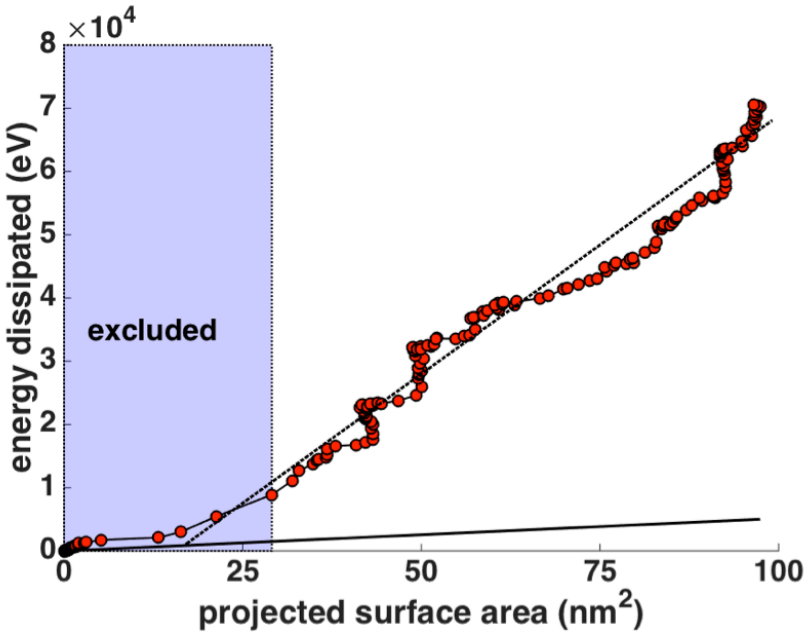

Figure 4-10: G_c is estimated as the slope of a line fitted to the plot of dissipated energy vs. projected crack surface area. Data points in the shaded region are excluded from the fit.

the crack propagates in a brittle-like manner, with $G_c \approx 2\gamma_s$. This stage corresponds to the propagation of a straight, clean crack into a perfect, defect-free Ni single crystal. During the second stage, when the projected area increases beyond $29nm^2$, the crack is curved and damaged. As mentioned above, we consider this stage to be more representative of crack propagation in Ni than the fist stage. We determine the average critical energy release rate during the second stage as the slope of the line fitted to the (W-U) vs. A_{proj} plot. For the simulation in Figure 4-10, we find $G_c = 62.4 \pm 1.9 J/m^2$, i.e. $\sim$15 times higher than $2\gamma_s$. All further G_c values reported in this thesis are determined this way.

Chapter 5

Intergranular fracture in Ni

In this chapter, we use large-scale MD simulations to investigate the mechanisms and toughness of crack propagations along different GBs in Ni. By analyzing the fracture processes, three distinct fracture mechanisms are identified: (1) crack propagation by slipping of atoms at its tip due to emission of dislocations, (2) decohesion restrained by emission of dislocations (DRED) and (3) continuous brittle crack propagation without arrest due to local hardening mechanism. The critical energy release rates for crack propagations with these mechanisms are also calculated and compared.

5.1 Intergranular fracture simulations

Large-scale atomistic fracture simulations are performed along coherent twin boundaries with cracks oriented in the $[11\bar{2}]$ and $[1\bar{1}0]$ directions as well as $\Sigma 65<100>$ symmetrical tilt GB with tilt angle $\theta = 14.25°$. This section describes the model construction and the simulation results along these GBs.

5.1.1 Fracture along coherent twin boundaries

Figure 5-1 shows the setup of our atomistic simulation of intergranular fracture along coherent twin boundaries with different crack orientations. Periodic boundary conditions are applied in the z direction with free surfaces in the x and y directions.

The initial crack configuration is created by removing atoms of 1nm thick with length equal to 1/5 of the box size in the x direction (see Figure 5-1). Uniaxial tensile strain is applied in the y direction using a displacement-control loading method described in Chapter 3 with a strain rate of $2 \times 10^8/s$.

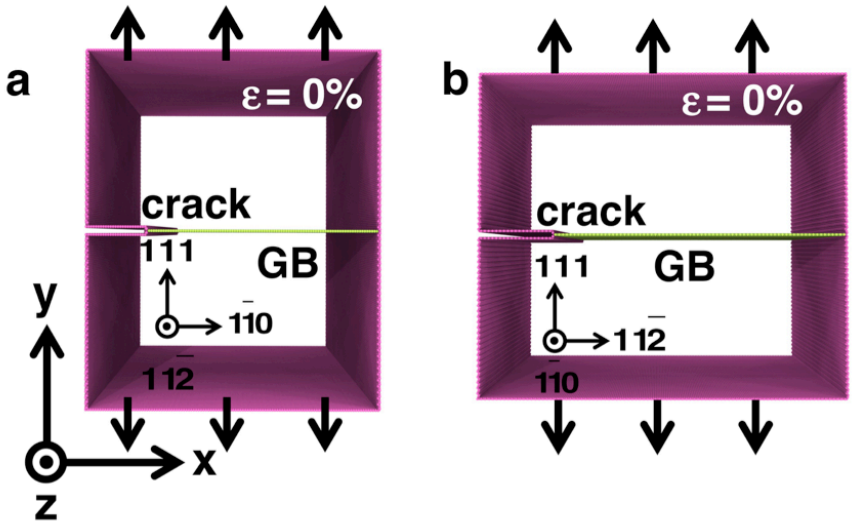

Figure 5-1: Simulation setup for intergranular fracture along coherent twin boundaries with crack oriented in the (a) $[11\bar{2}]$ and (b) $[1\bar{1}0]$ direction.

Table 5.1: Summary of simulation configurations

GB	Crack orientation	Dimensions x | y | z (nm)	Atoms
Twin boundary	$[1\bar{1}0]$	41.3 | 36.6 | 29.9	4147200
Twin boundary	$[11\bar{2}]$	29.9 | 36.6 | 41.3	4147200

The orientations of slip planes with respect to the crack front for the two simulation models (see Figure 5-1) are shown in Figure 5-2 and Figure 5-3. The (111) slip plane is the twin boundary plane and hence omitted. The $[11\bar{2}]$ crack does not lie in any of the $(\bar{1}11)$, $(1\bar{1}1)$, or $(11\bar{1})$ slip planes. Therefore, the dislocation process accompanying the propagation of $[11\bar{2}]$ crack is inherently 3D and precludes the use of a quasi-2D model. For the $[1\bar{1}0]$ crack, it is contained in the $(11\bar{1})$ slip plane. However, the $(\bar{1}11)$ and $(1\bar{1}1)$ slip planes are oblique to the crack front. Dislocation processes on

these oblique slip planes may be locked out if a 2D model is used. Therefore, for both simulations, 3D models with large size in the periodic direction are used. The detailed information about the computational models, including the size and crack orientation, is listed in Table 5.1.

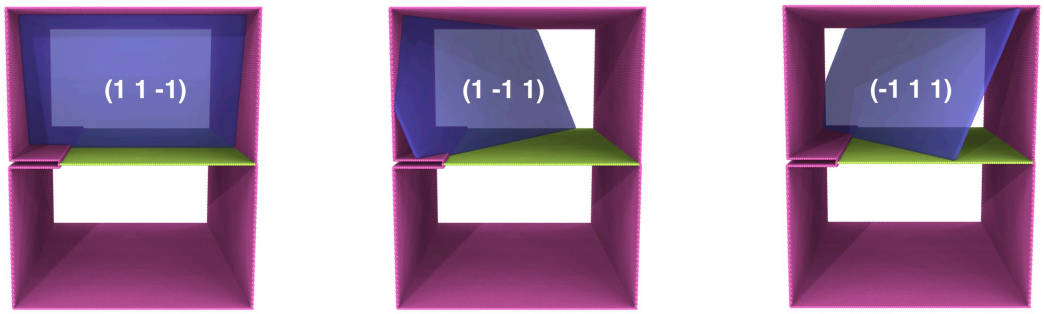

Figure 5-2: The orientation of slip planes with respect to the $[11\bar{2}]$ crack front on coherent twin boundary

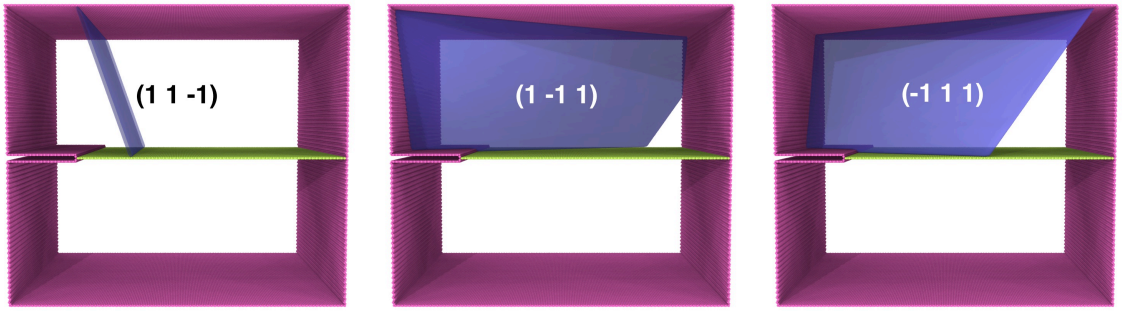

Figure 5-3: The orientation of slip planes with respect to the $[1\bar{1}0]$ crack front on coherent twin boundary

Figure 5-4a and b shows two stages of the fracture simulation on the bicrystal containing twin boundary with crack oriented in the $[11\bar{2}]$ direction. The model first deforms elastically up to a tensile load of ∼4GPa at 1.7% strain, whereupon Shockley partial dislocation loops begin to nucleate and emit from the crack tip (see Figure 5-4a). The crack tip is blunted by the continuous emission of dislocations. As we load

the model to ∼10% average tensile strain, the crack extends, but only by a small distance.

For the twin boundary fracture simulation with a crack oriented in the $[1\bar{1}0]$ direction (see Figure 5-1b), the crack propagation behavior is dramatically different from what we have seen with the $[11\bar{2}]$ crack. After the initial elastic deformation, the crack begins to propagate in a brittle-like manner at 1.7% tensile strain with nucleation of stacking fault tetrahedra from its tip (see Figure 5-5a).

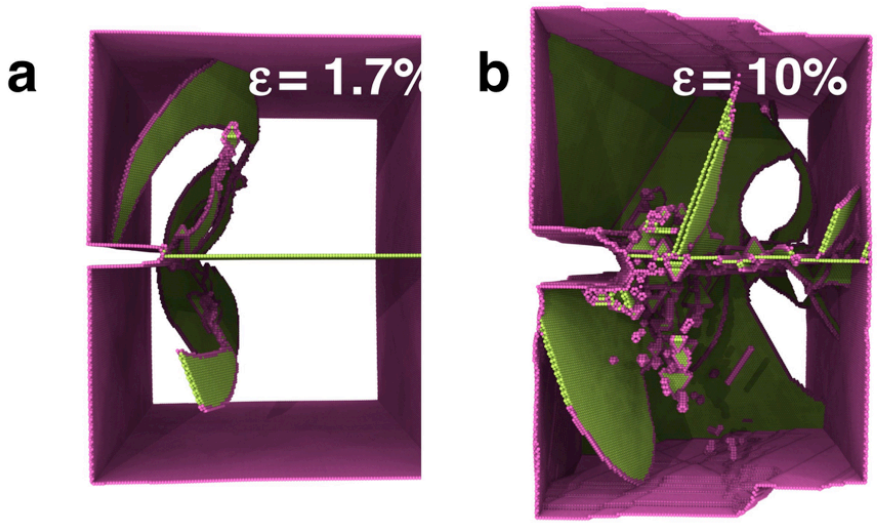

Figure 5-4: Intergranular fracture along coherent twin boundaries in Ni bicrystal model with cracks oriented in the $[11\bar{2}]$ direction. At the onset of fracture, (a) mobile Shockley partial dislocations are emitted from the $[11\bar{2}]$ crack. (b) The $[11\bar{2}]$ crack propagates with extensive plasticity and blunted tips.

From the stress-strain curve shown in Figure 5-6, it can be seen that, for simulations with crack oriented in the the $[1\bar{1}0]$ direction, the tensile stress continues to increase after the initial dislocation nucleation. As the load further increases, the stacking fault tetrahedron becomes unstable and the dislocations in the lock become mobile at 2.6% tensile strain. Deformation twins begin to nucleation from on the GB ahead of the crack tip at 3.0% tensile strain (see inset of Figure 5-6). Despite the surrounding plasticity, the crack tip remains sharp. As we load the model to ∼10% average tensile strain, the crack extends for a much longer distance than the $[11\bar{2}]$

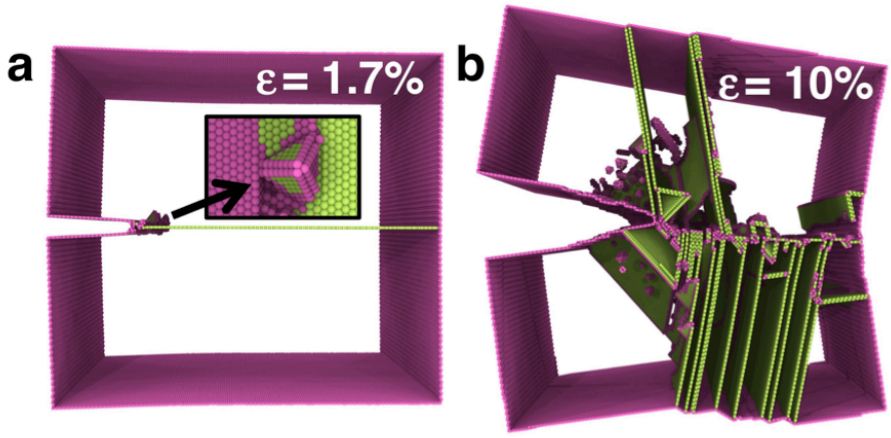

Figure 5-5: Intergranular fracture along coherent twin boundaries in Ni bicrystal model with cracks oriented in the $[1\bar{1}0]$ direction. At the onset of fracture, (a) sessile stair-rod dislocations are nucleated at the tip of $[1\bar{1}0]$ crack. The $[1\bar{1}0]$ crack extends in a brittle-like manner with relatively sharp tips.

crack.

The atomic configuration at the tip of the $[11\bar{2}]$ and $[1\bar{1}0]$ crack at different stages of fracture is shown in Figure 5-7. It can be clearly seen that the $[11\bar{2}]$ crack gets much blunted and almost does not propagate while the $[1\bar{1}0]$ remains relatively sharp and extends for a long distance..

5.1.2 Fracture along Σ65<100> symmetrical tilt GB

Figure 5-8 shows the geometry of our model with Σ65<100> symmetrical tilt GB. It contains a crack whose front lies along the <100> tilt axis of the GB. Under mode I loading, this configuration generates a lower resolved shear stress for dislocation glide than cracks with fronts along <110> or <112> directions in single crystals, making dislocation nucleation from the crack tip more difficult. Moreover, all dislocations are emitted on slip planes oblique to the crack front (see Figure 5-9) and are therefore less efficient at blunting the crack. This process is inherently 3D and precludes the use of a quasi-2D model geometry. The boundary condition in the direction of the crack front is periodic and the model has free surfaces in the remaining two orthogonal directions. The model has dimensions of $14.2nm \times 85.1nm \times 85.1nm$ with periodic boundary

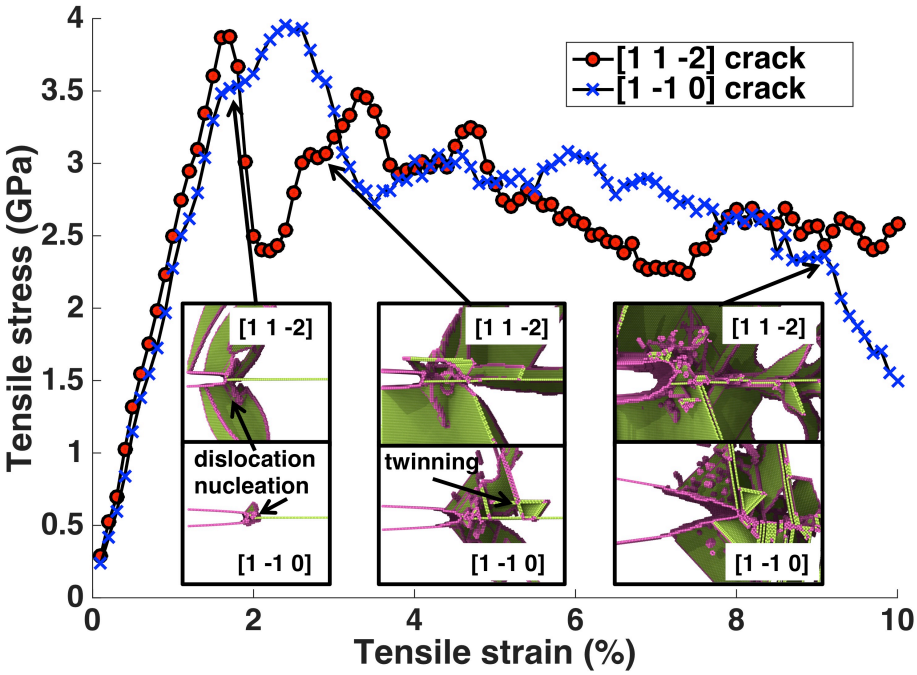

Figure 5-6: Average stress vs. average strain for the intergranular fracture simulation along coherent twin boundaries. Insets show atomic configuration near the crack tip at the onset of dislocation nucleation, deformation twining and at the end of the simulation.

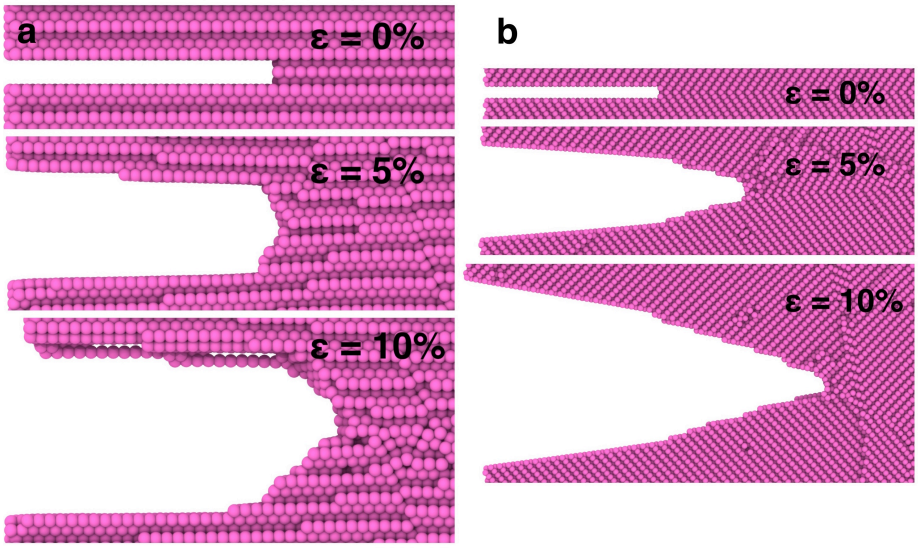

Figure 5-7: Atomistic configurations at the tip of the (a) $[11\bar{2}]$ and (b) $[1\bar{1}0]$ crack at different stages of fracture.

conditions in the x-direction and free surfaces in the y- and z-directions. It contains 9341200 atoms. A crack is created by removing atoms in a $14.2nm \times 14.2nm \times 1nm$ layer, as shown in Figure 5-8). The crystallographic orientation of Grain 1 in Figure 5-8 is x = [100], y = $[01\bar{8}]$, z = [081] while the orientation of Grain 2 is x = [100], y = $[0\bar{1}\bar{8}]$, z = $[08\bar{1}]$.

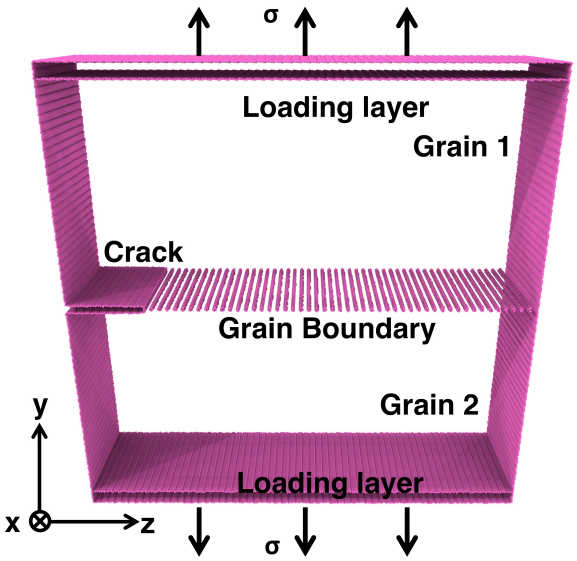

Figure 5-8: Ni bicrystal model with a nanocrack.

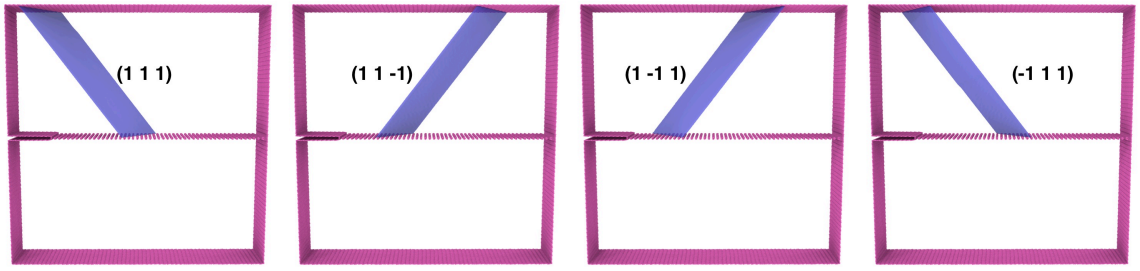

Figure 5-9: The orientation of slip planes with respect to the crack front on symmetrical tilt GB

The series of images in Figure 5-10 illustrates the outcome of our simulation. After an initial period of elastic deformation, the crack extends in a sudden burst accompanied by profuse dislocation emission, as shown in Figure 5-10a. After propagating for ∼2nm, the crack is arrested and all dislocations move out of the model, leaving

the surrounding environment relatively clean, as depicted in Figure 5-10b. Further loading leads to three additional bursts with similar behavior. Figure 5-10c shows the onset of the third burst and Figure 5-10d illustrates the state of the model after the burst. The crack advances by ∼2nm during each burst, yielding a total propagation distance of 8.4nm at the end of the simulation.

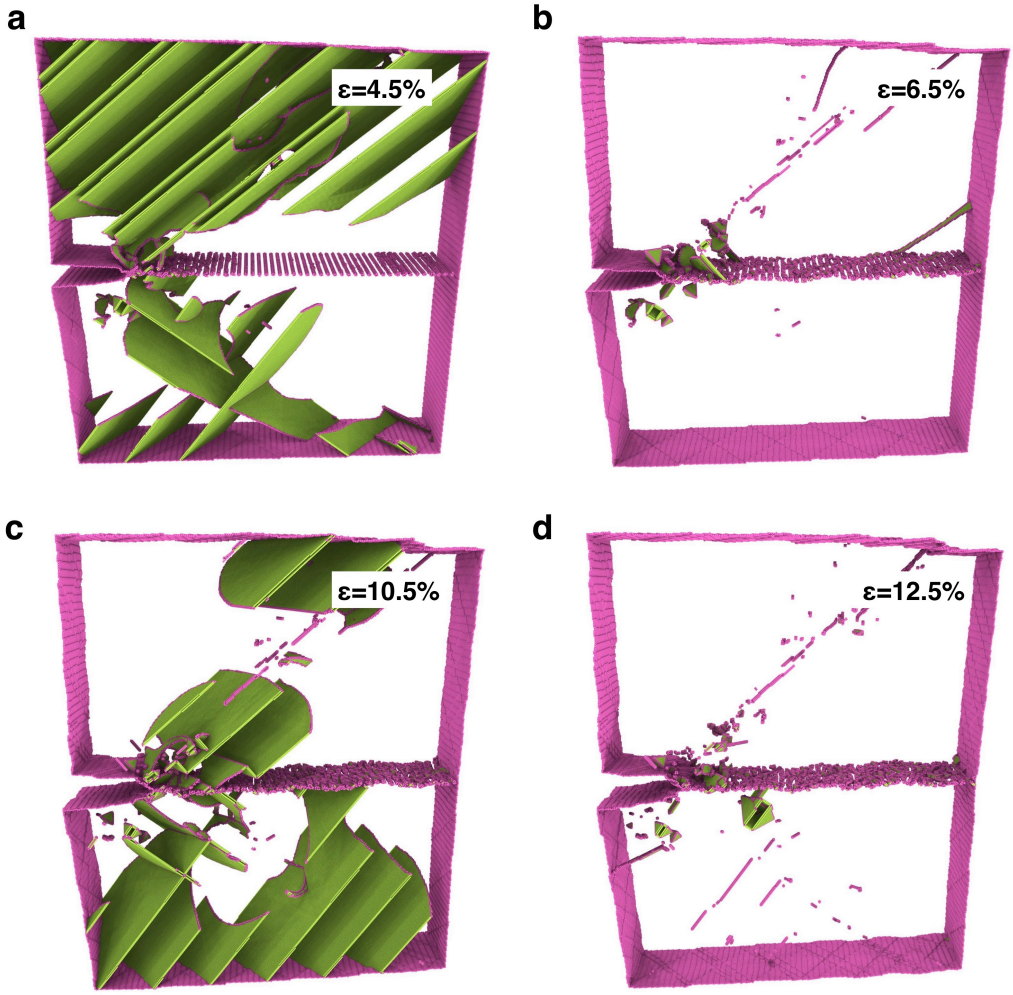

Figure 5-10: Intergranular fracture along a <100> tilt GB in Ni. The crack propagates in bursts accompanied by copious dislocation emission. Onset (a) and aftermath (b) of the first burst. Onset (c) and aftermath (d) of the third burst.

Figure 5-11 shows the crack tip configuration at different stages of the fracture. It can be seen that the crack tip remains sharp after each burst, despite the copious dislocations emitted from it. We repeated this simulation for other GB tilt angles

and observed similar outcomes.

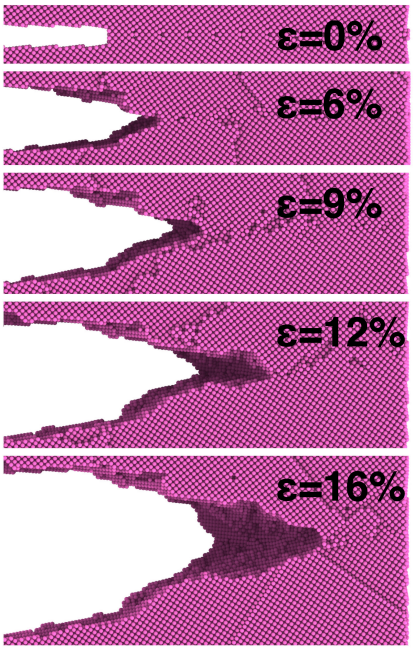

Figure 5-11: Atomistic configurations near the crack tip at different stages of fracture. The crack tip remains sharp as it propagates.

Figure 5-12 plots the average tensile stress vs. the average tensile strain during the simulation. The first burst begins after linear elastic deformation to 3.7GPa and 1.9% strain (see inset of Figure 5-12). The stress drops as the crack advances and as dislocations emitted from the crack propagate out of the model. By the end of the first stress relaxation (∼5.5% strain), the crack has been fully arrested and elastic loading resumes. This sequence of events repeats three more times during the simulation: elastic loading is followed by a burst of crack advance and eventual crack arrest. While the first burst of crack propagation initiates at a stress of 3.7GPa, the remaining bursts begin at lower stresses of ∼2.7GPa. These differences are due to the changing structure of the crack tip during the simulation: initially, the crack tip is defect-free and therefore lacking in preferential sites for dislocation emission and bond breaking. By contrast, the crack tip environment is significantly more distorted prior to subsequent bursts, due to the accumulation of dislocation debris and damage from new surface creation.

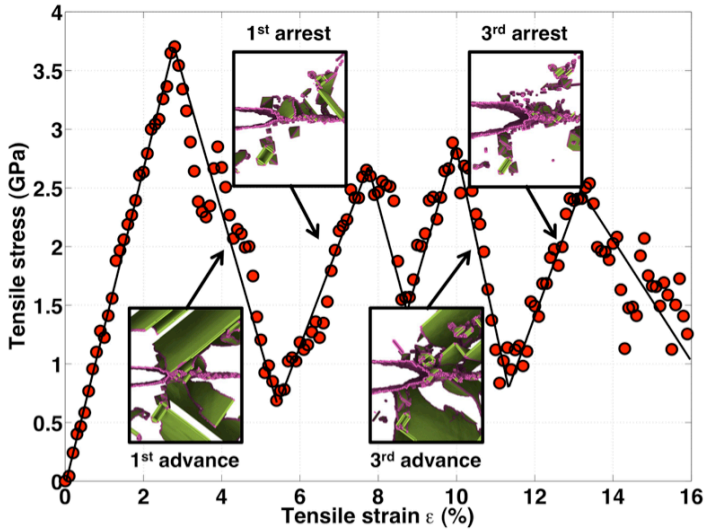

Figure 5-12: Average stress vs. average strain for the intergranular fracture simulation. Stress drops correspond to bursts of crack advance (shaded). Insets show the atomic configuration near the crack tip during and after the burst (perfect FCC atoms not shown).

In summary, three simulations of intergranular fracture are performed. Distinct crack propagation behaviors are observed and summarized below and in Table 5.2:

- **Coherent twin boundary with** $[11\bar{2}]$ **crack:** Crack propagates continuously with extensive plasticity. The crack tip gets blunted by the emission of dislocations.

- **Coherent twin boundary with** $[1\bar{1}0]$ **crack:** Crack propagates continuously in a brittle-like manner with limited plasticity. The crack tip remains sharp during its propagation.

- **Σ65<100> symmetrical tilt GB:** Crack propagates in bursts in a brittle-like manner with copious dislocation emissions. The crack tip remains sharp despite the emission of dislocations.

In order to reveal the fracture mechanisms for the observed behaviors, the crack propagation processes will be analyzed in details in the following sections.

Table 5.2: Crack propagation behaviors along different GBs

Model	Crack tip	Continuous or intermittent?	Dislocation activity
Twin with $[11\bar{2}]$ crack	Blunted	Continuous	Extensive plasticity
Twin with $[1\bar{1}0]$ crack	Sharp	Continuous	Limited plasticity
$\Sigma 65 <100>$ tilt GB	Sharp	Intermittent	Extensive plasticity

5.2 Mechanism of fracture along coherent twin boundary with $[11\bar{2}]$ crack

The crack propagation process along coherent twin boundary with $[11\bar{2}]$ crack is analyzed in this section. To better characterize the crack advance, we plot the average crack length and average crack tip radius of curvature as function of strain in Figure 5-13. The methods for the calculations are described in details in Chapter 4. From Figure 5-13, it can be seen that crack advances continuously and extends by approximately 1nm at a tensile strain of 10% with an average speed of 4.0m/s. The crack speed is small compared to the Rayleigh wave speed in Ni: $c_R = 2887.6$m/s, calculated for the potential we used. The crack tip radius also increases continuously due to the emission of dislocations during the fracture. By the end of the simulation, the radius of the curvature at the tip increases by more than 2nm.

Figure 5-14 plots the spatial distribution of crack length and crack tip radius along its front at a tensile strain of 10%. It shows that both crack length and crack tip radius are non-uniformly distributed along its front. Furthermore, the crack extends most at positions between 0nm to 10nm of the its front while the crack tip gets most blunted at positions between 0nm to 15nm of its front. This implies there is a spatial correlation between crack length and its bluntness: the more the crack tip gets blunted, the further the crack extends.

The spatial coincidence of crack propagation and its bluntness suggests that there may be a causal relationship between them, i.e., that one leads to the other. Indeed, increasing crack tip radii have been observed when cracks propagate through the

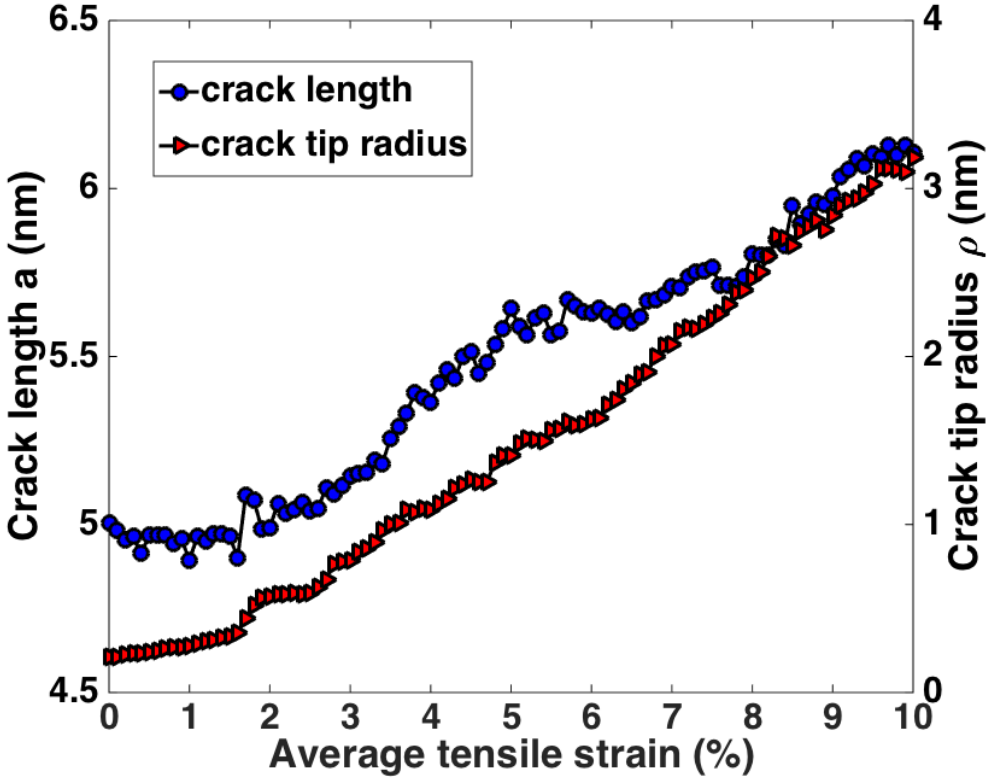

Figure 5-13: Crack length and crack tip radius during the intergranular fracture simulation along coherent twin boundary with $[11\bar{2}]$ crack.

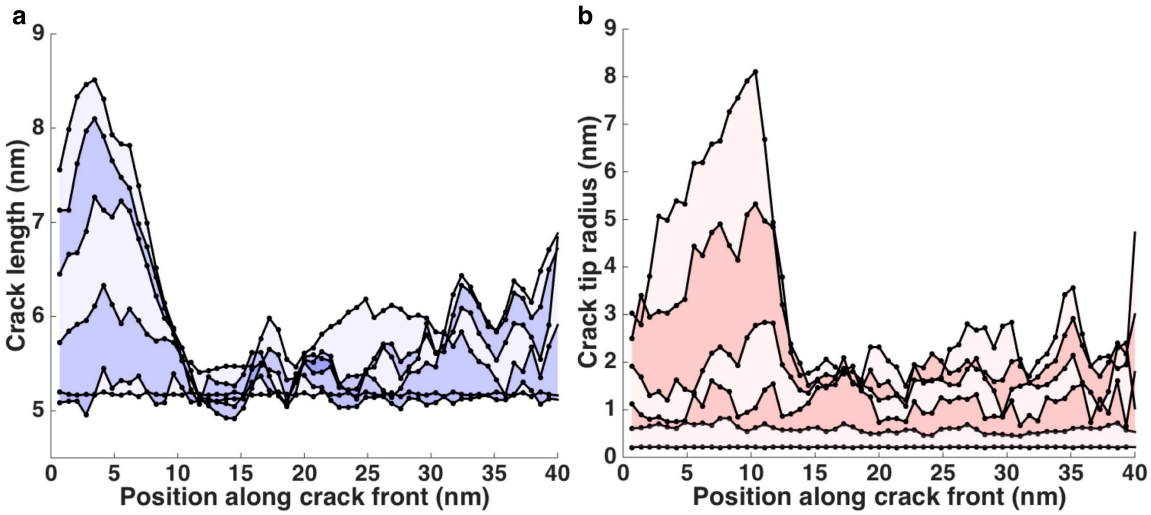

Figure 5-14: Spatial distribution of (a) crack length and (b) crack tip radius along the $[11\bar{2}]$ crack front at a tensile strain of 10%.

alternate activation of slip along two symmetrically disposed planes [102, 103], which is illustrated in Figure 5-15. In such cases, incremental increases in crack length Δa and crack tip radius $\Delta\rho$ obey

$$\frac{\Delta a}{\Delta \rho} = \cot(\phi), \tag{5.1}$$

where ϕ is the angle between the crack plane and the direction of slip.

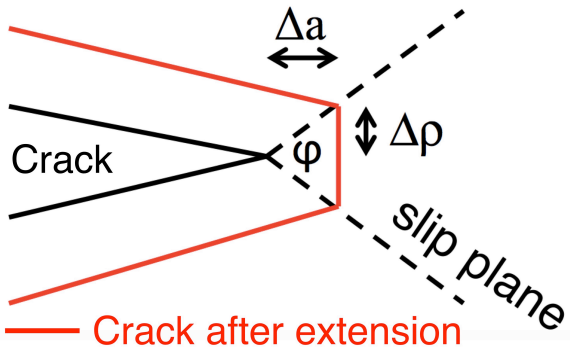

Figure 5-15: Schematic illustration of crack propagation by the alternate activation of slip along two symmetrically disposed planes.

To verify this hypothesis, the dislocations emitted from the crack tip during fracture are analyzed using DXA (see Figure 5-16). It is found that Shockley partial dislocations with $\frac{1}{6}[211]$ (leading partial) and $\frac{1}{6}[1\bar{1}2]$ (trailing partial) Burgers vectors are the primary type of dislocations emitted from the crack tip. Therefore, the angle between the crack plane and the direction of slip is computed to be $\phi = 58.5°$, predicting $\Delta a/\Delta\rho = 0.61$ for crack advance due to slip. Figure 5-17 plots the crack length vs. crack tip radius. There are good linear relationship between them and the fitting yields a slope of $\Delta a/\Delta\rho = 0.40 \pm 0.02$, which is in good agreement with the value 0.61, predicted by Equation 5.1.

Based on the analysis above, the intergranular crack propagation along coherent twin boundary with $[11\bar{2}]$ crack is induced by slipping of atoms at the crack tip due to emission of dislocations. There is few bond breaking events.

One interesting feature of this fracture is that crack extension is localized−most of the crack advance occurs at one location while the rest part of the crack almost does not propagate (see Figure 5-18). This leads to the reorientation of crack front

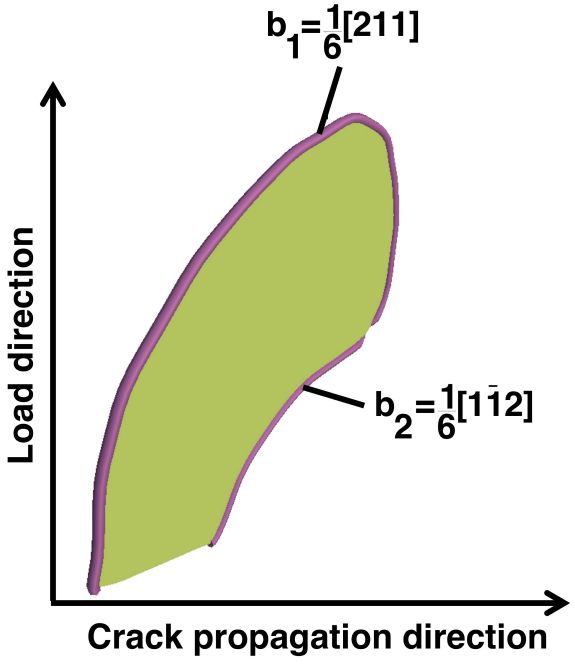

Figure 5-16: Shockley partial dislocations with $\frac{1}{6}[211]$ and $\frac{1}{6}[1\bar{1}2]$ Burgers vectors are the primary type of dislocations emitted from the $[11\bar{2}]$ crack tip.

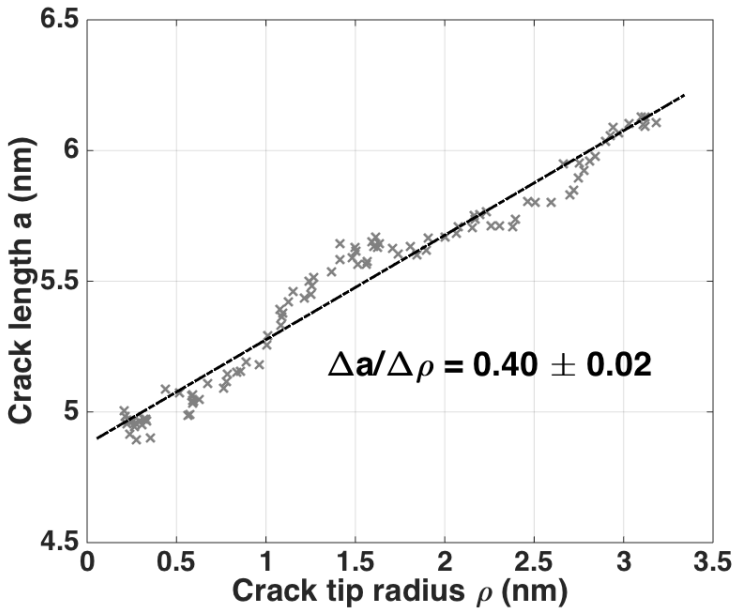

Figure 5-17: Crack length vs. crack tip radius. Linear fitting yields a slope of 0.40 ± 0.02.

from $[11\bar{2}]$ to $[1\bar{1}0]$ direction. It implies that the emission of dislocations from one location of the crack front will lead to emission of more dislocations from the same location. This is, however, contour-intuitive, because the emission of the dislocations blunts the crack tip and generally reduces the local stress intensity factors at that location.

One possible explanation for this behavior may be that, in this case, the perturbation of the straight crack front due to crack advance by slipping of atoms causes the local stress intensity factor to increase. Indeed, Rice derived theoretical formula for the stress intensity factor due to small perturbations of a straight crack front [104]. It shows that small initial deviations from straightness of the crack front can either reduce or increase the stress intensity factor depending on the size of the perturbation. If the size of the perturbation is larger than a critical length, then local stress intensity factor goes up. The critical length λ_c depends on the loading systems and crack geometry and is, however, hard to estimate for our system.

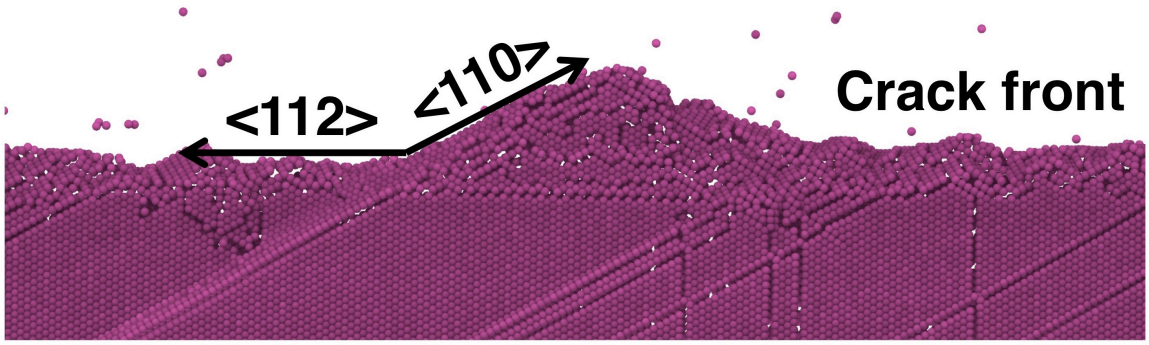

Figure 5-18: Localized crack propagation leads to reorientation of crack front from $[11\bar{2}]$ to $[1\bar{1}0]$ direction.

5.3 Mechanism of fracture along Σ65<100> symmetrical tilt GB

The crack propagation process along Σ65<100> symmetrical tilt GB is analyzed in this section. We plot the crack surface area and average crack tip radius of curvature

as functions of strain in Figure 5-19. It can be seen from Figure 5-19 that the four bursts are clearly discernible on this plot and initiate at 1.9%, 7.6%, 10.0%, and 12.6% strain. The crack does not advance uniformly along its entire front. Figure 5-20 plots the crack extension as a function of position along the front, showing maximum and minimum extensions of ∼10nm and ∼4nm, respectively, at the end of the simulation. The crack propagation velocity during each burst is 20m/s-50m/s, i.e. far lower than the Rayleigh wave speed, $c_R = 2887.6$ m/s, of the potential we used.

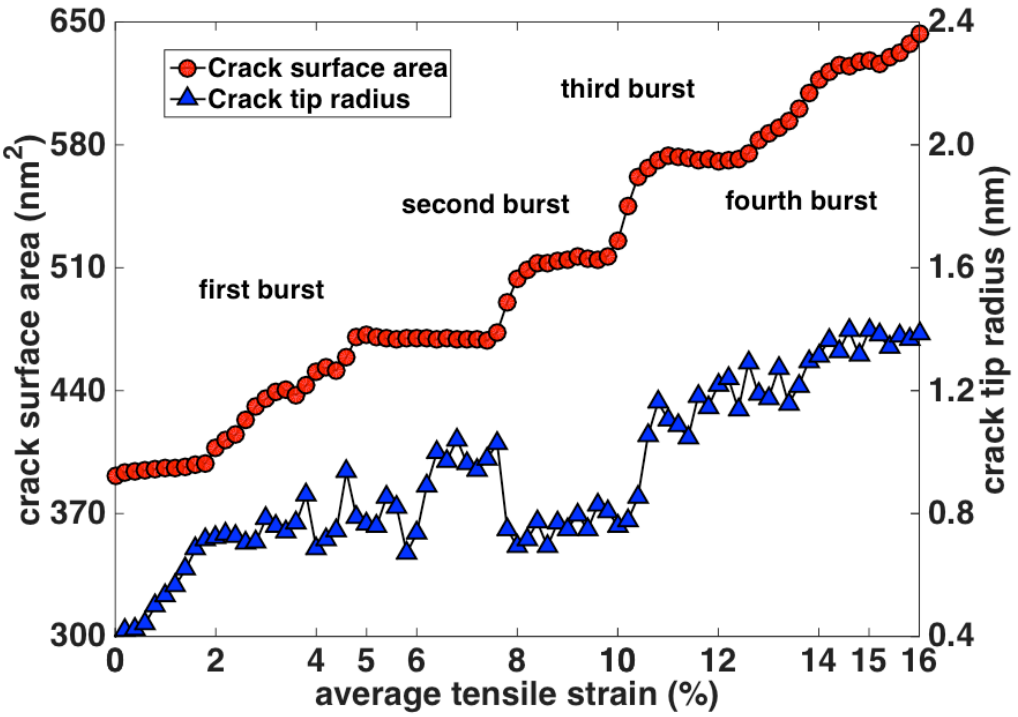

Figure 5-19: Crack surface area and crack tip radius during the intergranular fracture simulation.

The crack tip remains sharp throughout the entire simulation. Initially, its radius of curvature is $\rho \approx 0.4$nm. During each burst, the crack blunts slightly, causing ρ to increase, as shown in Figure 5-19. However, by the end of the simulation, the radius of curvature of the tip increases by only ∼0.9nm, despite the numerous dislocations emitted during each burst. The primary type of dislocations emitted from the crack tip is Shockley partials with $[12\bar{1}]$ and $[\bar{1}1\bar{2}]$ Burgers vectors. Therefore, the angle between the crack plane and the direction of slip $\phi = 40.45°$, predicting $\Delta a/\Delta\rho$=1.17

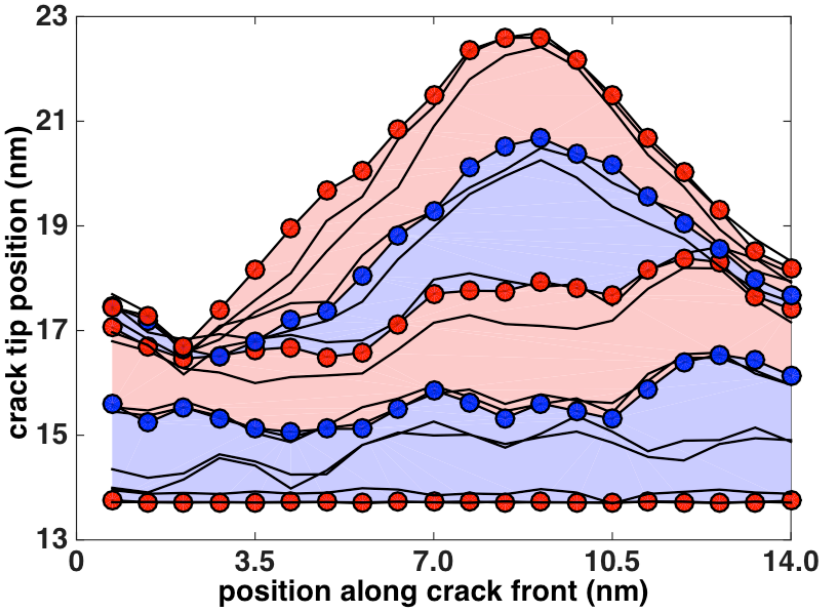

Figure 5-20: Location of the crack tip as a function position along the crack front.

based on Equation 5.1 for crack advance due to slip. However, the measured value of $\Delta a/\Delta\rho$ in our simulation is ∼9.3. Thus, the crack advance is an order of magnitude greater than would be expected due to slip alone, indicating a significant contribution of bond breaking to crack extension.

Based on the analysis above, the mechanism for crack propagation along Σ65<100> symmetrical tilt GB is different from that along coherent twin boundary with $[11\bar{2}]$ crack, where crack propagation is mainly attributed to the slipping of atoms by emission of dislocations. To understand how crack propagates along Σ65<100> symmetrical tilt GB, we will investigate bond breaking and dislocation emission as a function of position along the crack front and as a function of time during the second and third bursts.

5.3.1 Statistical analysis of crack tip processes

We exclude the first burst from this analysis because it starts with a perfectly straight, defect-free crack on an undisturbed GB: a configuration that may not be representative of a propagating crack tip. By contrast, in the remaining bursts,

the initial structures of the crack tip and GB are already highly perturbed by the preceding stages of fracture. We also exclude the fourth burst because at its onset the model is already severely distorted from its initial geometry.

Bond breaking analysis and slip vector analysis in a region of rectangular 3nm×6nm cross-section containing the crack front are performed using the methods described in Chapter 4. To ensure a temporal resolution sufficiently high to investigate bond breaking and dislocation emission in detail, we saved snapshots of the complete atomic-scale model every 0.1ps. We begin by investigating the spatial distribution of debonding and slip events along the crack front. Figure 5-21a and b show that these two processes occur non-uniformly along the crack front, consistent with the non-uniform rate of crack advance illustrated in Figure 5-20. Furthermore, slip and decohesion are correlated: the number of slip events is larger at locations where more bonds are broken. The Pearson coefficients for this relationship are 0.77 and 0.68 for the second and third bursts, respectively, indicating a high level of correlation between slip and bond breaking. The probability of the null (no-correlation) hypothesis for both bursts is less than 5%. Thus, bond breaking and slip are not locally mutually exclusive. On the contrary: they are co-located.

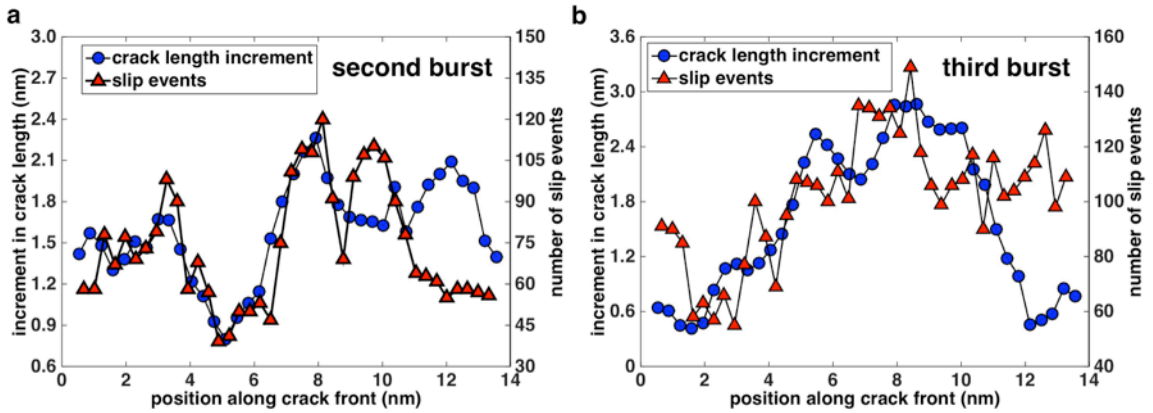

Figure 5-21: Correlation between bond breaking and dislocation emission at the crack tip during the (a) second and (b) third burst.

The spatial coincidence of slip and bond breaking suggests that there may be a causal relationship between these processes, i.e., that one leads to the other. To

examine this possibility, we study the temporal sequence of bond breaking and slip at each crack front location. To calculate t_{debond} and t_{slip}, the crack front is divided into twenty 0.7nm-wide bins. Inside each bin, the cumulative distributions F(x) of debonding and dislocation nucleation events are found. We estimate the start times, t_{debond} and t_{slip}, as the times at which the cumulative number F(x) of bond breaking or slip events exceeds 10% of the total at a given location for a given burst (see Figure 5-22).

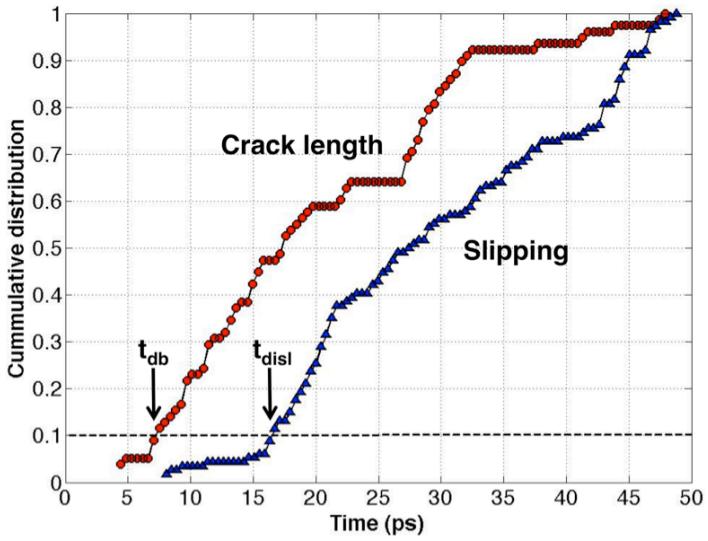

Figure 5-22: Cumulative distribution of debonding (red) and slip events (blue). The starting times for the two crack tip processes are defined as the times when their cumulative distribution reaches 10% threshold (dashed line).

Figure 5-23 plots tdebond against tslip for all locations and bursts analyzed, showing that bond breaking always precedes slip. Thus, crack advance begins as brittle fracture through bond breaking at certain locations along the crack front and is followed by emission of dislocations at the same locations.

5.3.2 Decohesion restrained by emission of dislocations

The emission of dislocations following brittle crack propagation is unexpected because, under quasi-static displacement-controlled loading, crack extension leads to

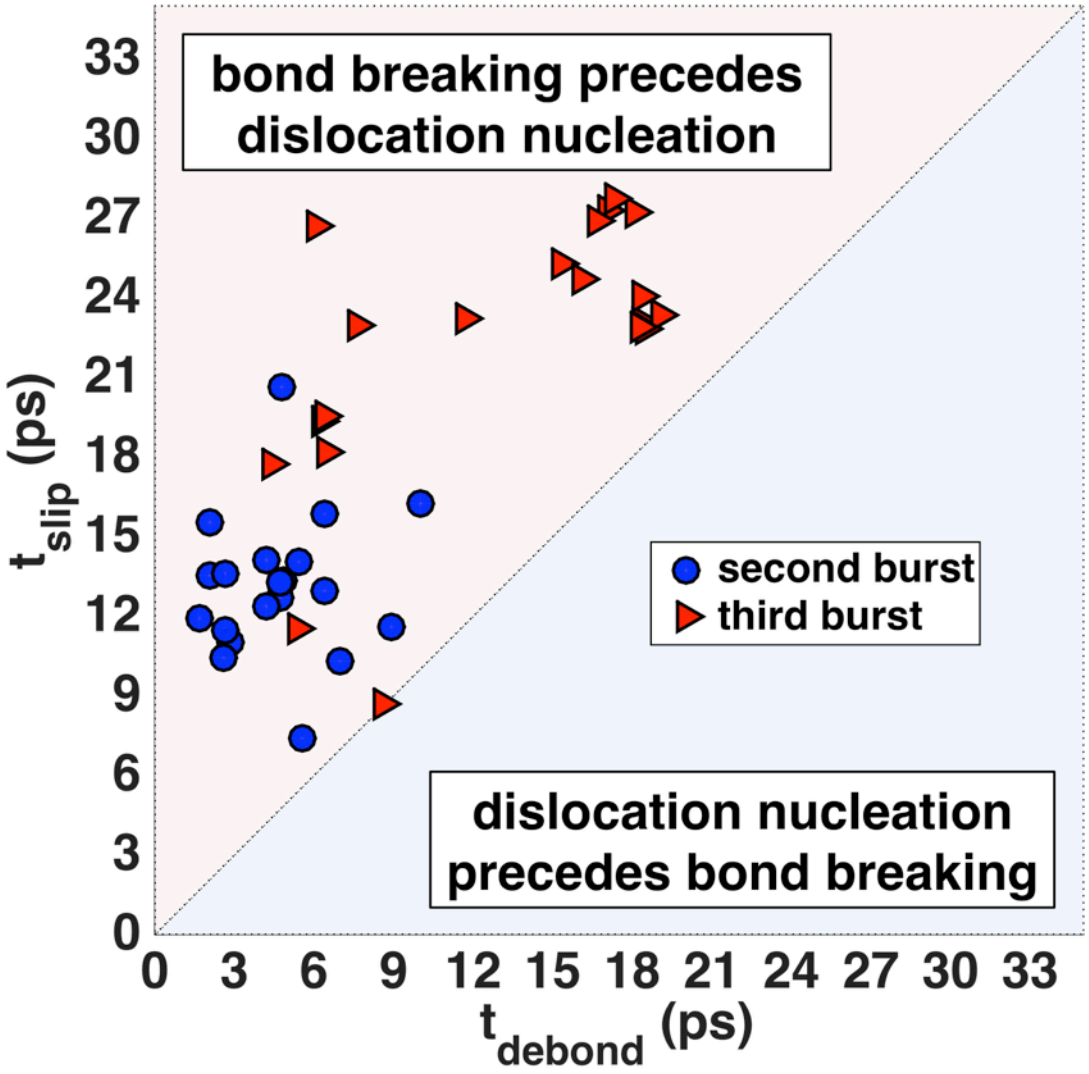

Figure 5-23: Times for onset of bond breaking (t_{debond}) and dislocation emission (t_{slip}). All the data points fall into the upper-left half-plane, indicating that bond breaking precedes dislocation emission.

a reduction in the stresses ahead of the crack, decreasing the likelihood of subsequent dislocation emission. To understand how crack advance initiates dislocation emission in our simulations, we determine the tensile stress, σ_{yy}, along the GB as a function of position ahead of the crack and plot it in Figure 5-24 for different times during the second burst. The stresses and start times, $<t_{debond}>$ and $<t_{slip}>$, in Figure 5-24 are averages taken along the crack front. Surprisingly, tensile stresses ahead of the crack increase immediately following the onset of brittle fracture and only begin to decrease upon emission of dislocations.

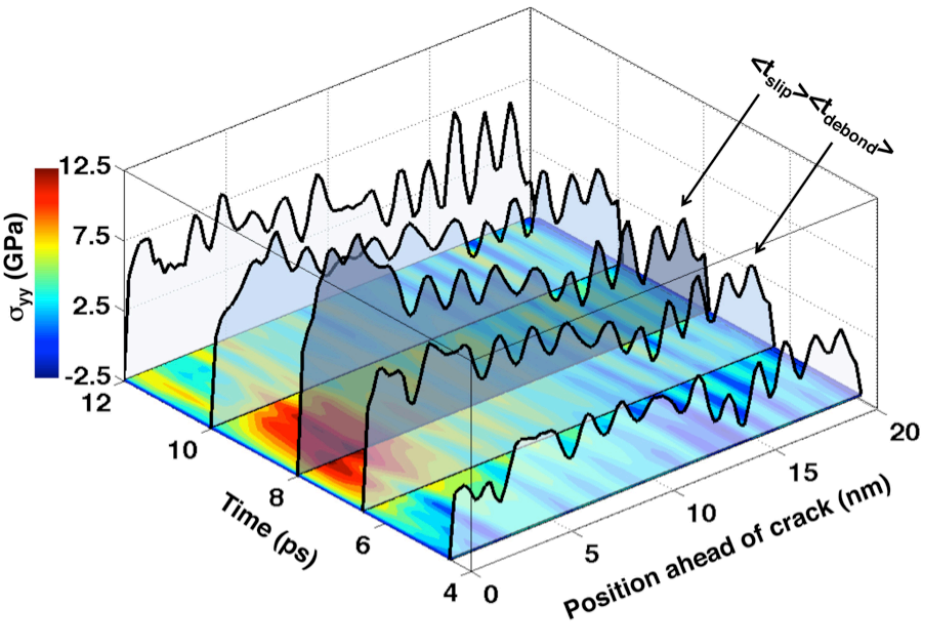

Figure 5-24: Tensile stresses ahead of the crack front during the second burst. $<t_{debond}>$ and $<t_{slip}>$ are averages of t_{debond} and t_{slip} along the crack front.

The foregoing observations lead us to propose a new mechanism of intergranular fracture in Ni that proceeds in the following stages:

- As external loads rise, the conditions for onset of brittle fracture are reached at the tip of a pre-existing sharp crack
- The crack advances by bond breaking and the stresses ahead of the crack increase

- Elevated stresses ahead of the advancing crack initiate the emission of dislocations, which, in turn, relax the crack tip stresses and arrest crack advance

To summarize these stages, we name the proposed mechanism decohesion restrained by emission of dislocations (DRED).

A key component of DRED is that tensile stresses ahead of a crack increase as the crack advances by bond breaking. We argue that this unexpected behavior is due to characteristic, transient elastic fields that accompany subsonic brittle fracture [105]. To illustrate these fields, we perform a separate simulation on an idealized 2D model, shown in Figure 5-25a. The model consists of a close-packed array of particles. The size of the model is 446×386 in reduced units. Atoms interact through a nearest-neighbor harmonic potential:

$$\phi(r) = \frac{1}{2}k(r-d)^2. \tag{5.2}$$

The equilibrium nearest neighbor distance is $d = 2^{1/6}$ and the spring constant is $k = \phi''(d) = 72/2^{1/3}$. An atomically sharp crack of length 100 is introduced by turning off the interactions between atoms above and below the crack line. The elastic wave speeds are,

$$c_d = \sqrt{\frac{2\mu}{\rho}} = 9, c_s = \sqrt{\frac{\mu}{\rho}} = 5.2 \tag{5.3}$$

with shear modulus $\mu = \sqrt{3}k/4$ and density $\rho = \frac{2}{2^{1/3}\sqrt{3}}$. Therefore, the dilatational wave takes t=42.8 to reach the boundary and t=85.8 to come back to the crack. We create an edge crack in the model, impose an initial tensile strain of 3% by displacing the upper and lower surfaces, and relax the resulting configuration using energy minimization. We then instantaneously extend the crack by 20% and simulate the resulting elastic fields using MD.

Figure 5-25b shows the distribution of tensile stress σ_{yy} immediately after crack extension. The initial, equilibrium elastic fields are perturbed by the emission of two elastic wave fronts that propagate radially away from the crack tip: a dilatational

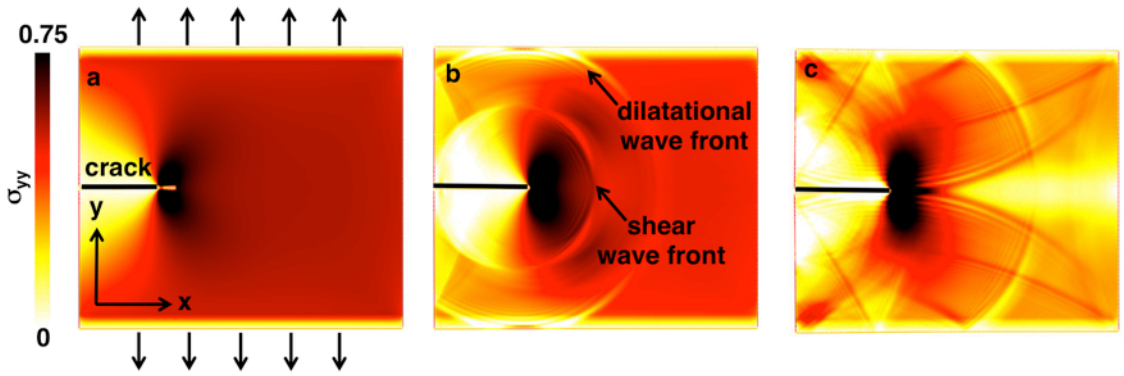

Figure 5-25: Tensile stress distributions in a 2D model (a) at the beginning of the simulation, (b) when the dilatational wave reaches the loading layer and (c) when the reflected dilatational wave reaches the crack tip. All quantities are given in reduced units.

wave and a slower shear wave. These waves are the only means by which information is carried from the crack tip to the boundaries of the model and vice versa. Thus, the time it takes for the crack tip to communicate with the boundaries—including the top and bottom surfaces, where loading is applied—is the time it takes the faster of these two waves (the dilatational one) to travel to the nearest surface and back. Prior to the return of the reflected dilatational wave, the elastic field around the crack does not depend on the shape or dimensions of the model and may therefore be considered a characteristic—albeit transient—state of a crack that has advanced subsonically by brittle fracture. In the long-time limit, scattering of elastic waves from the model boundaries, the crack, and each other—illustrated in Figure 5-25c—re-establishes mechanical equilibrium.

Remarkably, the characteristic transient elastic fields near the crack tip in Figure 5-25b closely resemble the asymptotic singular fields around an equilibrium crack [25]. In particular, the characteristic transient fields also exhibit a $R^{-1/2}$ singularity and a dependence on the polar angle θ identical to that found in equilibrium mode I loading (for all three stress components). The characteristic transient fields may therefore be described by a mode I stress intensity factor, K_{It}, where the subscript t indicates that we are referring to the characteristic transient fields.

The stress intensity factor (SIF) is estimated by fitting the asymptotic fields

around the crack tip (see Figure 5-26) [25],

$$\sigma_{ij}(r,\theta) = \frac{K}{\sqrt{2\pi r} f_{ij}(\theta)} \tag{5.4}$$

Data points near the crack surface and the tip are excluded from the fitting due to the large errors in estimating atomic-level stress there.

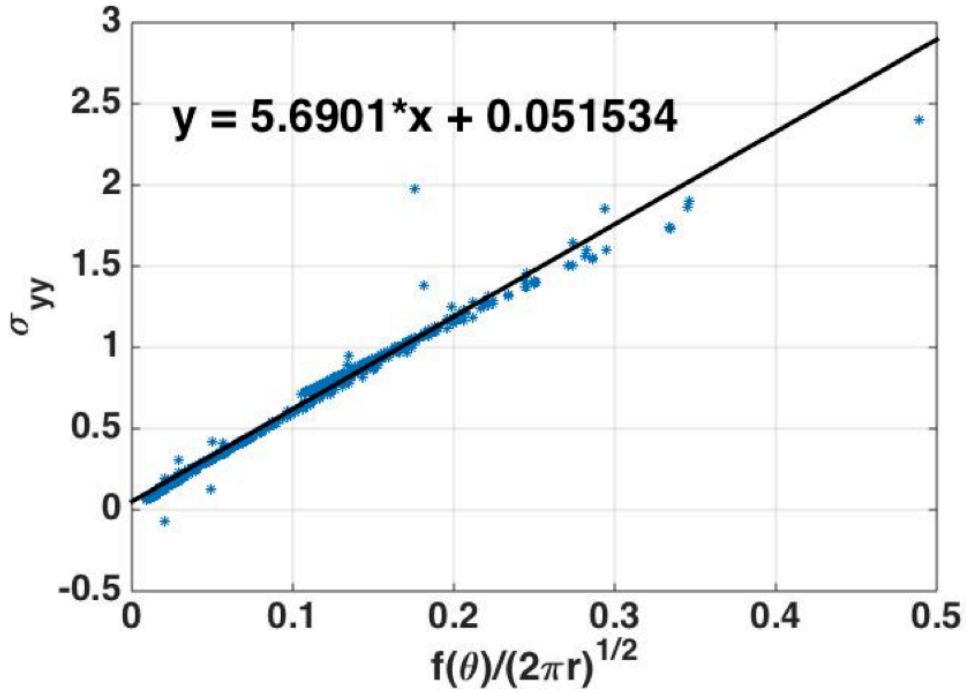

Figure 5-26: Estimation of mode I stress intensity factor by fitting σ_{yy} with $f(\theta)/\sqrt{2\pi r}$.

All the three stress components σ_{xx}, σ_{yy} and $\sigma_{xy}$are used separately for the fitting to estimate the dynamic SIF after a burst of crack advance is introduced (see Figure 5-27a). The goodness of the fitting is assessed by the R-square measure (see Figure 5-27b).

Figure 5-28 plots K_{It} as a function of time for the simulation illustrated in Figure 5-25a, where t=0 is the moment when the crack extends. The stress intensity rapidly rises to the equilibrium value−indicated by a red, horizontal line−expected for the new, extended crack length. Subsequently, K_{It} increases linearly with time, rising

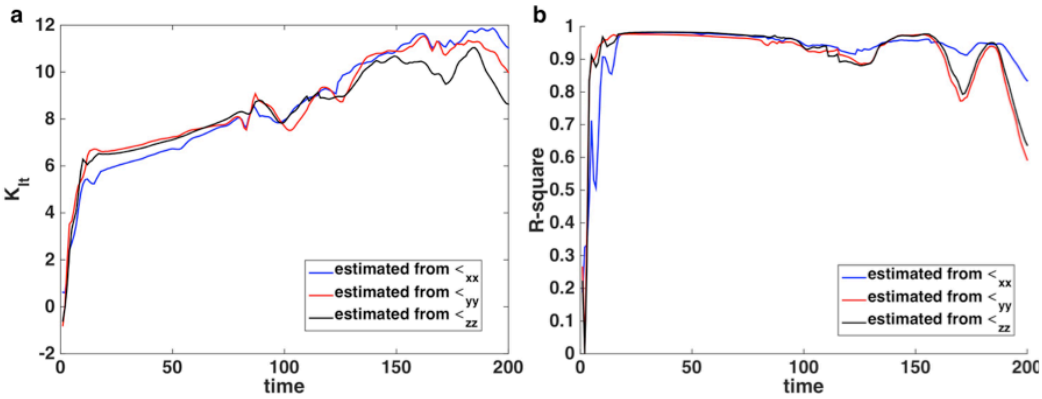

Figure 5-27: (a) The mode I dynamic stress intensity factor after a burst of crack advance is introduced is estimated using all the three stress components. (b) The goodness of the fitting is assessed by R-squre.

$\sim$25% above its equilibrium value before the dilatational wave returns to the crack tip. Afterwards, the stress distribution around the crack ceases to resemble the equilibrium asymptotic fields and K_{Ic} is ill-defined. However, as mechanical equilibrium is re-established, K_I may again be determined and approaches the expected equilibrium value, shown in Figure 5-28.

The increasing transient stress intensity factor, K_{It}, initiated by brittle fracture is responsible for elevated stresses ahead of the crack tip in the DRED mechanism. Dislocation emission initiates once K_{It} exceeds the critical stress intensity for dislocation nucleation, K_{Ic}^{disl}. Thus, all stages of DRED (see Figure 5-29a) may be described in terms of stress intensity factors. Figure 5-29b shows the change in stress intensity factor for different stages of DRED during the 2nd burst. In the first stage (indicated by S1 in Figure 5-29b), the crack is propagating in a brittle manner by sketching and breaking atomic bonds at its tip. The sudden crack propagation leads to a change in K_{It}, which is estimated using the stress fields ahead of the crack tip. The calculated ΔK_{It} is going up for 10ps (marked by circles in Figure 5-29b), resulting in a rise in the overall crack tip stress intensity factor. This then triggers subsequent dislocation nucleation, making the system entering the second stage of DRED. For this simulation, the dilatational wave speed is $c_d = 5751$m/s and it takes 15ps for the dilatational wave to reach and come back from the boundary. During the 10ps' period of the first

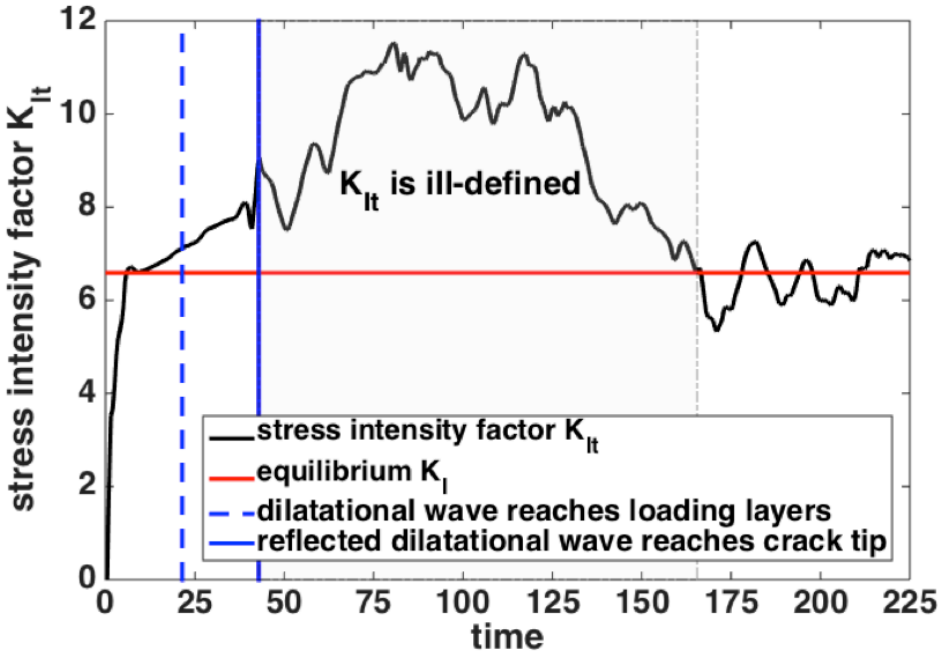

Figure 5-28: Mode I stress intensity factor in the 2D model simulation.

stage, the crack does not communicate with the boundary and therefore the rise in the stress intensity factor is not related to the size of the system.

In the second stage of DRED (indicated by S2 in Figure 5-29b), the stress fields of the nucleated dislocations can interact with the crack and can either amplify or alleviate the stress state around the crack, known as anti-shielding/shielding effect [101, 55, 106]. To estimate the change in stress intensity factor due to this effect, the dislocation line segments are first extracted from the simulation using DXA. The outcome of this extraction is the position and Burgers vector of each line segment. This information is then used to calculate ΔK_I^{disl} using the 2D dislocation anti-shielding/shielding formula,

$$\begin{aligned} \Delta K_I^{disl} &= \frac{1}{1-\nu}\left[cos\left(\frac{\theta}{2}\right) - \frac{1}{2}sin(\theta)sin\left(\frac{3\theta}{2}\right)\right]\frac{\mu b_1}{\sqrt{2\pi r}} \\ &\quad + \frac{1}{2(1-\nu)}sin(\theta)cos\left(\frac{3\theta}{2}\right)\frac{\mu b_2}{\sqrt{2\pi r}} \end{aligned} \tag{5.5}$$

The resulting ΔK_I^{disl} is shown in Figure 5-29b marked by triangles, which is negative,

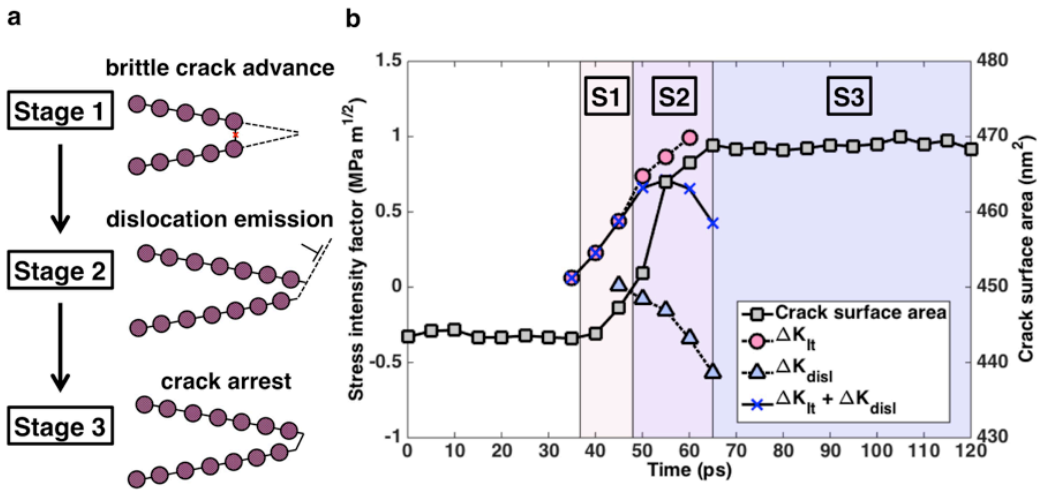

Figure 5-29: Stress intensity factors during the different stages of DRED.

indicating the dislocations are exerting a shielding effect on the crack. In the second stage, both ΔK_{It} and ΔK_I^{disl} contribute to the overall stress intensity factor at the crack tip, making it first increase and then decrease (see the curve marked by cross in Figure 5-29b). Eventually, the crack tip stress intensity factor drops below the critical value to sustain crack propagation, leading to the arrest of the crack in Stage 3 (indicated by S3 in Figure 5-29b).

In summary, crack propagation mechanism along $\Sigma 65 <100>$ symmetrical tilt GB is neither purely brittle nor the one described in Section 5.2. Rather, crack propagates in a brittle-like manner, which initiates dislocation emissions. The emission of dislocation then causes the crack to arrest.

5.4 Mechanism of fracture along coherent twin boundary with $[1\bar{1}0]$ crack

The crack propagation process along coherent twin boundary with $[1\bar{1}0]$ crack is analyzed in this section. Figure 5-30 shows the crack length and crack tip radius as a function of strain. Crack propagates continuously after the onset of fracture at a tensile strain of 1.7%. By the end of simulation, the crack extends by approximately

9.8nm with an average speed of 23m/s. The crack tip radius remains sharp throughout the entire simulation. At 10% tensile strain, the radius of curvature at the crack tip increases by only ∼0.4nm, yielding $\Delta a/\Delta\rho = 24.5$, which is much higher than the predicted ratio 0.58 for the primary slip system using Equation 5.1. The high ratio of Δa over $\Delta\rho$ indicates a significant contribution of bond breaking to crack extension, excluding the possibility of crack propagation via the mechanism described in Section 5.2.

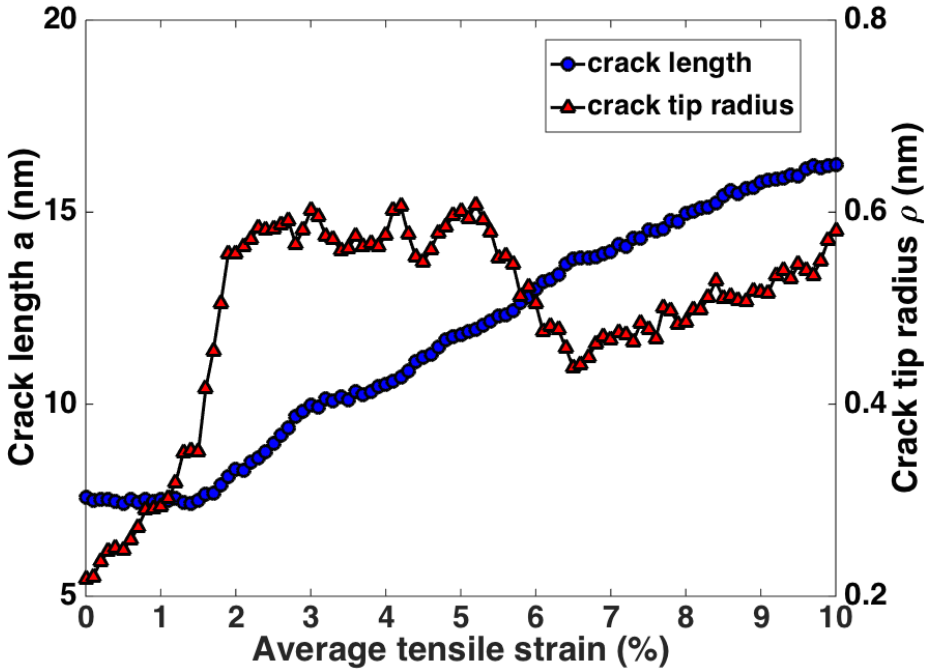

Figure 5-30: Crack length and crack tip radius during the intergranular fracture simulation along coherent twin boundary with $[1\bar{1}0]$ crack.

Similar to crack propagation along Σ65<100> tilt GB described in Section 5.3, the fracture processes involve both brittle decohesion and dislocation nucleation. To check whether there is a correlation between bond breaking and dislocation emission, similar statistical analysis shown in Section 5.3.1 is performed in a 20ps interval after the onset of fracture. Figure 5-31 shows the resulting spatial distribution of crack extension and slipping along the crack front. They are non-uniformly distributed. The Pearson coefficients for the correlation between crack extension and slipping is 0.69, which indicates a high level of correlation between the two crack tip processes.

The probability of the null (no correlation) hypothesis is less than 5%. The causal relationship between bond breaking and dislocation emission here is similar to the one described in Section 5.3−crack extension increases the transient stress fields near the crack tip, which initiates the nucleation of dislocations. Therefore, more slipping events are observed at locations where the crack advances more.

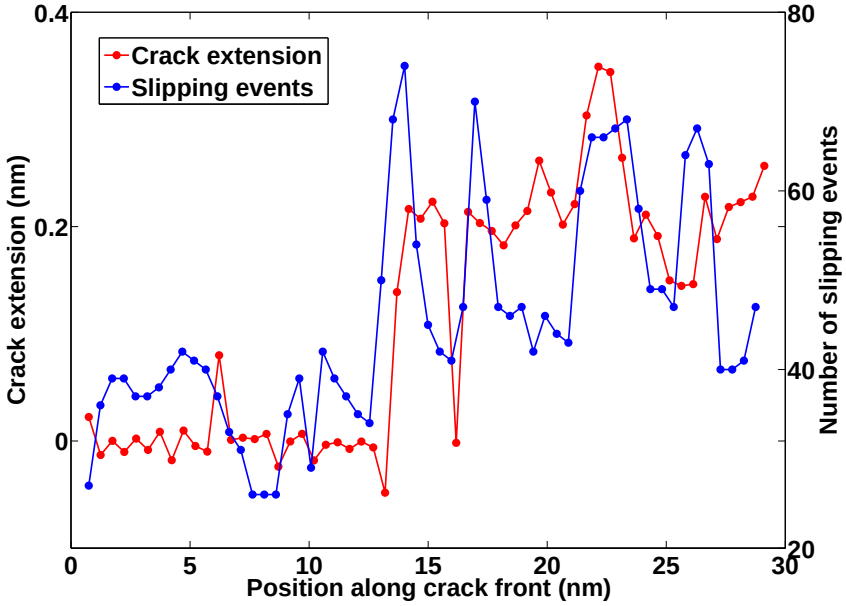

Figure 5-31: Spatial distribution of crack length and number of slipping events along the crack front in a 20ps interval right after the onset of fracture.

However, there is one significant difference between the fracture described in this section and in Section 5.3. For fracture described here, crack propagates continuously with very limited plasticity while for fracture described in Section 5.3, intermittent crack propagation with extensive plasticity is observed. To understand why the dislocation nucleated from the $[1\bar{1}0]$ crack does not arrest the crack, the post-yielding plastic deformation process is analyzed.

Dislocation configurations are extracted from the simulation in the initial and later stages of the fracture. Figure 5-32 shows that the stacking fault tetrahedron is directly nucleated from the crack tip at 1.7% tensile strain. The edges of the tetrahedron are stair-rod dislocations with 1/6<110> Burgers vector. The Burgers

vector of the stair-rod dislocation is perpendicular to the dislocation line and does not lie in either of the slip planes. Therefore, it cannot glide and is immobile. Unlike the plastic flow carried by the continuous movement, multiplication and entanglement of the free mobile dislocations emitted from the [100] crack along $\Sigma 65\langle 100\rangle$ tilt GB, the nucleated stacking fault tetrahedron from the $[1\bar{1}0]$ crack is immobile and thus is unable to relieve the local crack tip stress through plastic flow. This local hardening mechanism in the vicinity of the crack tip causes the continuous brittle crack propagation without arrest.

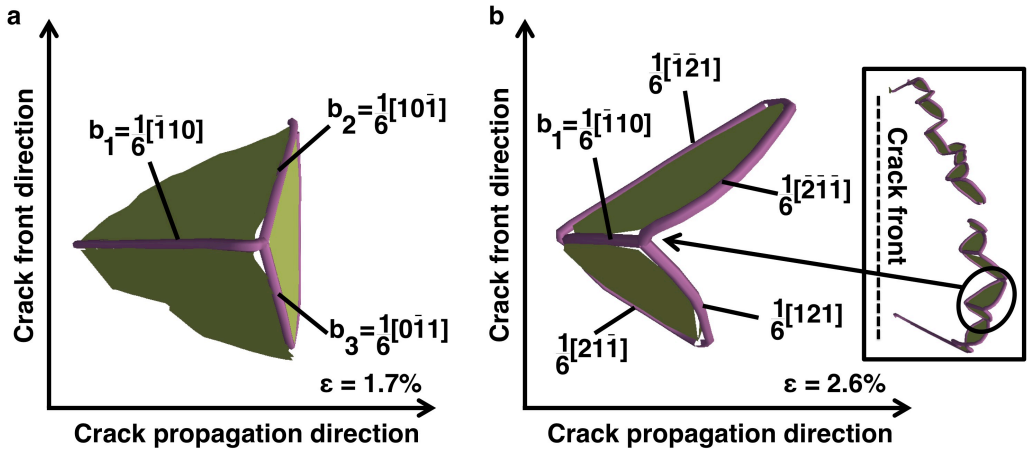

Figure 5-32: Dislocation configurations extracted from simulations at 1.7% and 2.6% tensile strain using DXA.

As the loading is increased, the stacking fault tetrahedron becomes unstable at a tensile strain of 2.6%. Shockley partials are dissociated from the stacking fault tetrahedron with $1/6[\bar{2}\bar{1}\bar{1}]$ and $1/6[\bar{1}\bar{2}1]$ Burgers vectors on the $(\bar{1}11)$ plane as well as $1/6[121]$ and $1/6[21\bar{1}]$ Burgers vectors on the $(1\bar{1}1)$ plane (see Figure 5-32b). Unlike the stacking fault tetrahedron, Shockley partial dislocations are mobile and can easily glide. The motion of dislocations contributes to the plastic flow. However, this does not leads to crack arrest because deformation twins are nucleated from the GBs ahead of the crack (see inset of Figure 5-5a) right after the onset of dislocation propagation at 3.0% tensile strain,. The deformation twins act as obstacles to dislocation motion

and cause local hardening again (see Figure 5-33a). The local hardening mechanism due to deformation twining enables continuous crack advance without arrest in the later stages in the simulation.

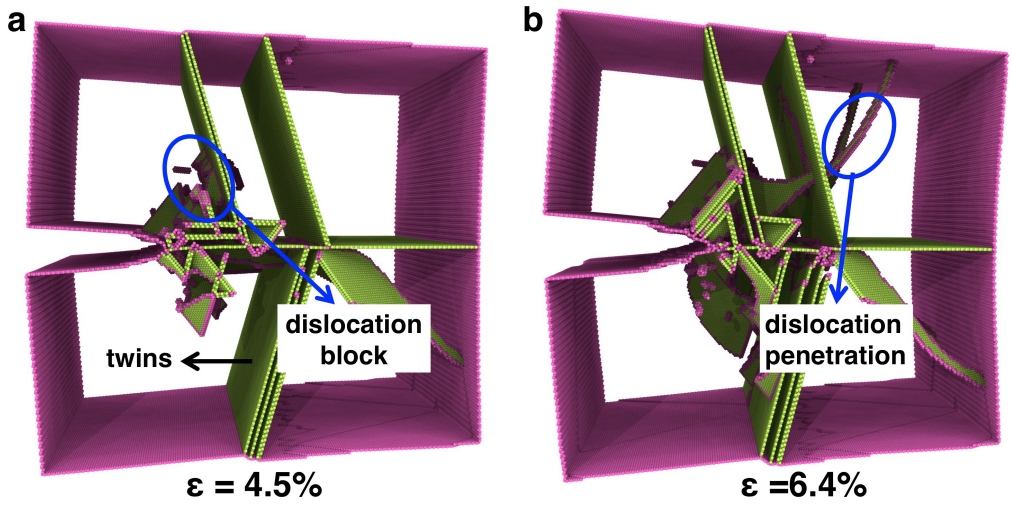

Figure 5-33: (a) The deformation twin blocks the motion of dislocations. (b) Dislocations penetrate the deformation twin.

Based on the analysis above, the $[1\bar{1}0]$ crack propagates along coherent twin boundaries by brittle fracture, which initiates dislocations nucleation from the crack tip. The dislocation process does not interfere with the brittle crack propagation because their mobilities are limited due to the local hardening mechanism caused by stair-rod dislocations and deformation twins.

5.5 Critical energy release rates

The analysis in previous sections shows three distinct crack propagation mechanisms:

- **Coherent twin boundary with** $[11\bar{2}]$ **crack:** Crack propagates by slipping of atoms at its tip due to emission of dislocations.

- **Coherent twin boundary with** $[1\bar{1}0]$ **crack:** Crack propagates by DRED.

- **Σ65<100> symmetrical tilt GB:** Crack propagate continuously in a brittle-like manner without arrest due to local hardening mechanism.

In this section, we want to relate the different crack propagation mechanisms with fracture toughness. The critical energy release rates for fracture along coherent twin boundaries as well as Σ65<100> symmetrical tilt GB are calculated using the method described in Chapter 4.

5.5.1 G_c calculation for fracture along coherent twin boundaries

Figure 5-34 illustrates G_c calculation for fracture along coherent twin boundaries with different crack orientations. Crack directional anisotropy in G_c is observed: for the crack oriented in the $[1\bar{1}0]$ direction, the average $G_c = 24 \pm 1 J/m^2$ while for the crack oriented in the $[11\bar{2}]$ direction, the average $G_c = 64 \pm 2 J/m^2$, which is 2.7 times more than the former. The difference is due to different crack propagation mechanisms described in Section 5.2 and Section 5.4.

One interesting feature of the G_c curve for the $[1\bar{1}0]$ crack is that there are three turning points (see Figure 5-34) that define several intervals with distinct G_c values. Before turning point 1, the stacking fault tetrahedron nucleated from the crack tip is stable and immobilized, which causes local hardening. Therefore, in this period, crack propagates in a brittle-like manner with limited plasticity, leading a small value of $G_c = 9.7 \pm 0.8 J/m^2$. This G_c is only slightly larger than the surface separation energies $2\gamma_{111} = 3.86 J/m^2$ (see Table 3.1). At turning point 1, the stacking fault tetrahedron becomes unstable and dissociated into Shockley partials. The motion of the partials contributes to the plastic flow, causing an rise in G_c (see Figure 5-34).

At turning point 2, deformation twins are nucleated from the GBs ahead of the crack, leading to local hardening again by impeding the motion of dislocations. Using the method described in Chapter 4, the plastic work density ρ_{pw} during crack propagation is estimated from atomistic simulations (see Figure 5-35). It can be seen that for the $[11\bar{2}]$ crack, the plasticity spread over almost the whole region of the bicrystal

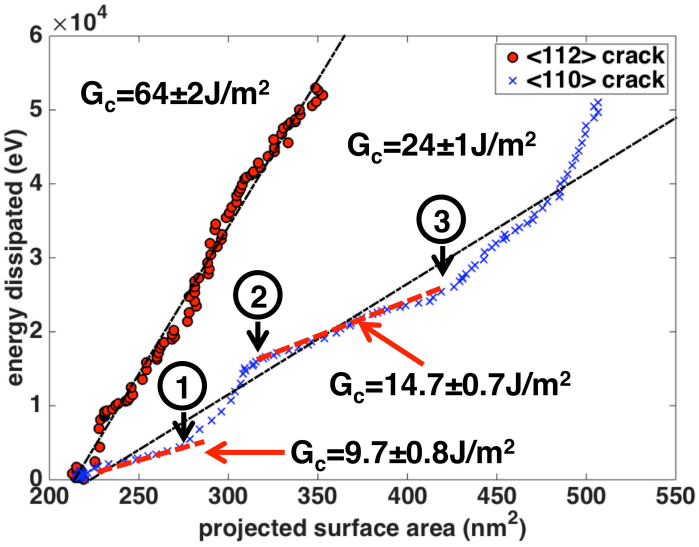

Figure 5-34: G_c for intergranular fracture along coherent twin boundaries. For the coherent twin boundary with a $[1\bar{1}0]$ crack, the stacking fault tetrehedron become unstable at 1, deformation twins are nucleated at 2, and slip across deformation twins occurs at 3.

(see Figure 5-35a) while for the $[1\bar{1}0]$ crack, the zone of plasticity (marked by ellipse in Figure 5-35b) is significantly reduced. This hardening due to deformation twining decreases G_c again to $14.7 \pm 0.7 J/m^2$. At turning point 3, dislocation slip across the twins takes place. Therefore, a rise in G_c is observed due to the increased plastic flow.

5.5.2 G_c calculation for fracture along Σ65<100> symmetrical tilt GB

Figure 5-36 illustrates G_c calculation for fracture along Σ65<100> symmetrical tilt GB, where crack propagates by DRED mechanism. The average G_c during the entire fracture simulation is $141 \pm 4 J/m^2$, which is two orders of magnitudes larger than $2\gamma_{100} = 4.12 J/m^2$ (see Table 3.1) for pure brittle fracture on <100> plane. The high G_c is attributed to the emission of dislocations triggered by brittle crack advance. It can be seen from Figure 5-36 that four bursts of brittle crack propagation are clear discernible. During each burst, the crack extends for a long distance but with small

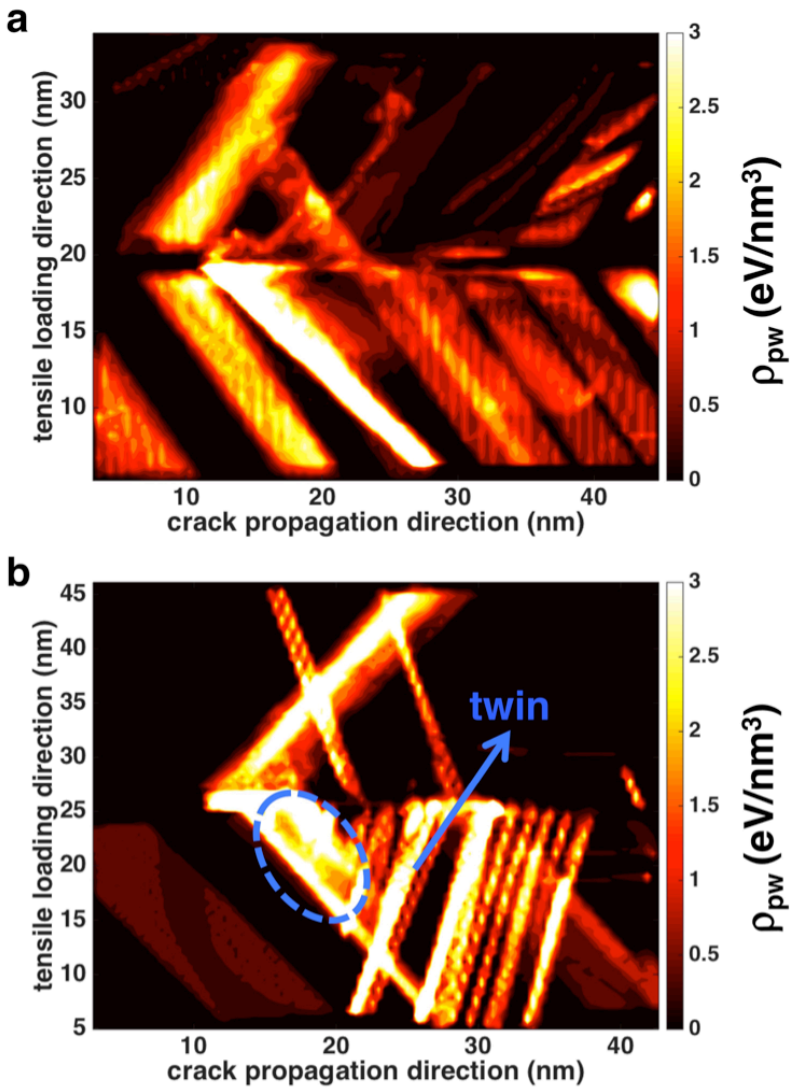

Figure 5-35: Plastic work distribution for coherent twin boundaries with cracks oriented in the (a) $[11\bar{2}]$ and (b) $[1\bar{1}0]$ directions. Plasticity spreads over almost the whole space for the $[11\bar{2}]$ crack while plasticity is limited to a small region (marked by ellipse) due to the deformation twining for the $[1\bar{1}0]$ crack.

amount of dissipated energies. The G_c values for second and third bursts are only $28 \pm 13 J/m^2$ and $18 \pm 5 J/m^2$, which is much smaller than the avearge G_c, indicating nearly brittle fracture is taking place during the burst. Between each two bursts, the G_c curve becomes steep. This is because the brittle decohesion is restrained by the emission of dislocations, leading to the arrest of the crack.

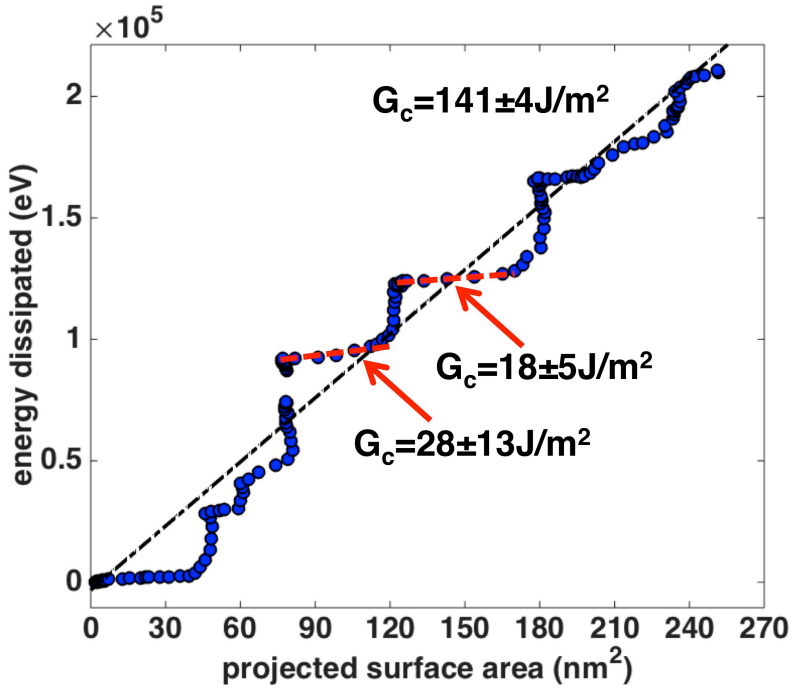

Figure 5-36: G_c for intergranular fracture along Σ65<100> symmetrical tilt GB.

The values of G_c for fracture along coherent twin boundaries and Σ65<100> symmetrical tilt GB are not directly comparable because the model sizes are different. In order to know how the G_c for crack propagation with DRED mechanism compares with others, we investigate the size effect on G_c for DRED mechanism. We construct five fracture simulation models containing the same Σ65<100> symmetrical tilt GB but with different sizes. The model (see Figure 5-8) has the same length in x direction, L_x, and different lengths in the y and z directions, L_y=L_z={23nm, 34nm, 45nm, 57nm, and 85nm}.

Figure 5-37 plots G_c for intergranular fracture in model sizes ranging from L_y=23nm to 85nm, showing that G_c increases with the model size. This effect is to be expected

because plastic work generally scales with the size of the region where dislocations are active: a larger system size gives rise to a larger plastic zone around the crack [107, 108]. By examining the slope of G_c vs. L_y on a log-log plot (see Figure 5-37), we find that $G_c \sim L_y^{1.20\pm0.48}$, indicating a nearly linear relationship between the critical energy release rate and the model size. Since the contribution of surface energy to G_c is negligible, this finding suggests that plastic work scales linearly with model size.

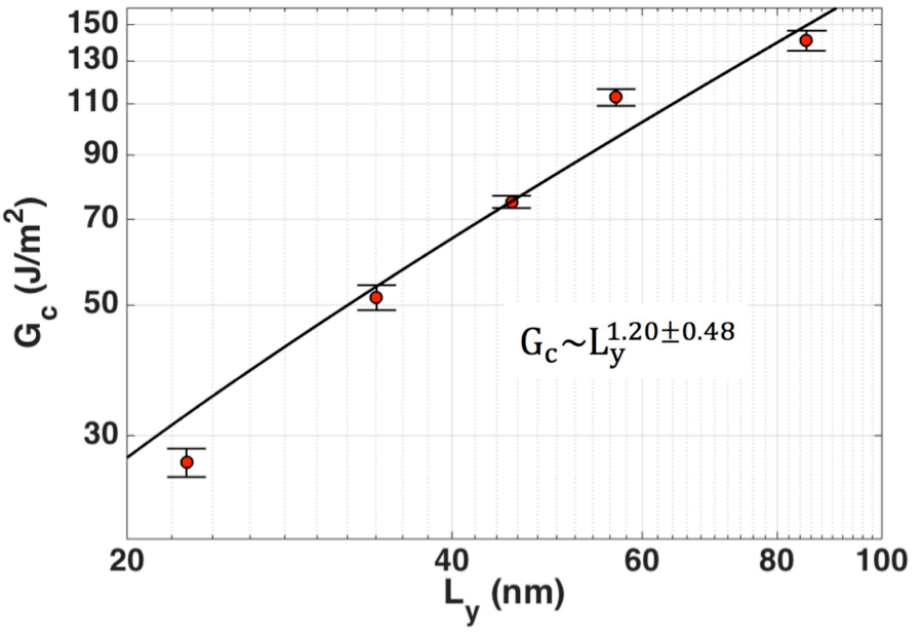

Figure 5-37: The dependence of G_c on model size, L_y, for intergranular fracture simulations.

To understand the linear dependence of G_c and plastic work on model size, the estimated plastic work densities for intergranular fracture with model sizes L_y=23nm, 34nm, and 45nm are visualized in Fig. Figure 5-38a-c. Bright regions correspond to intense dislocation activity and hence high plastic work density. The initial crack length at zero stress is marked by white lines in Figure 5-38. A striking feature of these plastic work density distributions is that most of the plastic work is localized in distinct slip bands that originate at the crack tip and end at a free surface. The size of this region increases linearly with model size, explaining the linear dependence of G_c on L_y.

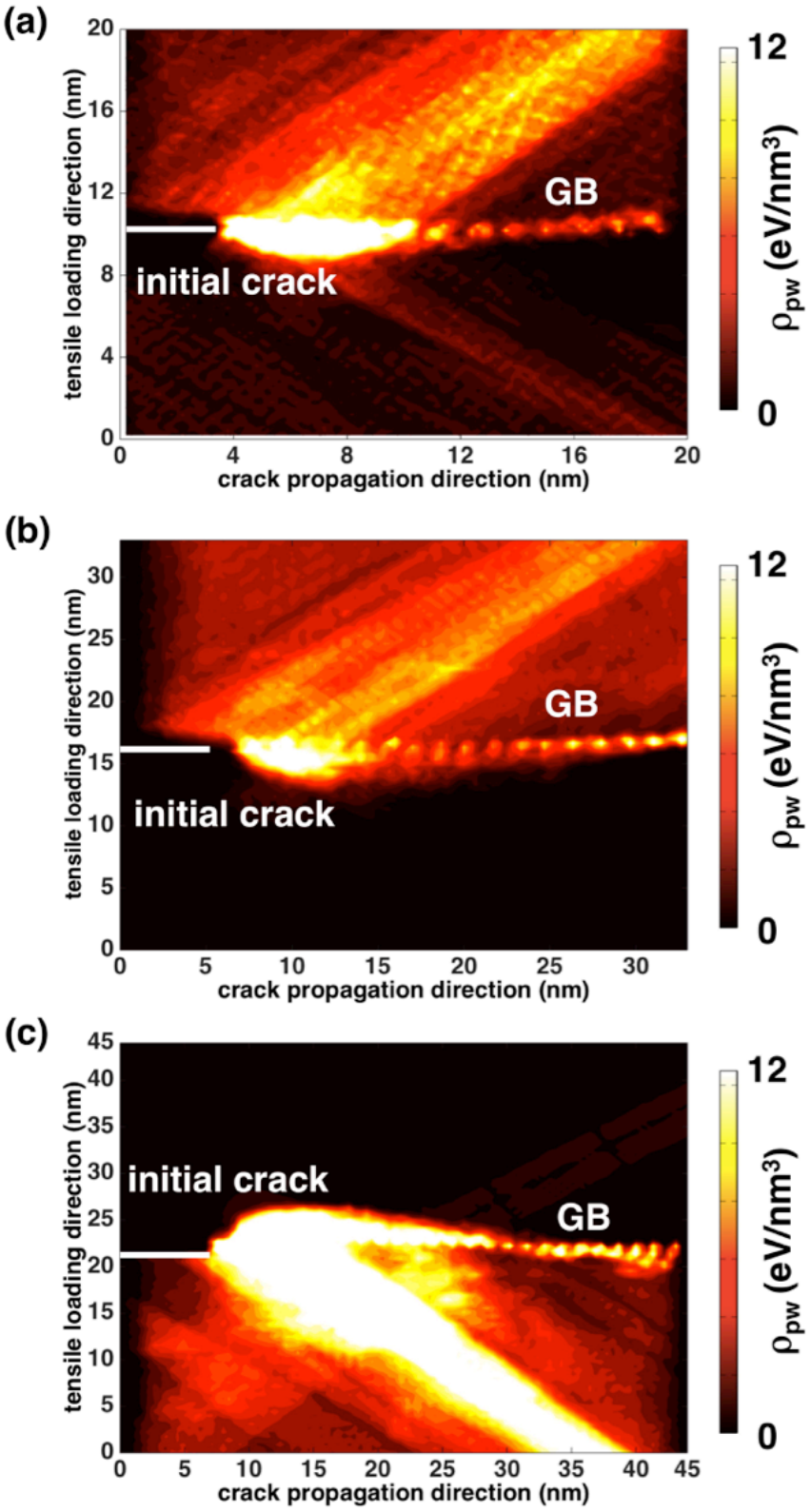

Figure 5-38: Plastic work density distribution for intergranular fracture with (a) L_y=23nm, (b) L_y=34nm and (c) L_y=45nm.

For all model sizes, the region ahead of the crack tip in Figure 5-38 is brightest because dislocations are nucleated there. We estimate the total plastic work ahead of the crack tip, W_p^{tip}, by integrating the plastic work density over a rectangular region ahead of the crack tip with width = 5nm and length = (final crack tip position) (initial crack tip position) = 4.8nm, 6.5nm, and 7.6nm for L_y = 23nm, 34nm, and 45nm. We obtain W_p^{tip}=729eV, 461eV, and 592eV with 1nm of crack extension for L_y = 23nm, 34nm and 45nm, respectively. It appears that W_p^{tip} does not scale with L_y, suggesting that the number of dislocations nucleated from the crack tip per unit crack advance does not depend on model size.

Having understood the size dependence of G_c, the value of G_c for crack propagation with DRED mechanism is extrapolated to the one with the same size as the fracture simulation along coherent twin boundaries. The resulting G_c is $\sim 46 J/m^2$, which is slightly smaller than $G_c = 64 \pm 2 J/m^2$ for crack propagation by 'ductile' fracture in Section 5.2 and larger than $G_c = 24 \pm 1 J/m^2$ for crack propagation by continuous brittle fracture in Section 5.4.

Chapter 6

Crack healing phenomenon

This chapter describes a serendipitous finding during the investigation of intergranular fracture−healing of nanocracks by microstructure evolution. We first present the crack healing phenomenon in 2D models. This mechanism relies on the generation of crystal defects known as disclinations by migrating grain boundaries. After that, we will present the healing of nanocracks in 3D microstructures of metals, followed by the discussion of its mechanism.

6.1 Atomistic simulations of crack healing

6.1.1 A serendipitous finding

In the course of studying intergranular fractures in Ni described in Chapter 5, we constructed a simulation model where a $\Sigma227(110)$ symmetrical tilt GB is perpendicular to a crack (see Figure 6-1). Under uniaxial tension, the crack faces gradually open and emit dislocations from its tip (see Figure 6-1a). Further loading leads to the dissociation of the $\Sigma227(110)$ symmetrical tilt GB into three new tilt GBs (marked by the dashed line in Figure 6-1b). The dissociated GB migrates towards the crack, causing the crack faces to close (see Figure 6-1c). As the dissociated GB continues to migrate, the crack faces finally touch each other and gets completely healed (see Figure 6-1d).

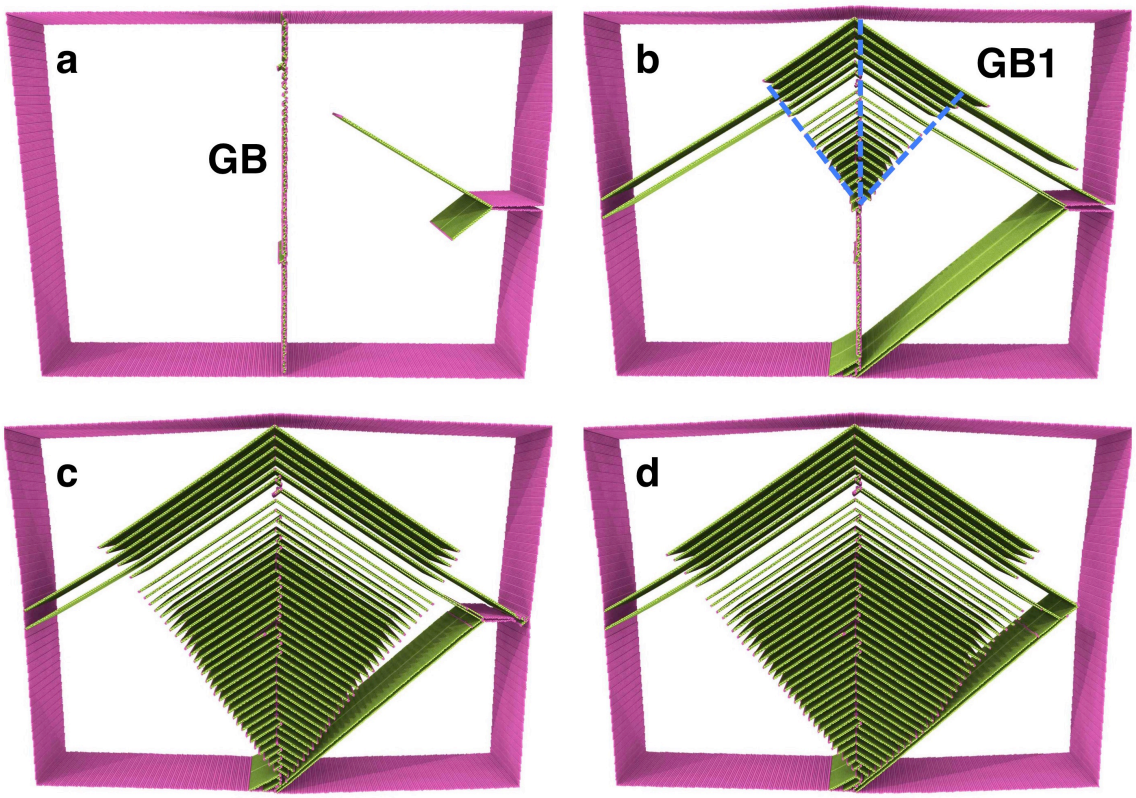

Figure 6-1: A serendipitous finding of crack healing phenomenon. (a) Under uniaxial tension, dislocations are emitted from the crack tip. (b) Further loading leads to the dissociation of he GB. (c) As the dissociated GB approaches the crack, the crack faces are closed. (d) Crack gets fully healed.

The phenomenon discovered in this simulation is very interesting−the migration of the GB leads to completely healing of the crack under tension. The key process here is stress-driven GB migration (SDGBM), where a shear stress applied parallel to a grain boundary leads to diffusionless migration of the boundary in the direction perpendicular to its plane.

6.1.2 Model construction and simulation setup

To further investigate the crack healing phenomenon and understand how SDGBM influences fracture, we use MD to simulate loading of a model microstructure in Ni: a bicrystal, shown in Figure 6-2, with a pre-existing nanocrack. The system has dimensions of $4.3nm \times 105.3nm \times 103.4nm$ with periodic boundary conditions in the x-direction and free surfaces in the y- and z-directions. To create a nanocrack, we remove atoms in a $4.3nm \times 10nm \times 1nm$ layer. The crystallographic orientation of Grain 1 is x = [$\bar{1}$ 2 $\bar{1}$], y = [$1\bar{7}$ 2 21], z = [22 19 16], and the orientation of Grain 2 is x = [$\bar{1}$ 2 $\bar{1}$], y = [$2\bar{1}$ $\bar{2}$ 17], z = [16 19 22]. In this way, two $\Sigma 367(10\bar{1})$ symmetrical tilt GBs are formed with tilt angle 14.69°.

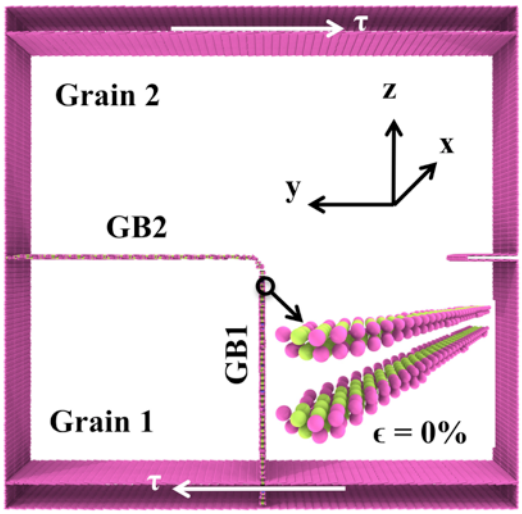

Figure 6-2: Simulation setup for Ni bicrystal model with a crack. The inset shows misfit dislocations in GB1.

The nanocrack is stable when no external stress is applied. The model is loaded in shear by applying tractions along the surfaces normal to the z-direction using the method described in Chapter 3. Due to the symmetry of the stress tensor, both GB1 and GB2, shown in Figure 6-2, are under shear stress. The orientations of Grain 1 and Grain 2 are chosen such that GB1 is a symmetric tilt GB. GB1 consists of an array of parallel edge dislocations (see inset of Figure 6-2) [14] and migrates easily due to their collective motion under an applied load. Reversing the loading direction reverses the migration direction of GB1. GB2 does not undergo shear-coupled migration and its shear resistance is sufficiently high so that it does not shear during the simulation.

6.1.3 SDGBM leads to healing or opening of cracks

We found that the migration of GB1 causes the nanocrack to open or close, depending on the direction of migration. This is surprising since the system is loaded under pure shear: there is never any net tensile or compressive external load applied to it. When GB1 moves away from the crack, the crack surfaces initially undergo a reversible crack opening displacement, as if the system were experiencing net tensile. At an average engineering shear strain of 3.5%, Shockley partial dislocations nucleate at the crack tip and glide into Grain 2, as illustrated in Figure 6-3. Additional dislocations are emitted as GB1 continues to migrate and the crack extends into Grain 2.

However, when GB1 moves toward the crack, the crack surfaces progressively close as illustrated in Figure 6-4a, even though no net compressive stress is applied. As GB1 continues to migrate, the crack faces eventually come into contact and rapidly bond along the entire length of the crack. The nanocrack is thereby fully healed, leaving behind several edge dislocations with Burgers vectors pointing in the surface normal direction of the original crack (see Figure 6-4b). Their presence in the vicinity of the healed crack is topologically necessary because the crack itself was formed by the removal of a $\sim$1nm-thick layer of atoms.

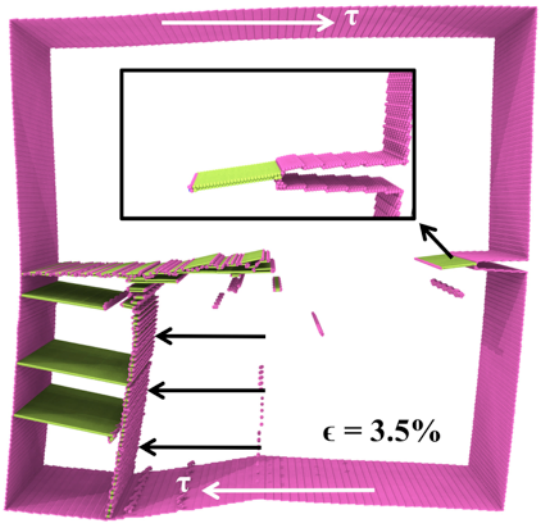

Figure 6-3: Simulation result of Ni bicrystal containing a migrating GB and a crack. The crack opens when the GB moves away from it. All perfect crystal atoms have been suppressed for clarity.

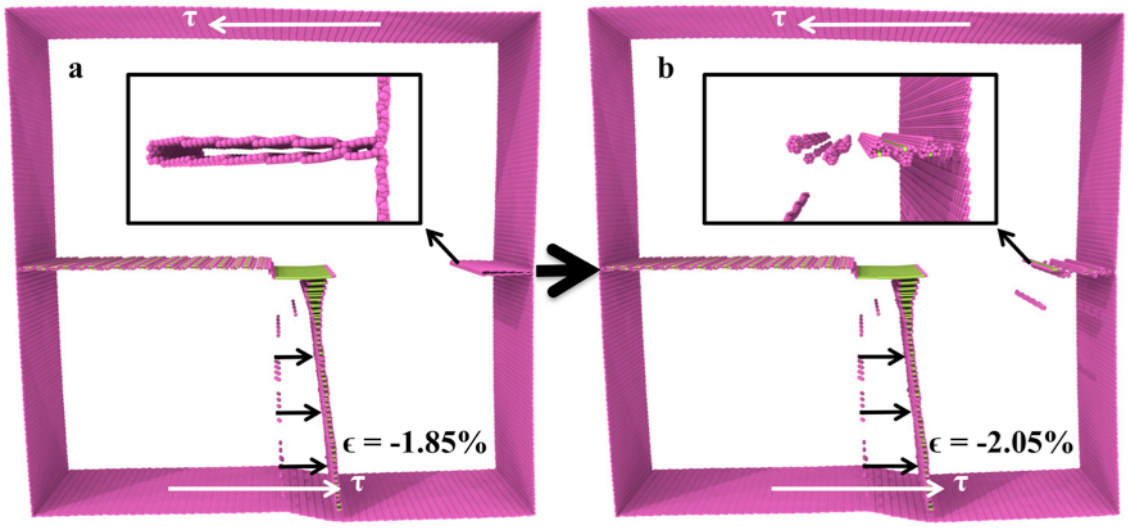

Figure 6-4: Simulation result of Ni bicrystal containing a migrating GB and a crack. The crack closes (a) and eventually heals completely (b) when the GB moves towards it. All perfect crystal atoms have been suppressed for clarity.

6.2 Crack healing mechanism

6.2.1 Generation of disclinations due to SDGBM

Crack opening and closing in the presence of SDGBM may be interpreted using the mechanics of crystal defects known as disclinations [109]. Figure 6-5 illustrates how positive and negative wedge disclinations are created. For a positive one (see Figure 6-5a), a wedge of material of angle ω is removed. The surfaces thereby created are then forced together and welded shut. For a negative wedge disclination (see Figure 6-5b), a cut is made and the surfaces thereby created are forced open to an angle ω. A wedge of material is welded in to close the gap.

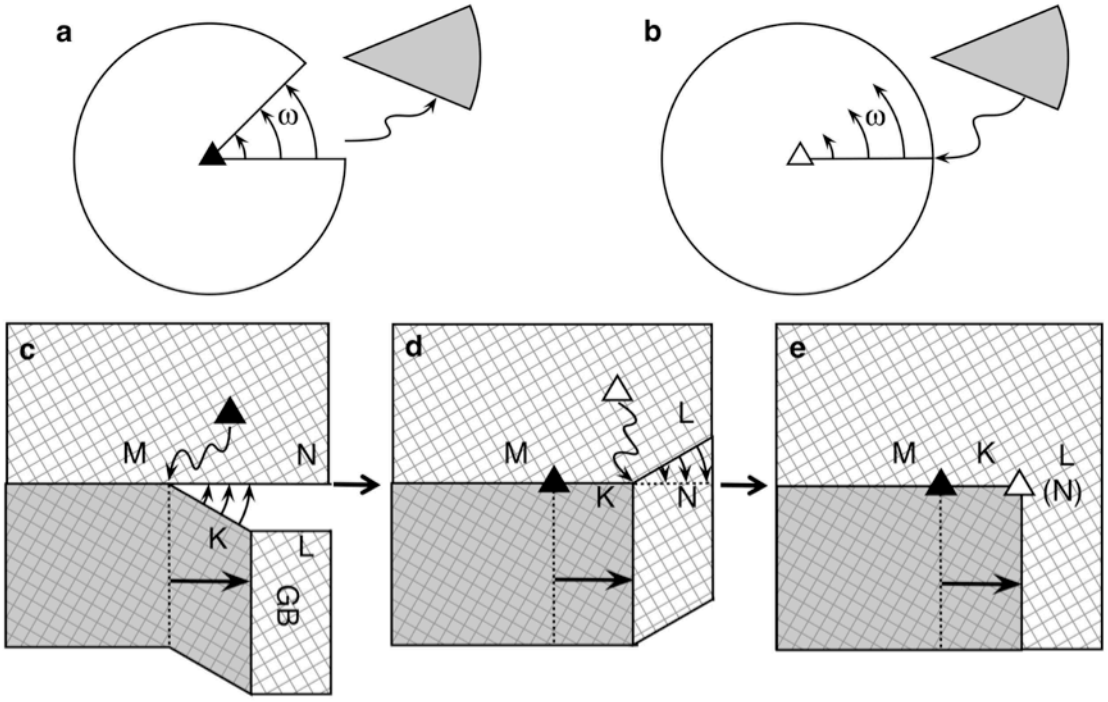

Figure 6-5: (a) Positive (filled triangle) and (b) negative (open triangle) wedge disclinations. (c) If surfaces MN and MKL are not connected, then GB migration produces the shear offset shown. (d) A positive wedge disclination is added at M to close the gap $\angle$NMK. (e) A negative wedge disclination is added at K to prevent overlap in $\triangle$LKN.

Figure 6-5 illustrate how wedge disclination dipoles may be used to describe the effect of GB migration on internal stress fields [110, 111]. If surfaces MN and MKL

are not connected, then GB1 migration produces the shear offset shown in Figure 6-5c. To reconnect surfaces MN and MKL, a positive wedge disclination is added at point M in Figure 6-5d to close the gap ∠NMK and a negative wedge disclination is added at point K in Figure 6-5e to prevent overlap in region △LKN.

To confirm the presence of disclinations generated by GB migration, a Burgers circuit analysis has been conducted in the region where GB migration takes places citeKroner1. In the case of dislocations, such analysis identifies a characteristic translational closure failure whose value does not depend on the path of the circuit. When carried out on disclinations, this analysis identifies a characteristic rotational closure failure that does not depend on the path of the circuit. Figure 6-6 shows a circuit around a negative wedge disclination in a right-handed screw sense. A triad of lattice vectors is displaced along the circuit from A to B. In a reference lattice, there is no change in its orientation when the triad returns to A. In the deformed structure, however, there is a rotational closure failure. The rotation required to reorient the triad back to its original orientation is just the misorientation of GB1. The Burgers circuit analysis also justifies the use of discrete disclinations, instead of modeling internal stresses created during SDGBM with arrays of hypothetical dislocations.

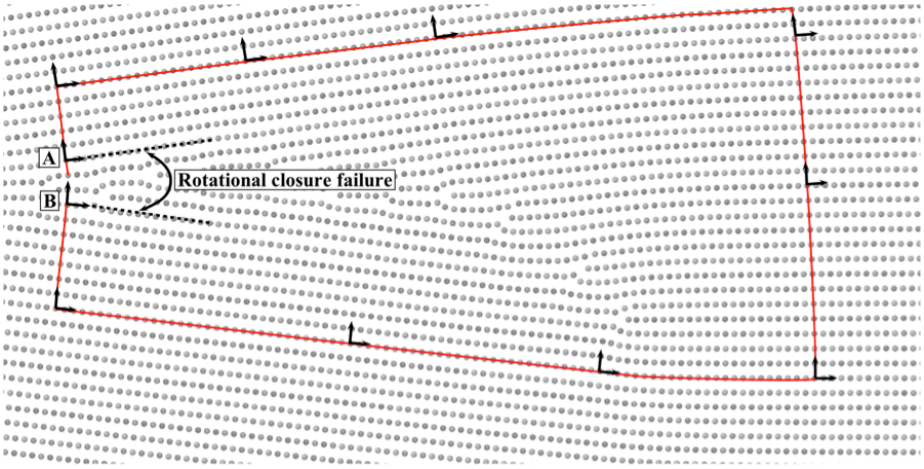

Figure 6-6: Burgers circuit analysis around a disclination.

6.2.2 Stress fields around disclination dipoles

The σ_{zz} (tensile) stress field calculated from the simulations in Figure 6-2 at 1.5% applied shear strain and shown in Figure 6-7a and b gives clear evidence of discrete, well separated, clearly identifiable disclinations at the predicted locations. The stress field of each disclination translates with the disclination as it moves during SDGBM.

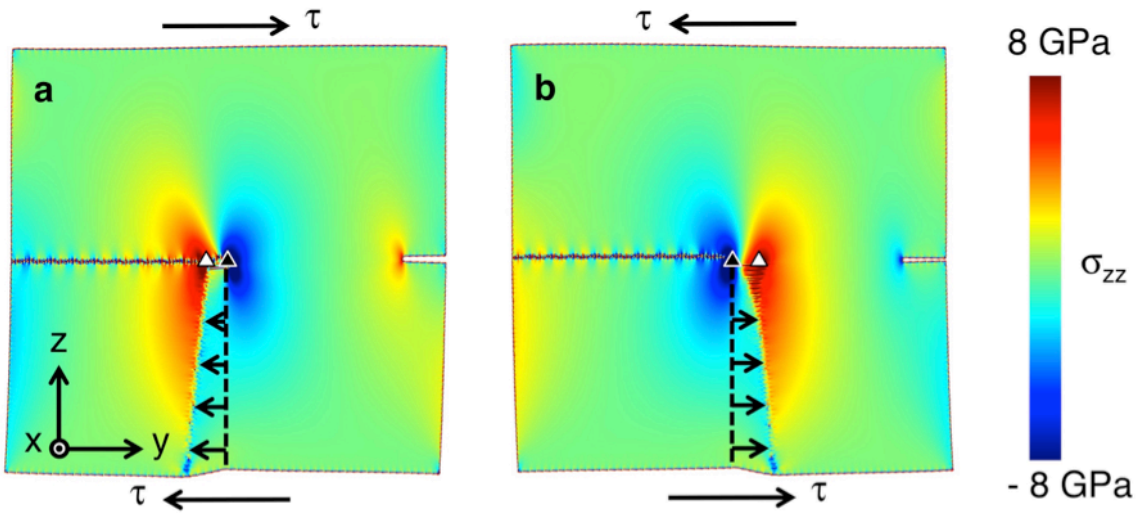

Figure 6-7: (a) σ_{zz} field calculated from atomistic simulations when GB1 migrates away from the crack and (b) toward the crack. Positive and negative disclinations coincide with the compressive (blue) and tensile (red) stress concentrations, respectively.

To verify the stress fields around disclination dipoles computed from atomistic simulations, we used the finite element method (FEM) implemented in the commercial software package COMSOL to calculate the stress and displacement fields due to surface image stresses generated by disclination dipoles in the model microstructure shown in Figure 6-2. The size and shape of the FEM model is identical to that in the atomistic simulations. Details of the FEM implementation is described in Chapter 3.

The disclination strength used in the FEM model is calculated as the tilt angle of GB1, which is equal to 14.69°. In the calculation, the migration distance of GB1 is fixed to be 14nm. One disclination of the dipole is placed at the center of the cell while the other is placed 14nm away. The stress fields calculated using FEM are in excellent

agreement with out atomistic simulations. Figure 6-8 shows the σ_{zz} component of the complete stress field generated when GB1 migrates in either direction. This should be compared with the stress field obtained in the atomistic simulation and shown in Figure 6-7.

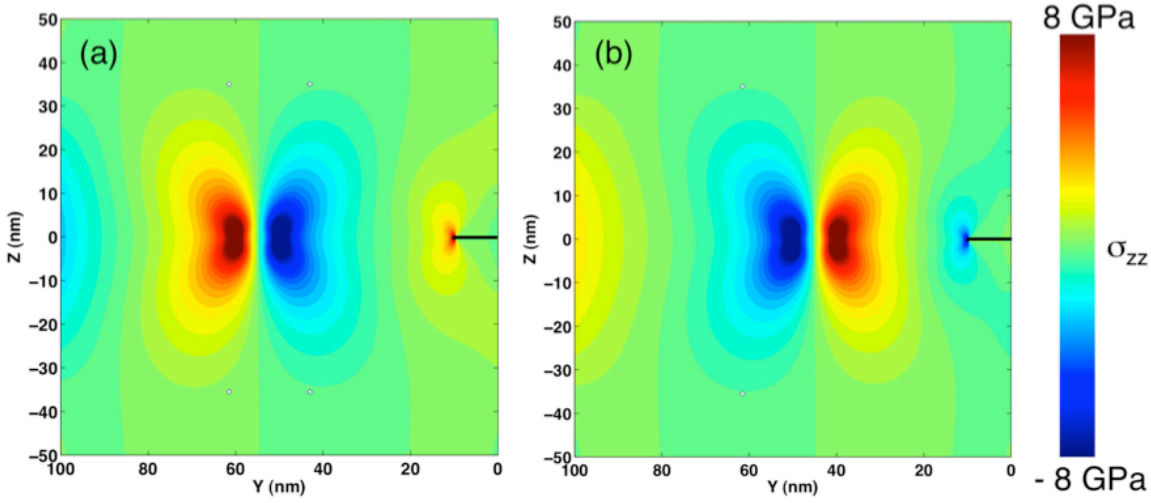

Figure 6-8: FEM calculation of σ_{zz} component of stress fields generated by wedge disclination dipoles in the model shown in Figure 6-2 (a) when GB1 moves away from the crack and (b) when GB1 moves toward the crack.

6.2.3 Crack healing due to disclination dipoles

The internal stresses generated by migrating GBs in an infinite solid may be computed analytically by superimposing the stress fields of positive and negative wedge disclinations, which have been known for over a century. In a finite solid, a disclination dipole will additionally induce tractions on the free surfaces. Therefore, image stresses will arise to satisfy traction-free boundary conditions [53]. It is these image stresses that are responsible for the crack healing mechanism described here. To substantiate this claim, we used the FEM to assess the effect of surface image stresses on the disclination-induced deformation of the model shown in Figure 6-2. The directions and magnitudes of relative crack surface displacements calculated from the image stresses alone are in excellent quantitative agreement with atomistic simula-

tions as are the stress fields calculated by FEM. Figure 6-9 shows the u_z component of displacement fields generated by image forces on the free surface. The crack surfaces move apart from each other when GB1 moves away from the crack and toward each other when GB1 moves toward the crack, which agrees with the simulation results.

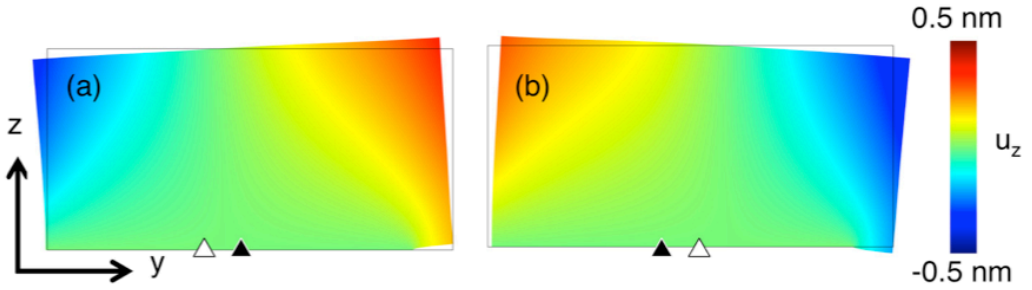

Figure 6-9: FEM calculation of u_z component of displacement fields generated by image stresses due to the free surfaces in the model shown in Figure 6-2 when GB1 moves away from the crack and (b) when GB1 moves toward the crack. Crack opening and closing occurs as expected from the atomistic model.

Although free surface image stresses are not present at internal intergranular cracks, disclinations formed during SDGBM may still cause them to open or close. Wedge disclinations may attenuate or amplify crack tip stress intensities of internal cracks [112], leading to additional, mixed-mode crack surface displacements. This effect, known as shielding or antishielding, may be expressed as a change in the stress intensity at the crack tip, ΔK. For a disclination dipole lying on the crack plane ahead of a semi-infinite crack,

$$\Delta K_I = \frac{\sqrt{2}}{2} \frac{\mu\omega}{2\pi(1-\nu)} (\sqrt{d_+} - \sqrt{d_-}), \tag{6.1}$$

where μ is the shear modulus, ν is Poisson's ratio, ω the disclination strength, and $d_\pm$ the distance from the crack tip to the positive (negative) wedge disclination.

Equation 6.1 predicts that larger GB migration distances lead to larger ΔK_I magnitudes and therefore a stronger influence on the crack. Subscript I indicates that the stress intensity generated by the disclinations is equivalent to Mode I (tensile/compressive) loading and gives rise to crack opening when $d_+ > d_-$ and closing

when $d_+ < d_-$. Healing of periodic (semi-infinite) as well as finite-length internal intergranular cracks through this mechanism is also observed.

6.3 Healing of nanocracks under tension

A firm understanding of the disclination-based mechanism of crack healing enables us to design microstructures that heal cracks even under monotonic external tensile loading, which would normally cause crack opening and advance. In Figure 6-10, we show a bicrystal containing a nanocrack and a symmetric tilt GB designed to migrate towards the crack under an applied tensile load. Since the uniform migration of a GB alone would not change the internal stress distribution in a bicrystal and therefore would not influence crack face displacements, we placed an impenetrable precipitate ahead of the advancing GB to block the motion of part of the GB. The precipitate, shown in blue in Figure 6-10a, is created by requiring all the atoms in it to displace as a rigid body.

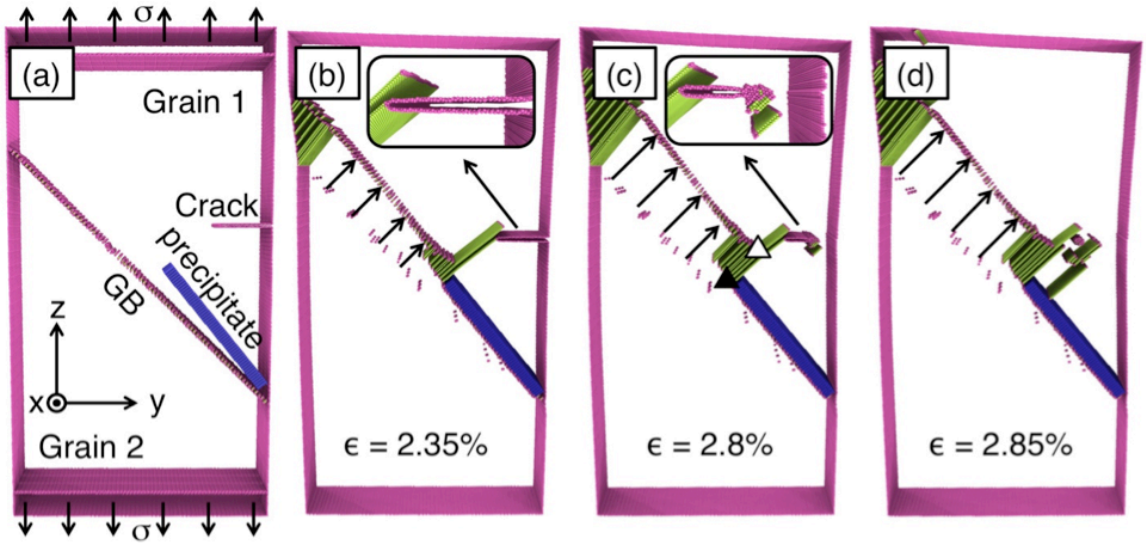

Figure 6-10: (a) Initial configuration and loading conditions. (b) Crack opens slightly due to applied tensile load; the GB begins to migrate towards the crack; part of the GB is blocked by the rigid precipitate. (c) Crack begins to heal as the part of the GB not blocked by the precipitate migrates further; white and black triangles indicate negative and positive disclinations, respectively (see Figure 6-5). (d) Complete crack healing. All perfect crystal atoms have been suppressed for clarity.

Tensile loading is applied on the surfaces normal to the z-direction. The crack surfaces initially open under the applied load and the GB migrates as expected. With further loading, part of the GB impinges upon the impenetrable precipitate while the remainder continues to move, as shown in Figure 6-10b. With continued loading, the crack surfaces cease opening and eventually begin to close. Figure 6-10c shows the moment when the crack faces touch and the crack begins to heal while in Figure 6-10d the crack has healed completely. Thus, we have successfully designed a microstructure where GB migration is used to achieve a counterintuitive result: complete crack healing under monotonic applied tensile loading.

The stress field inside the bicrystal corresponds to that of the disclination dipole shown in Figure 6-10c. This dipole would not have formed had there been nothing to impede the migration of part of the GB. As the unimpeded section of the GB continues to migrate, it leaves behind a positive wedge disclination near the precipitate while the negative wedge disclination shown as an open triangle in Figure 6-10c approaches the crack. The resulting disclination dipole induces closing displacements on the crack surface, which compete with the opening displacements arising from the external load. At a critical GB migration distance, the net displacement of the crack surface switches from opening to closing and the crack eventually heals despite the continuing tensile loading.

The effect of SDGBM on crack healing and advance in Ni is not symmetrical: less migration is required to heal cracks than to advance them. Figure 6-11 plots crack length as a function of GB migration distance for the simulation shown in Figure 6-2. The crack begins to close once GB1 moves towards it by 7.2nm. However, dislocation emission does not occur until GB1 has migrated 27.7nm away from the crack. The simulation illustrated in Figure 6-2 was repeated with the misorientation of GB1 reversed such that its effect on the crack is reversed: migration away from the crack closes it and migration towards the crack opens it. As shown in Figure 6-11, the amount of migration required to heal the crack in this case is again smaller than that required to advance it.

This asymmetry has potentially far-reaching consequences: it suggests that in

materials where GBs are equally likely to move towards cracks or away from them, SDGBM-induced crack healing will occur more frequently than SDGBM-induced crack advance. Thus, SDGBM may inhibit fracture by closing small cracks and impeding the formation or propagation of others. It is especially relevant to NC materials because GB-related mechanisms such as GB sliding and SDGBM often play a larger role in their deformation than does conventional dislocation plasticity [113, 114]. This proposition is consistent with studies that reported enhanced ductility in NC materials where SDGBM occurred [115, 116, 117]. The frequency of disclination-induced crack healing in real microstructures is not currently known. However, studies of fracture in nanopillars and nanowires suggest that direct experimental investigations of such phenomena are becoming possible [118, 119].

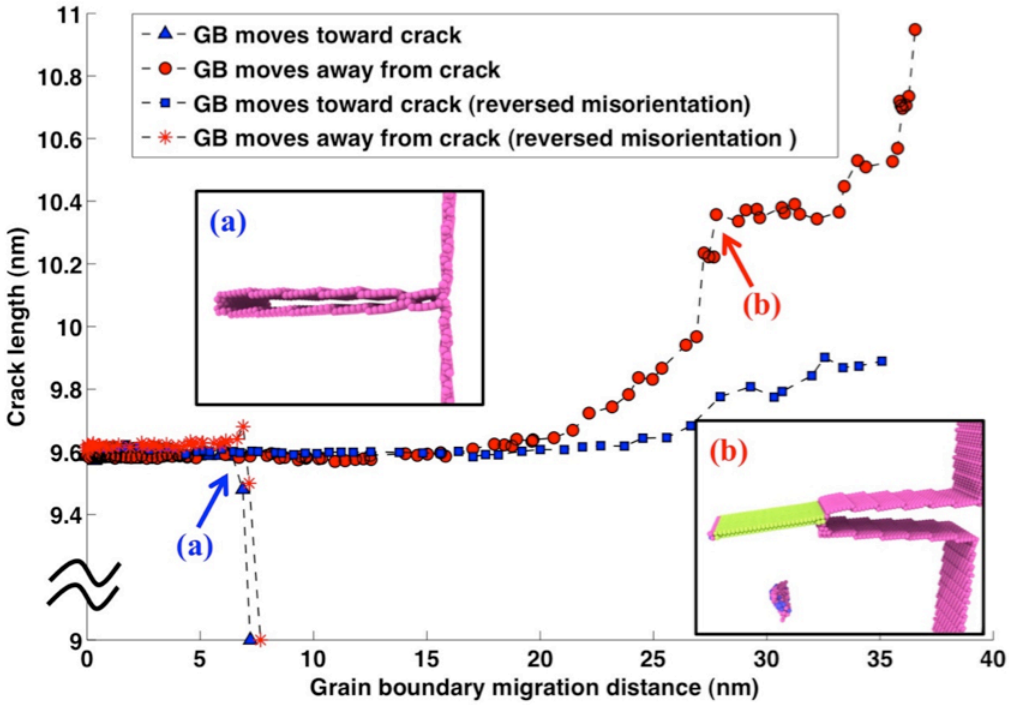

Figure 6-11: The relationship between crack length and GB1 migration distance.

6.4 Healing of nanocracks in the 3D microstructure.

In this section, we further examines the possibility of crack healing in the 3D microstructure of metals. We build a model 3D nc-Pd grain structure composed of uniform, space-filling truncated octahedra of width d=20nm, measured between two opposing hexagonal faces, as illustrated in Figure 6-12. This is a reasonable representation of nc-Pd created by consolidation of Pd nanoclusters synthesized through inert gas condensation [120]. Of the five convex polyhedra that tessellate 3D Euclidean space [121], truncated octahedra do so with least interface area per unit volume [122], resulting in models with low total GB energy. Such models are commonly used in studies involving 3D grain structures [123, 124].

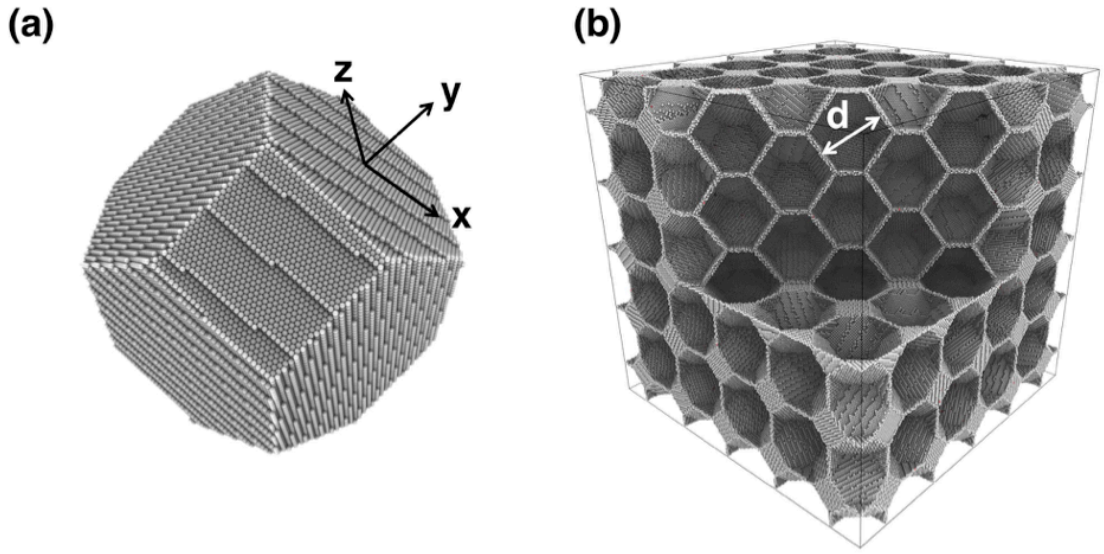

Figure 6-12: (a) A crystalline Pd grain shaped as a truncated octahedron. (b) The nc-Pd model used in the present study. For clarity, atoms with perfect face-centered cubic (fcc) environments are not shown.

We carry out MD simulations using LAMMPS [86] software and an EAM potential for Pd [90]. Our model has dimensions 40nm $\times$ 40.8nm $\times$ 35.4nm with periodic boundary conditions applied in all directions. It contains $\sim$4.25M atoms. We introduce a 7.5nm $\times$ 7.5nm square-shaped crack of thickness 1nm in the vicinity of one of the GBs by removing atoms, as shown in Figure 6-13a. We apply external loading

by iteratively shearing the supercell by γ_{xz}=0.1% followed by 5ps of MD relaxation after each strain increment, yielding an average strain rate of $2 \times 10^8/s$.

Figure 6-13 shows the effect of loading on the crack in nc-Pd: the crack progressively closes, even though the applied strain is simple shear and has no net compressive component. At an average shear strain of γ_{xz}=4.05%, the crack surfaces far from the GB touch and bond (see Figure 6-13b). Concurrently, Shockley partial dislocations with $[1\bar{1}2]$ Burgers vectors nucleate from the crack faces where bonding occurs. They are followed by trailing partials with $[21\bar{1}]$ Burgers vectors. The emitted dislocations have net Burgers vectors perpendicular to the crack surfaces, consistent with crack closure. At an average shear strain of γ_{xz}=4.3%, the nanocrack bonds along the entirety of both of its surfaces and is completely healed (see Figure 6-13b). Further loading leads to nucleation of dislocations at GB triple junctions followed by their propagation through the grains and absorption at opposing GBs.

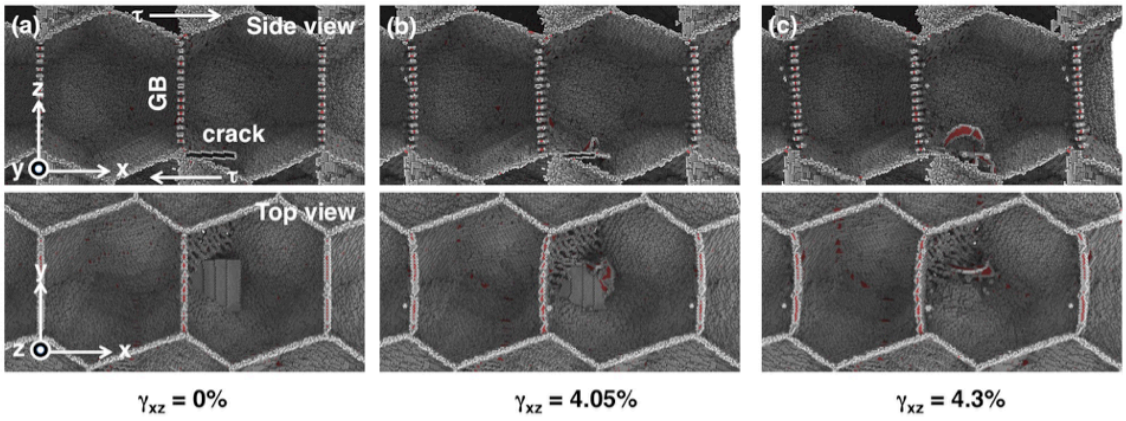

Figure 6-13: Simulation of a crack in nc-Pd during shear loading. The top row shows the crack edge-on while the bottom row shows it in plan-view. Applied strains are indicated below the figures. For clarity, atoms with perfect fcc environments are not shown. (a) Initial model structure. (b) Upon shearing, the crack begins to close at its right end (far from the GB). (c) Eventually, the crack heals completely.

The closure and healing of cracks in nc-Pd under simple shear is surprising because no net compressive stress is applied. To emphasize this point, we perform another MD simulation on a model containing a crack of identical shape and dimensions as that shown in Figure 6-13, but located in a single crystal (see Figure 6-14a). The

orientation of the single crystal is the same as that of the grain in the nc-Pd containing the crack. All the other simulation parameters remain the same. As shear loading progresses to stresses of ∼1.5GPa and shear strains of γ_{xz}=4.4%, Shockley partial dislocations nucleate at the crack and propagate away in the plane of the crack (see Figure 6-14b). No crack closure is observed at any time during this simulation.

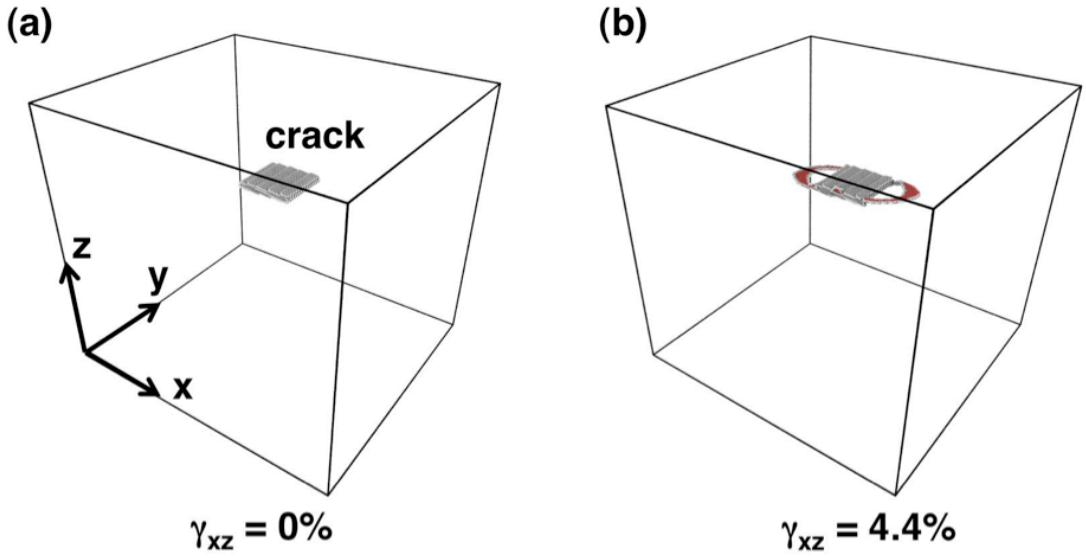

Figure 6-14: Simulation of a crack in single crystal Pd during shear loading. For clarity, atoms with perfect FCC environments are not shown. (a) Initial model structure. (b) Upon shearing, Shockley partials dislocations are emitted from the crack tip, but no crack healing is observed.

The reason for the different crack behaviors in nc-Pd and single crystal Pd is the non-uniform, microstructure-induced internal stress that develops within the former upon external loading. To understand how this stress is generated, we carry out a third MD simulation: this one on the same nc-Pd structure as shown in Figure 6-13, but with no crack. Atomic-level virial stresses are calculated in all three simulations at γ_{xz}=4.0%, i.e. just below the strain at which crack closure initiates in the simulation in Figure 6-13. Figure 6-15 shows the spatial distribution of σ_{zz}: the normal stress component perpendicular to the crack faces. This distribution is highly non-uniform in nc-Pd (Figure 6-15b): it concentrates in alternating lobes of tension and compression in the vicinity of GBs. In elastically anisotropic materials, such patterns

arise from compatibility strains due to the different crystallographic orientations of adjacent grains [53, 125].

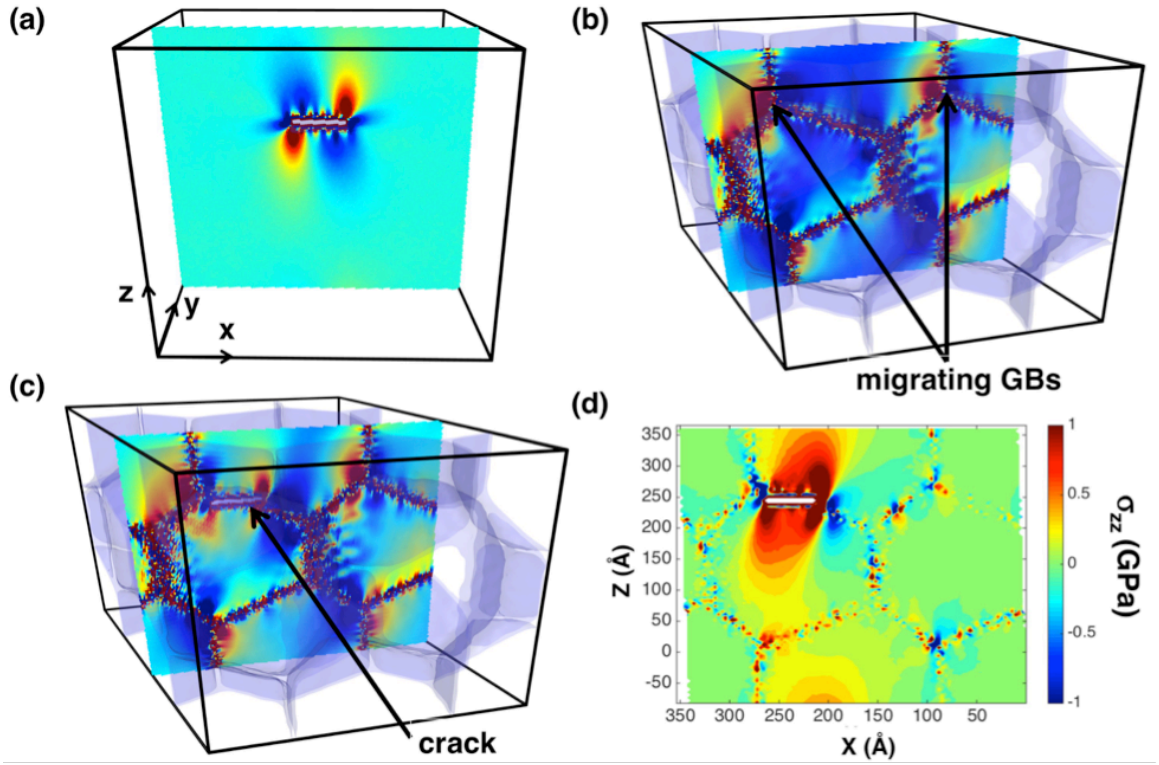

Figure 6-15: The spatial distribution of σ_{zz}: the stress component normal to the crack faces at 4% shear strain calculated in (a) single crystal Pd, (b) nc-Pd without cracks, and (c) nc-Pd with a crack. The stress in (c) minus the stress in (b) is plotted in (d). The colorbar in d) applies to a), b), and c), as well.

Moreover, nc-Pd also exhibits local inelastic atomic re-arrangements—such as GB shearing and migration—even prior to the onset of plastic flow. These inelastic events also contribute to internal stresses in nc-Pd. For example, the GB nearest to the crack in Figure 6-13a) is a $\Sigma 367(110)$ symmetrical tilt GB with tilt angle $\theta = 14.69°$. It consists of an array of edge dislocations and easily migrates under external shear loading [101]. These differences in the nominally elastic response of nc-Pd and single crystal Pd are apparent in the stress-strain curves obtained from our simulations and shown in Figure 6-16: GB-mediated plasticity in the early, nominally-elastic stage of deformation relieves some of the stress in the model, giving rise to a lower apparent shear modulus than the simulation in single crystal Pd.

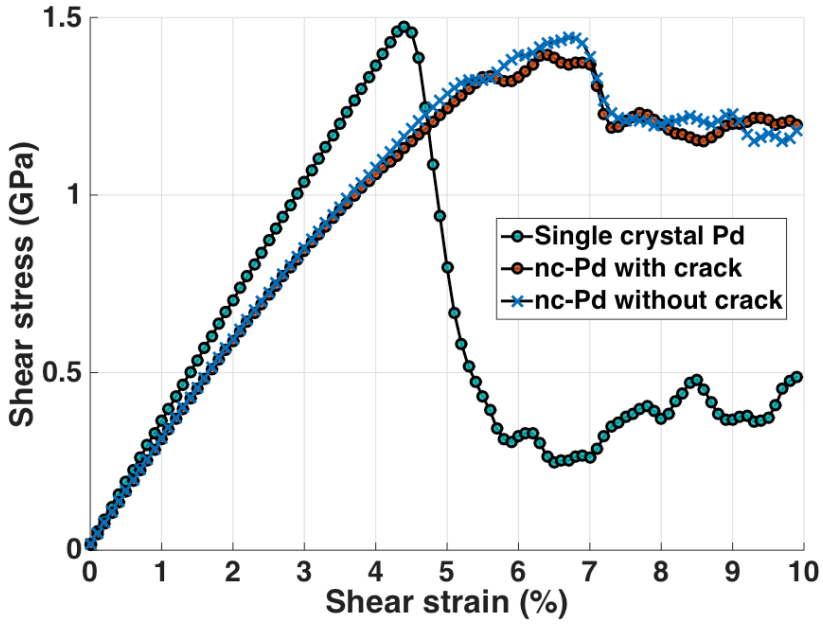

Figure 6-16: Stress-strain curves for the three MD simulations conducted within this study.

The σ_{zz} stress component from the single crystal simulation is shown in Figure 6-15a. It exhibits the characteristic shape of mode II crack tip stress fields, with tension on one side of the crack plane and compression on the other [25]. As expected, this type of stress field does not lead to closure of the crack. However, Figure 6-15b shows that, in nc-Pd, σ_{zz} has a high, compressive value in the region where the crack is later introduced. These microstructurally-induced internal stresses gives rise to local compression on the crack, as shown in Figure 6-15c. Figure 6-15d plots σ_{zz} in nc-Pd with the crack minus σ_{zz} in nc-Pd without the crack, i.e. the crack-induced stresses in nc-Pd. These stresses appear qualitatively different than those in Figure 6-15a because, in addition to the characteristic mode II elastic fields for cracks in uniform media [25], they also incorporate crack-induced image stresses arising from the non-uniform internal fields generated by the nc-Pd microstructure.

The present study demonstrates that complete closure and healing of nanocracks in realistic, 3D microstructures is possible, even when no net compressive loads are applied. Therefore, the mechanically-induced crack healing behavior is not confined

to model 2D microstructures. In both studies, crack healing arises due to internal stresses generated by non-uniform, evolving microstructure, e.g. through compatibility strains and inelastic GB response. These observations illustrate the importance of accounting for microstructurally-induced internal stresses when predicting the behavior of cracks under mechanical loading. Other forms of microstructure evolution—e.g. martensitic transformations [126, 127] or differential distortion [128]—also generate internal stresses and so may also be expected to influence crack behavior. It remains to be seen whether small-scale crack closure events such as the one described here may be harnessed to mitigate material degradation in engineering applications.

Chapter 7

Discussion and conclusion

This chapter first discusses the implication of the work in this thesis, followed by a brief summary of the thesis as well as open questions.

7.1 Discussion

Knowing the fracture toughness of individual GB is of great significance. It can not only provide insights for designing stronger materials by GB engineering, but also can be used as input to build accurate lifetime models to predict failures. Unfortunately, the dependence of fracture toughness on GB types is still unknown. Classical models simplify this as a classification problem−given the type of GB, identify which category it belongs to, intrinsically ductile (high toughness) or intrinsically brittle (low toughness). The well-known criterion for this classification problem, proposed by Rice and Thomson [4, 34], can correctly predict which one is intrinsically brittle or ductile for a few type of metals as well as the threshold temperature for crack tip plasticity in α-Fe [4]. However, in general, its predictability is limited.

The newly discovered DRED fracture mechanism described in Chapter 5 contrasts with the classical view of Rice and Thomson. Their fracture criterion recognizes that, in general, bond breaking and dislocation emission near crack tips occur at different applied loads [68, 36]. Under quasi-static conditions, the process that requires lower load initiates first and relaxes stresses in the vicinity of the crack. Subsequent re-

loading of the crack re-initiates the same process. Thus, bond breaking and dislocation emission are mutually exclusive in this simple model: during continuous loading, only the process requiring the lower load occurs. However, in DRED, bond breaking and dislocation emission are not mutually exclusive, but rather act in concert: the onset of brittle fracture generates transient elastic fields that lead to the emission of dislocations, which, in turn, shield and arrest the crack. Both DRED and Rice's model focuses on crack-tip processes and does not address mesoscale phenomena, such as the evolution of ordered dislocation structures and their interaction with the crack [129, 130, 131, 132].

The investigation of crack propagation mechanisms in Chapter 5 hints on the conditions under which crack propagates by ductile, brittle or DRED mechanism. Similar to Rice's model, the conditions can be expressed in terms of critical stress intensity factors for decohesion K_{Ic}^{dec} and dislocation emissions K_{Ic}^{disl}. When $K_{Ic}^{dec} > K_{Ic}^{disl}$, dislocations will be emitted first, which will tip the balance towards plastic blunting of the crack tip, leading to ductile fracture (see Figure 7-1a). This condition for ductile fracture is the same with Rice's criterion.

When $K_{Ic}^{dec} < K_{Ic}^{disl}$, whether crack propagates by DRED or pure brittle fracture depends on the difference between K_{Ic}^{dec} and K_{Ic}^{disl}. The stress intensity for a crack advancing at steady state velocity v is

$$K_I(v) = k(v)K_{Is}, \tag{7.1}$$

where K_{Is} is the stress intensity for a static crack of identical shape and $k(v)$ is a function that decreases monotonically to zero as v increases to Rayleigh wave speed. Therefore, we expect the transient stress intensity to reach a maximum value (see Figure 6-12b), $K_{It}^{max} = K_{Ic}^{dec} + \Delta$, as an initially stationary crack accelerates to v, where F is a function of the loading conditions and crack geometries. If $K_{Ic}^{disl} > K_{It}^{max} = K_{Ic}^{dec} + \Delta$, the condition for dislocation emission will never be reached before the transient stress intensity begins to drop. Therefore, crack will propagate by pure brittle fracture under this condition (see Figure 7-1b).

When $K_{Ic}^{disl} - \Delta < K_{Ic}^{dec} < K_{Ic}^{disl}$, crack can propagate by either DRED mechanism or brittle fracture depending on the post-yielding plastic deformation process. Dislocation process will be first triggered as a result of the rising crack tip stress intensity factor. In the absence of local hardening, the nucleated dislocations will propagate away and relax the crack tip stress, leading to crack arrest (see Figure 6-12c). This is the DRED mechanism. However, in the presence of local hardening, the motion of dislocations is restricted and therefore the crack tip stress can not be relaxed through plasticity. In this case, crack propagates continuously in a brittle-like manner (see Figure 6-12c).

DRED also sheds light on how to optimize fracture toughness. The key is to prevent onset of pure brittle fracture by increasing K_{Ic}^{dec} and decreasing K_{Ic}^{disl}. K_{Ic}^{dec} may be altered by changing GB character [5, 2, 133] or through alloying [134]. Razumovskiy et. al. investigated the effect of transition metal alloying elements on a typical high-angle GB in Ni using first-principle calculations and identified Zr, Hf, Nb, Ta and B to have positive impact on increasing K_{Ic}^{dec} [134]. K_{Ic}^{disl} depends on unstable stacking fault energy γ_{us} ($K_{Ic}^{disl} \sim \sqrt{\gamma_{us}}$, in 2D) and the orientation of slip systems in the adjacent grains [34]. Additional strategies for increasing toughness may also emerge from an improved understanding of the transient fields that follow the onset of brittle fracture in DRED. For example, it may be possible to reduce the amount of brittle fracture prior to dislocation emission by enhancing the rate at which the transient stress intensity, K_{It}, increases or by amplifying the shielding effect of emitted dislocations [55]. Indeed, the example of DRED shows that much remains to be understood concerning the role of transient stresses in the micromechanics of fracture.

The understanding of crack propagation mechanism in 'nerd' environment is of great importance for investigation of H-induced intergranular fracture. So far, numerous mechanisms have been proposed to account for H embrittlement, including H-induced decohesion [135, 136], H-enhanced localized plasticity [137], hydride-formation and cleavage [138] and absorption-induced dislocation emission (AIDE) [139]. In the model of AIDE, the absorption of H to the crack tip facilitates the

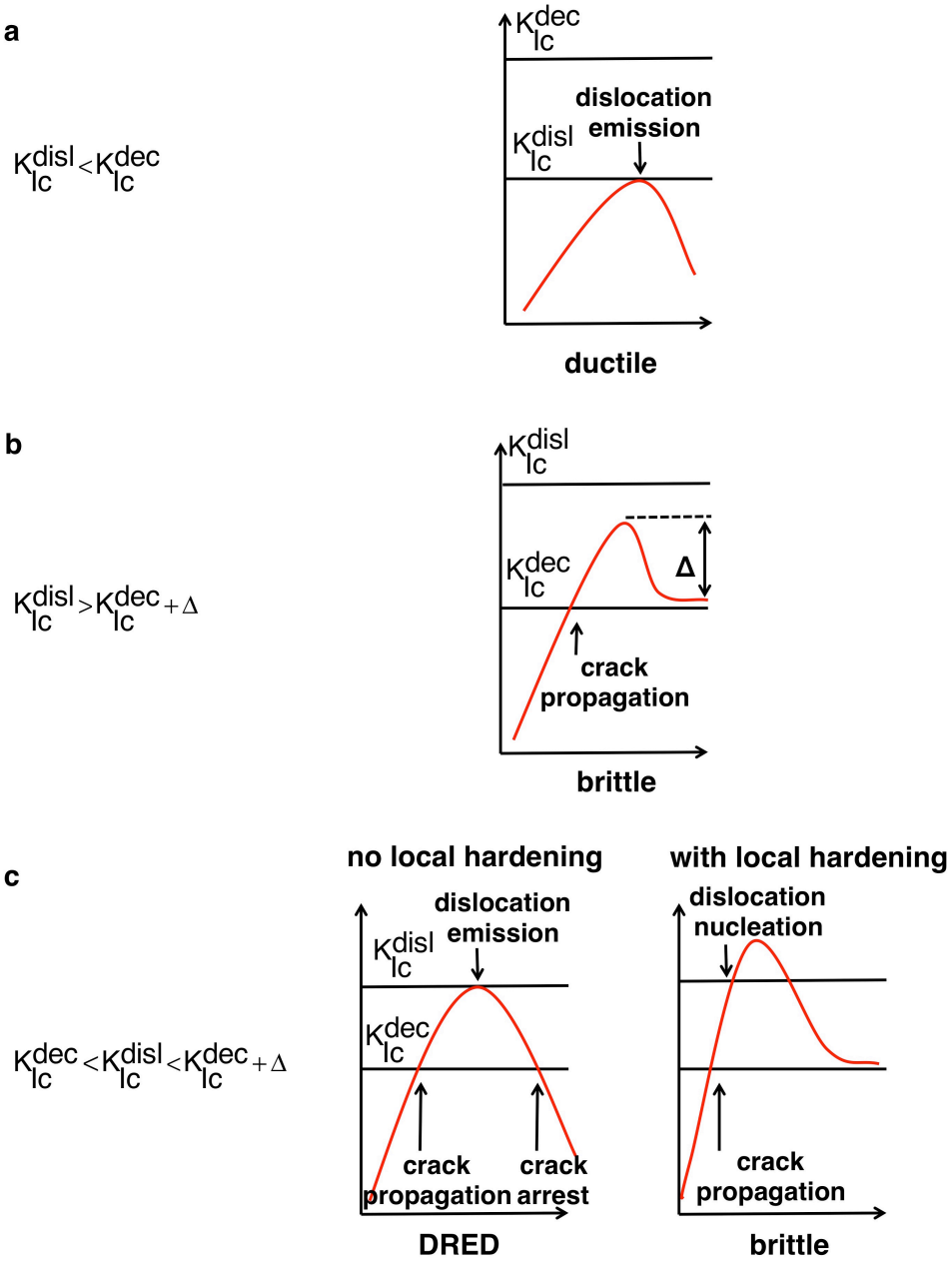

Figure 7-1: Criterion for ductile, DRED, and brittle fracture.

emission of dislocation on suitably inclined slip planes, promoting the coalescence of cracks with micro- or nano- scale voids ahead of cracks. However, if crack propagation in H environment is via DRED mechanism, then dislocations are only emitted after a burst of brittle crack advance. In this case, the decrease in K_{Ic}^{disl} due to absorption of H to the crack tip will actually reduce $K_{Ic}^{disl} - K_{Ic}^{dec}$, leading to an earlier arrest of the crack. Thus, the H absorbed to the crack tip in AIDE does not accelerate the fracture process, but rather hinders crack propagations.

A recent work by Kirchheim shows that the surface separation energies at the GB have different values for fast and slow cracks [140]. Hydrogen energetically prefers to stay on a pair of free crack surfaces rather than at GBs [141]. Therefore, the H concentration on the crack surface during fast crack propagation is equal to half the H content at the uncracked GB, which is lower. However, for slow crack propagation, the H concentration on the crack surface will always be in equilibrium and therefore higher than in the case of fast separation. Kirchheim shows that the surface separation energy for fast crack is higher than that for slow crack. When crack propagates by DRED mechanism, it is slow on average but fast during the intermittent burst. Therefore, H has no time to diffuse to the crack surface during each burst, leading to a lower K_{Ic} for DRED in the presence of H than that for slow cracks.

Besides the understanding of fracture mechanisms, another way to find the relationship between fracture toughness and GB types is to collect a sufficient amount of data on GB's fracture toughness and then use the data mining approaches to infer the governing relationships. Given the huge number of GBs, acquiring this data from experiments would be almost impossible. In this thesis, we proposed a relatively simple and fast method for computing critical energy release rates from atomistic simulations. Our method relies solely on global thermodynamic quantities and is not limited to LEFM. Therefore, it applies to fracture at the onset of crack tip dislocation nucleation as well as in the presence of extensive plastic deformation.

Experimentally determined values of G_c for pure Ni and Ni-base alloys range from $111 kJ/m^2$ to $854 kJ/m^2$ [142, 143, 144]. These G_c values are much higher than the ones calculated in Chapter 5. The reason for this discrepancy is a difference in

fracture mode. Pure Ni and Ni-base alloys undergo transgranular ductile fracture, where cracks propagate by void growth and coalescence [145]. This mechanism is qualitatively different from the one we investigated. Indeed, our atomistic models are too small and the simulations are conducted at too high a strain rate to display fracture by void growth and coalescence. However, when we compare our simulations with experiments where a similar, brittle-like fracture mode was observed, we find that the G_c values we computed are comparable to those obtained experimentally.

For example, in some intermetallic alloys, local ordering limits the number of independent slip systems, leading to fracture behavior similar to that in our simulations. Change et.al. found that the room temperature fracture toughness of single crystal NiAl ranges from $3.0MPa\sqrt{m}$ for cracks along the soft <110> orientation to $9.31MPa\sqrt{m}$ along the hard <100> orientation [146]. The corresponding G_c values−computed using Equation 2.1 with Youngs modulus E = 187.8GPa and Poissons ratio ν=0.3135[147]−range from $43.2J/m^2$ to $416J/m^2$. They are much larger than the surface separation energy $2\gamma_{<100>} = 1.9J/m^2$ [147], indicating that plasticity accompanies crack propagation. Moreover, they are comparable with the range of G_c values obtained in our work (see Figure 5-37): $27.0J/m^2 - 141J/m^2$ (naturally, we do not expect G_c for intermetallic NiAl and fcc Ni to be identical). Assuming that NiAl follows the same scaling relationship as shown in Figure 5-37, we estimate that the size of the plastic zone in these experiments ranges from ∼30nm to ∼200nm for cracks along <110> and <100> directions, respectively. Intergranular cleavage in copper (Cu) embrittled by bismuth (Bi) is another example of brittle-like fracture in an FCC material. Wang et.al. measured $G_c = 28J/m^2$ and $54J/m^2$ along a $\Sigma 9$ symmetric tilt and a random GBs, respectively. These values are also comparable with our calculations.

Hydrogen introduced into Ni causes the fracture mode to change from ductile transgranular to brittle intergranular [148], albeit with copious accompanying plasticity [1]. G_c is thereby greatly reduced, e.g. to $19kJ/m^2$ for Ni-base alloy X-750 [149] or $24kJ/m^2$ for Ni-base alloy 690 [150]. Despite the similarity in fracture mode, these values are nevertheless orders of magnitude larger than the ones obtained in

the present work. The likely reason for this discrepancy is the limited of size of our atomistic models. Using the relationship between G_c and L obtained from Figure 5-37, we infer that to observe G_c values comparable to those found experimentally in H-charged Ni-base alloys would require models with edge lengths of $\sim 6\mu m$.

Our work makes important improvements on previous efforts to model fracture. However, it also shares some of its shortcomings. Although our model sizes are large by comparison to most previous simulations, they still small by comparison to most experiments on Ni. Therefore, it is impossible to capture certain fracture behaviors in the simulations, such as ductile fracture by void growth and coalescence. To simulate those behaviors, model sizes on the order of tens or hundreds of microns are needed, requiring trillions of atoms or more. This number of atoms can probably not be simulated in any computer in the near future. For models of such size, it is more practical to conduct simulations using discrete dislocation dynamics (DDD) [151, 152] or hybrid atomistic/DDD methods [153, 154].

Another shortcoming of using atomistic simulations to study fracture are the extremely high strain rates they necessitate. Fracture experiments are usually performed with strain rates ranging from $10^{-5}/s$ to $10^{2}/s$. However, in MD simulations, the duration of individual simulations is restricted to nano- or micro-seconds. Reaching strains of several percent therefore requires strain rates ranging from $10^{7}/s$ to $10^{10}/s$, i.e., many orders of magnitudes higher than in experiments. This means that our simulations overestimate K_{dis}. In a simulation with much lower strain rate, thermal activation may make dislocation emission easier, thereby reducing K_{dis}. Strain rate is unlikely to affect the surface separation energy much, so the reduction of K_{dis} is likely to favor ductile fracture over brittle fracture.

Our simulations were conducted in pure FCC Ni. In reality, even ultrapure Ni contains some concentration of impurities. These impurities may have a tendency to segregate to grain boundaries. Thus, although their volume-averaged concentration may be on the order of 0.01%, their concentration at grain boundaries may be significantly higher. As discussed in this section, impurities may have a strong effect on surface separation energies [134]. However, because reliable classical potentials are

not available for most impurity species, their effect on the overall fracture process cannot yet be simulated.

Finally, pure Ni is not used in engineering applications. Rather, it is used as the base element in a wide range of multicomponent alloys, such the Inconel® [155, 156], René® [157], or Nimonic® [158] families. In addition to containing large concentrations of Cr, Fe, or Co, these alloys also incorporate a variety of intermetallic precipitates and inclusions [159, 160, 161]. The effect of such microstructural elements on crack tip fracture has yet to be modeled.

7.2 Conclusion

In this thesis, we use careful atomistic simulation and in-depth statistical analysis to investigate the intergranular fracture mechanism in Ni. An unexpected new intergranular fracture mechanism, decohesion restrained by emission of dislocations, is discovered. This mechanism departs significantly from the classical picture of crack tip fracture processes, as described by the criterion of Rice and Thomson. Moreover, it challenges the long-held, implicit assumption that static or steady state stress fields are sufficient to describe crack-tip processes within the micro-mechanics of fracture.

We also found that the fracture behaviors rely on not only the initial response of the crack at the onset of fracture, as proposed by Rice and Thomson, but also the various deformation process occurring in the later stage of fracture. We discovered that the local hardening in the vicinity of the crack tip, caused by deformation twining or formation of stable dislocation locks, can significantly reduce the fracture toughness and influence the fracture behaviors.

We developed a new method to estimate the critical energy release rate (and hence the toughness) of fracture from atomistic simulations. This method can be employed to fracture with extensive plastic deformations. It also enables fast generation of data on GB's resistance to fracture via atomistic simulations, which would facilitate the prediction of the relationship between fracture toughness and GB types.

In the course of investigating intergranular fracture in Ni, we accidentally discov-

ered a new crack healing mechanism in a 2D model structure whereby the generation and motion of crystal defects known as disclinations leads to complete healing of nanocracks. The disclinations are formed by stress-driven grain boundary migration. We also demonstrated that the complete closure and healing of nanocracks in realistic 3D microstructures is possible. This mechanism may enhance ductility in nanocrystalline materials by closing small cracks and suppressing the propagation of others.

7.3 Future directions

This thesis also opens a few possible research directions for better understanding GBs effect on fracture behaviors. Here lists a few topic that remain to be further investigated:

- What is the minimum difference between G_{dec} and G_{disl} that will result in pure brittle fracture instead of DRED?
- How the role of GBs on fracture will change in the presence of hydrogen and/or high temperature?
- How to design experiment to observe the crack healing phenomenon?

Bibliography

[1] M. Martin, B. Somerday, R. Ritchie, P. Sofronis, and I. Robertson, "Hydrogen-induced intergranular failure in nickel revisted," *Acta Mater.*, vol. 69, pp. 275–282, 2014.

[2] S. Bechtle, M. Kumar, B. Somerday, M. Launey, and R. Ritchie, "Grain-boundary engineering markedly reduces susceptibility to intergranular hydrogen embrittlement in metallic materials," *Acta Materialia*, vol. 57, no. 14, pp. 4148 – 4157, 2009.

[3] H. Kurishita, A. Ôishi, H. Kubo, and H. Yoshinaga, "Grain boundary fracture in molybdenum bicrystals with various< 110> symmetric tilt boundaries," *Transactions of the Japan institute of metals*, vol. 26, no. 5, pp. 341–352, 1985.

[4] J. R. Rice and R. Thomson, "Ductile versus brittle behaviour of crystals," *Philosophical Magazine*, vol. 29, no. 1, pp. 73–97, 1974.

[5] D. L. Olmsted, S. M. Foiles, and E. A. Holm, "Survey of computed grain boundary properties in face-centered cubic metals: I. grain boundary energy," *Acta Materialia*, vol. 57, no. 13, pp. 3694–3703, 2009.

[6] Y. Kaneko, K. Kitagawa, and S. Hashimoto, "Fatigue crack propagation in copper bicrystals having the grain boundaries of $\sigma 3$ vicinal domain," *Interface Science*, vol. 7, no. 2, pp. 147–158, 1999.

[7] V. Yamakov, E. Saether, D. Phillips, and E. Glaessgen, "Molecular-dynamics simulation-based cohesive zone representation of intergranular fracture pro-

cesses in aluminum," *Journal of the Mechanics and Physics of Solids*, vol. 54, no. 9, pp. 1899–1928, 2006.

[8] R. Raj and M. Ashby, "Intergranular fracture at elevated temperature," *Acta Metallurgica*, vol. 23, pp. 653–666, 1975.

[9] R. Fessler, "Studies reveal causes of stress-corrosion cracking.," *Pipe Line Industry*, vol. 44, pp. 37–39, 1976.

[10] S. Chiovelli, D. Dorling, A. Glover, and D. Horsley, "Main line failure resulted from combination of minor causes," *Oil and Gas Journal*, vol. 92, pp. 91–100, 1994.

[11] G. Schmitt, L. Sobbe, and W. Bruckhoff, "Corrosion and hydrogen-induced cracking of pipeline steel in moist triethylene glycoldiluted with liquid hydrogen sulfide," *Corrosion Science*, vol. 27, pp. 1071–1076, 1987.

[12] K. Aust, U. Erb, and G. Palumbo, "Interface control for resistance to intergranular cracking," *Materials Science and Engineering A*, vol. 176, pp. 329–334, 1994.

[13] G. Palumbo, P. King, K. Aust, U. Erb, and P. Lichtenberger, "Grain boundary design and control for intergranular stress-corrosion resistance," *Scripta Metallurgica*, vol. 25, pp. 1775–1780, 1991.

[14] A. Sutton and R. Balluffi, *Interfaces in Crystalline Materials*. Oxford University Press, 1995.

[15] T. Watanabe, "An approach to grain boundary design for strong and ductile polycrystals," *Res Mechanica*, vol. 11, pp. 47–84, 1984.

[16] C. Cheung, U. Erb, and G. Palumbo, "Application of grain boundary engineering concepts to alleviate intergranular cracking in alloys 600 and 690," *Materials Science and Engineering: A*, vol. 185, no. 1, pp. 39 – 43, 1994.

[17] T. Watanabe and S. Tsurekawa, "The control of brittleness and development of desirable mechanical properties in polycrystalline systems by grain boundary engineering," *Acta Materialia*, vol. 47, no. 15–16, pp. 4171 – 4185, 1999.

[18] M. Shimada, H. Kokawa, Z. Wang, Y. Sato, and I. Karibe, "Optimization of grain boundary character distribution for intergranular corrosion resistant 304 stainless steel by twin-induced grain boundary engineering," *Acta Materialia*, vol. 50, no. 9, pp. 2331 – 2341, 2002. Computational Thermodynamics and Materials Design.

[19] J. Tatami, T. Harada, K. Yasuda, and Y. Matsuo, *Influence of Twist Angle on the Fracture Toughness of (0001) Twist Boundary of Alumina*, pp. 211–218. John Wiley & Sons, Inc., 2008.

[20] Y. Qiao and A. Argon, "Cleavage cracking resistance of high angle grain boundaries in fe–3no. 3–6, pp. 313 – 331, 2003.

[21] J. Brosse, R. Fillit, and M. Biscondi, "Intrinsic intergranular brittleness of molybdenum.," *Scripta Metallurgica*, vol. 15, pp. 619–623, 1981.

[22] A. Suzuki, M. Gigliotti, and P. Subramanian, "Novel technique for evaluating grain boundary fracture strength in metallic materials," *Scripta Materialia*, vol. 64, no. 11, pp. 1063 – 1066, 2011.

[23] K. Sato, H. Miyazaki, Y. Ikuhara, H. Kurishita, and H. Yoshinaga, "Structure and strength of grain-boundaries in si bicrystals with< 111> twist misorientations," *Materials Transactions, JIM*, vol. 31, no. 10, pp. 865–872, 1990.

[24] J. Liu and B. Shen, "Direct measurement of the work of fracture for grain boundaries of twist misorientation about ń100ż in tungsten," *Metallurgical Transactions A*, vol. 15, no. 6, pp. 1289–1292, 1984.

[25] K. Broberg, *Cracks and Fracture*. Academic Press, 1999.

[26] P. Thomason, "Ductile fracture of metals," *Pergamon Press plc, Ductile Fracture of Metals(UK), 1990,*, p. 219, 1990.

[27] A. A. Griffith, "The phenomena of rupture and flow in solids," *Philosophical transactions of the royal society of london. Series A, containing papers of a mathematical or physical character*, pp. 163–198, 1921.

[28] V. Lubarda, M. Schneider, D. Kalantar, B. Remington, and M. Meyers, "Void growth by dislocation emission," *Acta Materialia*, vol. 52, no. 6, pp. 1397–1408, 2004.

[29] T. Pardoen, I. Doghri, and F. Delannay, "Experimental and numerical comparison of void growth models and void coalescence criteria for the prediction of ductile fracture in copper bars," *Acta Materialia*, vol. 46, no. 2, pp. 541–552, 1998.

[30] I. Barsoum and J. Faleskog, "Rupture mechanisms in combined tension and shear—experiments," *International Journal of Solids and Structures*, vol. 44, no. 6, pp. 1768 – 1786, 2007. Physics and Mechanics of Advanced Materials.

[31] A. Azhdari, S. Nemat-Nasser, and J. Rome, "Experimental observations and computational modeling of fracturing in an anisotropic brittle crystal (sapphire)," *International journal of fracture*, vol. 94, no. 3, pp. 251–266, 1998.

[32] R. Armstrong, "Cleavage crack propagation within crystals by the griffith mechanism versus a dislocation mechanism," *Materials science and engineering*, vol. 1, no. 4, pp. 251–254, 1966.

[33] A. Kelly, W. Tyson, and A. Cottrell, "Ductile and brittle crystals," *Philosophical magazine*, vol. 15, no. 135, pp. 567–586, 1967.

[34] J. R. Rice, "Dislocation nucleation from a crack tip: an analysis based on the peierls concept," *Journal of the Mechanics and Physics of Solids*, vol. 40, no. 2, pp. 239–271, 1992.

[35] J. R. Rice and G. E. Beltz, "The activation energy for dislocation nucleation at a crack," *Journal of the Mechanics and Physics of Solids*, vol. 42, no. 2, pp. 333–360, 1994.

[36] Y. Cheng, Z.-H. Jin, Y. Zhang, and H. Gao, "On intrinsic brittleness and ductility of intergranular fracture along symmetrical tilt grain boundaries in copper," *Acta Materialia*, vol. 58, no. 7, pp. 2293–2299, 2010.

[37] G. Liu and G. Xu, "Nucleation of partial dislocations at a crack and its implication on deformation mechanisms of nanostructured metals," *Journal of the Mechanics and Physics of Solids*, vol. 57, no. 7, pp. 1078–1092, 2009.

[38] E. Tadmor and S. Hai, "A peierls criterion for the onset of deformation twinning at a crack tip," *Journal of the Mechanics and Physics of Solids*, vol. 51, no. 5, pp. 765–793, 2003.

[39] Y. Sun and G. E. Beltz, "Dislocation nucleation from a crack tip: a formulation based on anisotropic elasticity," *Journal of the Mechanics and Physics of Solids*, vol. 42, no. 12, pp. 1905–1932, 1994.

[40] G. Schoeck, "Dislocation emission from crack tips as a variational problem of the crack energy," *Journal of the Mechanics and Physics of Solids*, vol. 44, no. 3, pp. 413–437, 1996.

[41] G. Schoeck, "Dislocation emission from crack tips," *Philosophical Magazine A*, vol. 63, no. 1, pp. 111–120, 1991.

[42] G. Schoeck, "The emission of dislocations from crack tips: A critical assessment," *Materials Science and Engineering: A*, vol. 356, no. 1, pp. 93–101, 2003.

[43] G. Schoeck, "The formation of dislocation rings on a crack front," *Philosophical Magazine A*, vol. 74, no. 2, pp. 419–430, 1996.

[44] A. Argon, "Brittle to ductile transition in cleavage fracture," *Acta Metallurgica*, vol. 35, no. 1, pp. 185–196, 1987.

[45] M. Frary and C. A. Schuh, "Grain boundary networks: Scaling laws, preferred cluster structure, and their implications for grain boundary engineering," *Acta materialia*, vol. 53, no. 16, pp. 4323–4335, 2005.

[46] M. Elżanowski and G. Parry, "Material symmetry in a theory of continuously defective crystals," *Journal of Elasticity*, vol. 74, no. 3, pp. 215–237, 2004.

[47] F. Sansoz and J. Molinari, "Mechanical behavior of σ tilt grain boundaries in nanoscale cu and al: A quasicontinuum study," *Acta Materialia*, vol. 53, no. 7, pp. 1931–1944, 2005.

[48] J. Rittner and D. Seidman, "$<110>$ symmetric tilt grain-boundary structures in fcc metals with low stacking-fault energies," *Physical Review B*, vol. 54, no. 10, p. 6999, 1996.

[49] J. Yang, Y. Nagai, and M. Hasegawa, "Use of the frank–bilby equation for calculating misfit dislocation arrays in interfaces," *Scripta Materialia*, vol. 62, no. 7, pp. 458–461, 2010.

[50] V. Lubarda and D. Kouris, "Stress fields due to dislocation arrays at interfaces," *Mechanics of materials*, vol. 23, no. 3, pp. 191–203, 1996.

[51] M. D. Sangid, H. Sehitoglu, H. J. Maier, and T. Niendorf, "Grain boundary characterization and energetics of superalloys," *Materials Science and Engineering: A*, vol. 527, no. 26, pp. 7115–7125, 2010.

[52] A. Sutton and R. Balluffi, "Overview no. 61 on geometric criteria for low interfacial energy," *Acta Metallurgica*, vol. 35, no. 9, pp. 2177–2201, 1987.

[53] J. P. Hirth, "The influence of grain boundaries on mechanical properties," *Metallurgical Transactions*, vol. 3, no. 12, pp. 3047–3067, 1972.

[54] B. Liu, D. Raabe, P. Eisenlohr, F. Roters, A. Arsenlis, and G. Hommes, "Dislocation interactions and low-angle grain boundary strengthening," *Acta Materialia*, vol. 59, no. 19, pp. 7125–7134, 2011.

[55] I.-H. Lin and R. Thomson, "Cleavage, dislocation emission, and shielding for cracks under general loading," *Acta Metallurgica*, vol. 34, no. 2, pp. 187–206, 1986.

[56] T. Shimokawa, M. Tanaka, K. Kinoshita, and K. Higashida, "Roles of grain boundaries in improving fracture toughness of ultrafine-grained metals," *Physical Review B*, vol. 83, no. 21, p. 214113, 2011.

[57] M. Tschopp and D. McDowell, "Grain boundary dislocation sources in nanocrystalline copper," *Scripta Materialia*, vol. 58, no. 4, pp. 299–302, 2008.

[58] S. Kobayashi, M. Nakamura, S. Tsurekawa, and T. Watanabe, "Effect of grain boundary microstructure on fatigue crack propagation in austenitic stainless steel," *Journal of materials science*, vol. 46, no. 12, pp. 4254–4260, 2011.

[59] L. Lim and T. Watanabe, "Fracture toughness and brittle-ductile transition controlled by grain boundary character distribution (gbcd) in polycrystals," *Acta metallurgica et materialia*, vol. 38, no. 12, pp. 2507–2516, 1990.

[60] I. Adlakha, M. Tschopp, and K. Solanki, "The role of grain boundary structure and crystal orientation on crack growth asymmetry in aluminum," *Materials Science and Engineering: A*, vol. 618, pp. 345–354, 2014.

[61] Y. Zhou, Z. Yang, and Z. Lu, "Dynamic crack propagation in copper bicrystals grain boundary by atomistic simulation," *Materials Science and Engineering: A*, vol. 599, pp. 116–124, 2014.

[62] F. Cleri, S. R. Phillpot, and D. Wolf, "Atomistic simulations of integranular fracture in symmetric-tilt grain boundaries," *Interface Science*, vol. 7, no. 1, pp. 45–55, 1999.

[63] A. Luque, J. Aldazabal, J. MARTÍNEZ-ESNAOLA, and J. Gil Sevillano, "Molecular dynamics simulation of crack tip blunting in opposing directions

along a symmetrical tilt grain boundary of copper bicrystal," *Fatigue & Fracture of Engineering Materials & Structures*, vol. 30, no. 11, pp. 1008–1015, 2007.

[64] C. Cui and H. Beom, "Molecular statics simulations of intergranular fracture along $\sigma 11$ tilt grain boundaries in copper bicrystals," *Journal of Materials Science*, vol. 49, no. 24, pp. 8355–8364, 2014.

[65] E. OROWAX, "Fracture and strength of solids," *Rep. Prog. Phys*, vol. 12, p. 185, 1949.

[66] G. R. Irwin, "Fracture dynamics," *Fracturing of metals*, vol. 152, 1948.

[67] G. Irwin, "Crack-extension force for a part-through crack in a plate," *Journal of applied mechanics*, vol. 29, pp. 651–654, 1961.

[68] G. Beltz and J. Rice, "Dislocation nucleation at metal-ceramic interfaces," *Acta metallurgica et materialia*, vol. 40, pp. S321–S331, 1992.

[69] M. Jokl, V. Vitek, and C. McMahon, "A microscopic theory of brittle fracture in deformable solids: a relation between ideal work to fracture and plastic work," *Acta Metallurgica*, vol. 28, no. 11, pp. 1479–1488, 1980.

[70] B. Cockeram, "The role of stress state on the fracture toughness and toughening mechanisms of wrought molybdenum and molybdenum alloys," *Materials Science and Engineering: A*, vol. 528, no. 1, pp. 288–308, 2010.

[71] J.-S. Wang and P. Anderson, "Fracture behavior of embrittled fcc metal bicrystals," *Acta metallurgica et materialia*, vol. 39, no. 5, pp. 779–792, 1991.

[72] L. Freund and J. Hutchinson, "High strain-rate crack growth in rate-dependent plastic solids," *Journal of the Mechanics and Physics of Solids*, vol. 33, no. 2, pp. 169–191, 1985.

[73] A. Needleman, "An analysis of tensile decohesion along an interface," *Journal of the Mechanics and Physics of Solids*, vol. 38, no. 3, pp. 289–324, 1990.

[74] D. Warner and J. Molinari, "Micromechanical finite element modeling of compressive fracture in confined alumina ceramic," *Acta Materialia*, vol. 54, no. 19, pp. 5135–5145, 2006.

[75] X. Zhou, J. Zimmerman, E. Reedy, and N. Moody, "Molecular dynamics simulation based cohesive surface representation of mixed mode fracture," *Mechanics of Materials*, vol. 40, no. 10, pp. 832–845, 2008.

[76] R. Miller, E. Tadmor, R. Phillips, and M. Ortiz, "Quasicontinuum simulation of fracture at the atomic scale," *Modelling and Simulation in Materials Science and Engineering*, vol. 6, no. 5, p. 607, 1998.

[77] J. J. Möller and E. Bitzek, "Fracture toughness and bond trapping of grain boundary cracks," *Acta Materialia*, vol. 73, pp. 1–11, 2014.

[78] R. E. Jones and J. A. Zimmerman, "The construction and application of an atomistic j-integral via hardy estimates of continuum fields," *Journal of the Mechanics and Physics of Solids*, vol. 58, no. 9, pp. 1318–1337, 2010.

[79] Y. Xu, K. Behdinan, and Z. Fawaz, "Molecular dynamics calculation of the j-integral fracture criterion for nano-sized crystals," *International journal of fracture*, vol. 130, no. 2, pp. 571–583, 2004.

[80] J. A. Zimmerman and R. E. Jones, "The application of an atomistic j-integral to a ductile crack," *Journal of Physics: Condensed Matter*, vol. 25, no. 15, p. 155402, 2013.

[81] J. R. Rice, "A path independent integral and the approximate analysis of strain concentration by notches and cracks," *Journal of applied mechanics*, vol. 35, no. 2, pp. 379–386, 1968.

[82] B. Liu and X. Qiu, "How to compute the atomic stress objectively?," *Journal of Computational and Theoretical Nanoscience*, vol. 6, no. 5, pp. 1081–1089, 2009.

[83] J. A. Zimmerman, E. B. WebbIII, J. Hoyt, R. E. Jones, P. Klein, and D. J. Bammann, "Calculation of stress in atomistic simulation," *Modelling and Simulation in Materials Science and Engineering*, vol. 12, no. 4, p. S319, 2004.

[84] N. Bernstein and D. Hess, "Lattice trapping barriers to brittle fracture," *Physical review letters*, vol. 91, no. 2, p. 025501, 2003.

[85] E. Bitzek, J. R. Kermode, and P. Gumbsch, "Atomistic aspects of fracture," *International Journal of Fracture*, vol. 191, no. 1-2, pp. 13–30, 2015.

[86] S. Plimpton, "Fast parallel algorithms for short-range molecular dynamics," *Journal of computational physics*, vol. 117, no. 1, pp. 1–19, 1995.

[87] A. Stukowski, "Visualization and analysis of atomistic simulation data with ovito–the open visualization tool," *Modelling and Simulation in Materials Science and Engineering*, vol. 18, no. 1, p. 015012, 2010.

[88] M. S. Daw and M. I. Baskes, "Embedded-atom method: Derivation and application to impurities, surfaces, and other defects in metals," *Physical Review B*, vol. 29, no. 12, p. 6443, 1984.

[89] J. E. Angelo, N. R. Moody, and M. I. Baskes, "Trapping of hydrogen to lattice defects in nickel," *Modelling and Simulation in Materials Science and Engineering*, vol. 3, no. 3, p. 289, 1995.

[90] X. Zhou, J. A. Zimmerman, B. M. Wong, and J. J. Hoyt, "An embedded-atom method interatomic potential for pd–h alloys," *Journal of Materials Research*, vol. 23, no. 03, pp. 704–718, 2008.

[91] S. Nosé, "A unified formulation of the constant temperature molecular dynamics methods," *The Journal of chemical physics*, vol. 81, no. 1, pp. 511–519, 1984.

[92] W. G. Hoover, "Canonical dynamics: equilibrium phase-space distributions," *Physical Review A*, vol. 31, no. 3, p. 1695, 1985.

[93] W. Zhixun, G. Wenxuan, and Y. Zhufeng, "Crack propagation paths and fracture of ni-based single crystal," *Rare Metal Materials and Engineering*, vol. 36, no. 9, p. 1549, 2007.

[94] H. Grimmer, "Coincidence-site lattices," *Acta Crystallographica Section A: Crystal Physics, Diffraction, Theoretical and General Crystallography*, vol. 32, no. 5, pp. 783–785, 1976.

[95] O. C. Zienkiewicz, R. L. Taylor, O. C. Zienkiewicz, and R. L. Taylor, *The finite element method*, vol. 3. McGraw-hill London, 1977.

[96] A. Comsol, "Comsol multiphysics user's guide," *Version: September*, 2005.

[97] M. T. Vaughn, "Finite-dimensional vector spaces," *Introduction to Mathematical Physics*, pp. 37–92, 2007.

[98] L. M. Dupuy and R. E. Rudd, "Surface identification, meshing and analysis during large molecular dynamics simulations," *Modelling and Simulation in Materials Science and Engineering*, vol. 14, no. 2, p. 229, 2006.

[99] J. Zimmerman, C. Kelchner, P. Klein, J. Hamilton, and S. Foiles, "Surface step effects on nanoindentation," *Physical Review Letters*, vol. 87, no. 16, p. 165507, 2001.

[100] A. Stukowski and K. Albe, "Extracting dislocations and non-dislocation crystal defects from atomistic simulation data," *Modelling and Simulation in Materials Science and Engineering*, vol. 18, no. 8, p. 085001, 2010.

[101] J. P. Hirth and J. Lothe, *Theory of Dislocations*. Wiley, 1982.

[102] H. Vehoff and P. Neumann, "In situ sem experiments concerning the mechanism of ductile crack growth," *Acta Metallurgica*, vol. 27, no. 5, pp. 915–920, 1979.

[103] H. Vehoff and W. Rothe, "Gaseous hydrogen embrittlement in fesi-and ni-single crystals," *Acta Metallurgica*, vol. 31, no. 11, pp. 1781–1793, 1983.

[104] J. Rice, "First-order variation in elastic fields due to variation in location of a planar crack front," *Journal of Applied Mechanics*, vol. 52, no. 3, pp. 571–579, 1985.

[105] H. Gao, Y. Huang, and F. F. Abraham, "Continuum and atomistic studies of intersonic crack propagation," *Journal of the Mechanics and Physics of Solids*, vol. 49, no. 9, pp. 2113–2132, 2001.

[106] Y. Katz, R. Keller, H. Huang, and W. Gerberich, "A dislocation shielding model for the fracture of semibrittle polycrystals," *Metallurgical Transactions A*, vol. 24, no. 2, pp. 343–350, 1993.

[107] X. Zeng and A. Hartmaier, "Modeling size effects on fracture toughness by dislocation dynamics," *Acta Materialia*, vol. 58, no. 1, pp. 301–310, 2010.

[108] H. Huang and W. Gerberich, "Quasi-equilibrium modeling of the toughness transition during semibrittle cleavage," *Acta metallurgica et materialia*, vol. 42, no. 3, pp. 639–647, 1994.

[109] A. Romanov and V. Vladimirov, "Disclinations in solids," *Physica status solidi (a)*, vol. 78, no. 1, pp. 11–34, 1983.

[110] I. Ovid'ko, A. Sheinerman, and E. Aifantis, "Stress-driven migration of grain boundaries and fracture processes in nanocrystalline ceramics and metals," *Acta Materialia*, vol. 56, no. 12, pp. 2718–2727, 2008.

[111] S. Bobylev, N. Morozov, and I. Ovid'ko, "Cooperative grain boundary sliding and migration process in nanocrystalline solids," *Physical review letters*, vol. 105, no. 5, p. 055504, 2010.

[112] Q. Fang, Y. Liu, C. Jiang, and B. Li, "Interaction of a wedge disclination dipole with interfacial cracks," *Engineering fracture mechanics*, vol. 73, no. 9, pp. 1235–1248, 2006.

[113] V. Yamakov, D. Wolf, S. Phillpot, A. Mukherjee, and H. Gleiter, "Deformation-mechanism map for nanocrystalline metals by molecular-dynamics simulation," *nature materials*, vol. 3, no. 1, pp. 43–47, 2004.

[114] J. Schiøtz and K. W. Jacobsen, "A maximum in the strength of nanocrystalline copper," *Science*, vol. 301, no. 5638, pp. 1357–1359, 2003.

[115] T. Fang, W. Li, N. Tao, and K. Lu, "Revealing extraordinary intrinsic tensile plasticity in gradient nano-grained copper," *Science*, vol. 331, no. 6024, pp. 1587–1590, 2011.

[116] D. Gianola, S. Van Petegem, M. Legros, S. Brandstetter, H. Van Swygenhoven, and K. Hemker, "Stress-assisted discontinuous grain growth and its effect on the deformation behavior of nanocrystalline aluminum thin films," *Acta Materialia*, vol. 54, no. 8, pp. 2253–2263, 2006.

[117] L. Lu, L. Wang, B. Ding, and K. Lu, "High-tensile ductility in nanocrystalline copper," *Journal of Materials Research*, vol. 15, no. 02, pp. 270–273, 2000.

[118] F. Östlund, P. R. Howie, R. Ghisleni, S. Korte, K. Leifer, W. J. Clegg, and J. Michler, "Ductile–brittle transition in micropillar compression of gaas at room temperature," *Philosophical Magazine*, vol. 91, no. 7-9, pp. 1190–1199, 2011.

[119] C. Peng, Y. Zhan, and J. Lou, "Size-dependent fracture mode transition in copper nanowires," *Small*, vol. 8, no. 12, pp. 1889–1894, 2012.

[120] J. Markmann, P. Bunzel, H. Rösner, K. Liu, K. Padmanabhan, R. Birringer, H. Gleiter, and J. Weissmüller, "Microstructure evolution during rolling of inert-gas condensed palladium," *Scripta Materialia*, vol. 49, no. 7, pp. 637–644, 2003.

[121] D. Wells, *The Penguin dictionary of curious and interesting numbers*. Penguin, 1997.

[122] W. S. Thomson, "On the division of space with minimum partitional area," *Acta mathematica*, vol. 11, no. 1-4, pp. 121–134, 1887.

[123] A. Jivkov, N. Stevens, and T. Marrow, "A three-dimensional computational model for intergranular cracking," *Computational materials science*, vol. 38, no. 2, pp. 442–453, 2006.

[124] A. Jivkov and T. Marrow, "Rates of intergranular environment assisted cracking in three-dimensional model microstructures," *Theoretical and Applied Fracture Mechanics*, vol. 48, no. 3, pp. 187–202, 2007.

[125] K. Aust and N. Chen, "Effect of orientation difference on the plastic deformation of aluminum bicrystals," *Acta Metallurgica*, vol. 2, no. 4, pp. 632–638, 1954.

[126] S. D. Antolovich and B. Singh, "On the toughness increment associated with the austenite to martensite phase transformation in trip steels," *Metallurgical and Materials Transactions B*, vol. 2, no. 8, pp. 2135–2141, 1971.

[127] P. M. Kelly and L. F. Rose, "The martensitic transformation in ceramics—its role in transformation toughening," *Progress in Materials Science*, vol. 47, no. 5, pp. 463–557, 2002.

[128] W. H. Woodford, Y.-M. Chiang, and W. C. Carter, ""electrochemical shock" of intercalation electrodes: a fracture mechanics analysis," *Journal of the Electrochemical Society*, vol. 157, no. 10, pp. A1052–A1059, 2010.

[129] V. Panin, "Overview on mesomechanics of plastic deformation and fracture of solids," *Theoretical and applied fracture mechanics*, vol. 30, no. 1, pp. 1–11, 1998.

[130] S.-J. Chang and S. Ohr, "Dislocation-free zone model of fracture," *Journal of Applied Physics*, vol. 52, no. 12, pp. 7174–7181, 1981.

[131] A. Arsenlis and D. M. Parks, "Modeling the evolution of crystallographic dislocation density in crystal plasticity," *Journal of the Mechanics and Physics of Solids*, vol. 50, no. 9, pp. 1979–2009, 2002.

[132] A. Needleman, "Computational mechanics at the mesoscale," *Acta Materialia*, vol. 48, no. 1, pp. 105–124, 2000.

[133] Y. Mishin, M. Asta, and J. Li, "Atomistic modeling of interfaces and their impact on microstructure and properties," *Acta Materialia*, vol. 58, no. 4, pp. 1117–1151, 2010.

[134] V. I. Razumovskiy, A. Lozovoi, and I. Razumovskii, "First-principles-aided design of a new ni-base superalloy: Influence of transition metal alloying elements on grain boundary and bulk cohesion," *Acta Materialia*, vol. 82, pp. 369–377, 2015.

[135] R. Oriani, "Hydrogen embrittlement of steels," *Annual review of materials science*, vol. 8, no. 1, pp. 327–357, 1978.

[136] R. Oriani, "The physical and metallurgical aspects of hydrogen in metals," *Fusion Technology*, vol. 26, no. 4, pp. 235–266, 1994.

[137] H. K. Birnbaum and P. Sofronis, "Hydrogen-enhanced localized plasticity—a mechanism for hydrogen-related fracture," *Materials Science and Engineering: A*, vol. 176, no. 1, pp. 191–202, 1994.

[138] D. Westlake, "The habit planes of zirconium hydride in zirconium and zircaloy," *Journal of Nuclear Materials*, vol. 26, no. 2, pp. 208–216, 1968.

[139] S. Lynch, "Environmentally assisted cracking: overview of evidence for an adsorption-induced localised-slip process," *Acta Metallurgica*, vol. 36, no. 10, pp. 2639–2661, 1988.

[140] R. Kirchheim, B. Somerday, and P. Sofronis, "Chemomechanical effects on the separation of interfaces occurring during fracture with emphasis on the hydrogen-iron and hydrogen-nickel system," *Acta Materialia*, vol. 99, pp. 87–98, 2015.

[141] J. R. Rice and J.-S. Wang, "Embrittlement of interfaces by solute segregation," *Materials Science and Engineering: A*, vol. 107, pp. 23–40, 1989.

[142] W. Mills, "Fracture toughness of two ni-fe-cr alloys," *Engineering Fracture Mechanics*, vol. 26, no. 2, pp. 223–238, 1987.

[143] M. Srinivas, G. Malakondaiah, and P. R. Rao, "Fracture toughness of fcc nickel and strain ageing bcc iron in the temperature range 77–773 k," *Acta metallurgica et materialia*, vol. 41, no. 4, pp. 1301–1312, 1993.

[144] D. M. Bahr and W. S. Johnson, "Temperature dependent fracture toughness of a single crystal nickel superalloy," *Journal of ASTM International*, vol. 2, no. 4, 2005.

[145] M. Ashby, C. Gandhi, and D. Taplin, "Overview no. 3 fracture-mechanism maps and their construction for fcc metals and alloys," *Acta metallurgica*, vol. 27, no. 5, pp. 699–729, 1979.

[146] K.-M. Chang, R. Darolia, and H. Lipsitt, "Cleavage fracture in b2 aluminides," *Acta metallurgica et materialia*, vol. 40, no. 10, pp. 2727–2737, 1992.

[147] D. Miracle, "Overview no. 104 the physical and mechanical properties of nial," *Acta Metallurgica et Materialia*, vol. 41, no. 3, pp. 649–684, 1993.

[148] D. Lassila and H. Birnbaum, "The effect of diffusive hydrogen segregation on fracture of polycrystalline nickel," *Acta Metallurgica*, vol. 34, no. 7, pp. 1237–1243, 1986.

[149] D. M. Symons, "The effect of hydrogen on the fracture toughness of alloy x-750 at elevated temperatures," *Journal of nuclear materials*, vol. 265, no. 3, pp. 225–231, 1999.

[150] W. Mills and C. Brown, "Fracture behavior of nickel-based alloys in water," in *Ninth International Symposium on Environmental Degradation of Materials*

in Nuclear Power Systems-Water Reactors, pp. 167–177, Wiley Online Library, 1999.

[151] E. Van der Giessen and A. Needleman, "Discrete dislocation plasticity: a simple planar model," *Modelling and Simulation in Materials Science and Engineering*, vol. 3, no. 5, p. 689, 1995.

[152] E. Bittencourt, A. Needleman, M. E. Gurtin, and E. Van der Giessen, "A comparison of nonlocal continuum and discrete dislocation plasticity predictions," *Journal of the Mechanics and Physics of Solids*, vol. 51, no. 2, pp. 281–310, 2003.

[153] L. Shilkrot, R. E. Miller, and W. A. Curtin, "Multiscale plasticity modeling: coupled atomistics and discrete dislocation mechanics," *Journal of the Mechanics and Physics of Solids*, vol. 52, no. 4, pp. 755–787, 2004.

[154] W. Curtin, V. Deshpande, A. Needleman, E. Van der Giessen, and M. Wallin, "Hybrid discrete dislocation models for fatigue crack growth," *International Journal of Fatigue*, vol. 32, no. 9, pp. 1511–1520, 2010.

[155] S. Metals, "Inconel alloy 600," *Technical Bulletin SMC-027*, 2008.

[156] S. Metals, "Inconel alloy 718," *Publication No. SMC-045, Special Metals Corporation, Huntington, WV, USA*, 2007.

[157] R. Morris, "Rene 41-new higher-strength nickel-base alloy," *Metal Progr.*, vol. 76, 1959.

[158] W. Betteridge, *The nimonic alloys*. E. Arnold, 1959.

[159] F. Long, Y. Yoo, C. Jo, S. Seo, H. Jeong, Y. Song, T. Jin, and Z. Hu, "Phase transformation of η and σ phases in an experimental nickel-based superalloy," *Journal of Alloys and Compounds*, vol. 478, no. 1, pp. 181–187, 2009.

[160] R. Cozar and A. Pineau, "Morphology of y'and y" precipitates and thermal stability of inconel 718 type alloys," *Metallurgical Transactions*, vol. 4, no. 1, pp. 47–59, 1973.

[161] M. Wang, J. Hanson, S. Gradečak, and M. Demkowicz, "Cutting apart of γ precipitates by dislocations emitted from nanoscale surface notches in ni-base alloy 725," *Materials Research Letters*, vol. 1, no. 2, pp. 77–80, 2013.